



HAL
open science

Analyse de la microstructure 3D du tissu cardiaque humain à l'aide de la micro-tomographie à rayons X par contraste de phase

Iulia Mirea

► **To cite this version:**

Iulia Mirea. Analyse de la microstructure 3D du tissu cardiaque humain à l'aide de la micro-tomographie à rayons X par contraste de phase. Imagerie médicale. Université de Lyon, 2017. Français. NNT : 2017LYSEI076 . tel-01973886

HAL Id: tel-01973886

<https://theses.hal.science/tel-01973886>

Submitted on 8 Jan 2019

HAL is a multi-disciplinary open access archive for the deposit and dissemination of scientific research documents, whether they are published or not. The documents may come from teaching and research institutions in France or abroad, or from public or private research centers.

L'archive ouverte pluridisciplinaire **HAL**, est destinée au dépôt et à la diffusion de documents scientifiques de niveau recherche, publiés ou non, émanant des établissements d'enseignement et de recherche français ou étrangers, des laboratoires publics ou privés.

Numéro d'ordre : 2017LYSEI076

Année 2017

THÈSE

présentée devant

L'Institut National des Sciences Appliquées de Lyon

DIPLÔME DE DOCTORAT

ÉCOLE DOCTORALE 160 : Électronique, Électrotechnique, Automatique

Soutenue publiquement le 19 septembre 2017 par

Iulia MIREA

Analyse de la microstructure 3D du tissu cardiaque humain à l'aide de la micro-tomographie à rayons X par contraste de phase

Jury

Bart BIJNENS	Professeur, Université POMPEU-FABRA	Rapporteur
Christine FERNANDEZ-MALOIGNE	Professeur, Université de POITIERS	Rapporteur
Theo ARTS	Professeur, Université de MAASTRICHT	Examinateur
Patrick CLARYSSE	Directeur de Recherche CNRS	Examinateur
Pierre-Simon JOUK	PUPH, Université JOSEPH FOURIER	Examinateur
Wan Yu LIU	Professeur, Institut de Technologie de HARBIN	Examinateur
Isabelle MAGNIN	Directeur de Recherche INSERM	Directeur de thèse
Yue-Min ZHU	Directeur de Recherche CNRS	Co-Directeur de thèse

Numéro d'ordre :

Année 2017

THÈSE

présentée devant

L'Institut National des Sciences Appliquées de Lyon

DIPLÔME DE DOCTORAT

ÉCOLE DOCTORALE 160 : Électronique, Électrotechnique, Automatique

Defense on the 19 September 2017 by

Iulia MIREA

Analysis of the 3D microstructure of the human cardiac tissue using X-ray phase contrast micro-tomography

Jury

Bart BIJNENS	Professeur, Université POMPEU-FABRA	Rapporteur
Christine FERNANDEZ-MALOIGNE	Professeur, Université de POITIERS	Rapporteur
Theo ARTS	Professeur, Université de MAASTRICHT	Examinateur
Patrick CLARYSSE	Directeur de Recherche CNRS	Examinateur
Pierre-Simon JOUK	PUPH, Université JOSEPH FOURIER	Examinateur
Wan Yu LIU	Professeur, Institut de Technologie de HARBIN	Examinateur
Isabelle MAGNIN	Directeur de Recherche INSERM	Directeur de thèse
Yue-Min ZHU	Directeur de Recherche CNRS	Co-Directeur de thèse

Acknowledgements

I would first like to thank my advisors, Prof. Isabelle Magnin and Prof. Yue-Min Zhu, for guiding me throughout the preparation of this thesis. I also thank them for the countless hours they have spent proof-reading, correcting and suggesting improvements for this thesis and for the published articles, often under the pressure of very short deadlines. They have made great effort to always respond quickly to my difficulties and help get the work submitted on time. I would also like to thank Prof Isabelle Magnin for supporting me to learn French and for her patience in trying to understand my French when I just arrive in France. I also must say thank you to: Gabrielle Michalowicz, Pierre-Simon Jouk, Yves Usson and Laurent Fanton for their support and availability when medical answers were required and to Max Langer for his support with the technical information related to the ESRF technology.

I would like to give special thanks to Prof. Vasile Buzuloiu, originally one of my professors at the University Politehnica of Bucharest (he taught information theory), he was also the founder and head of LAPI (IPAL - Image Processing and Analysis Laboratory) and the director of the master program ITEMS from the same university. He is the one who brought me to the research field and introduced me to the image processing domain, through the spring and summer schools that he organised annually which led to my enrollment in his master program. I would also like to thank to Prof. Mihai Ciuc for all the support in my adventure of searching my PhD.

I want to thank my the “colombian” friends: Alfredo Morales Pinzón, William A. Romero Ramirez and Duván A. Gómez Bentacur who helped me with my big struggle: the visualization of huge volumes and of the results.

I am also grateful to all my friends from CREATIS and from France: Alina Toma, Lin Wang, Hongying Li, Carlos Torres, Shengfu Li, Yu Liang Julien, Estelle Hilaire, Meriem El Azami, Younes Farouj, Mohammad Azizian Kalkhoran, Maëva Vallet, Matthew Ozon, Emmanuel Roux, Liang Wang, Anca Cristea, Razvan Stoica, Bruno Sciolla, Monica Sigovan, Emilia Bădescu, Denis Bujoreanu, Yufei Li, Paul Boulos, Lorena Petrusca, Lucian Robian, Claire Mouton, Eduardo Dávila, Leonardo Flórez Valencia, Vincent Perrot, Maxime Polichettim, Bingqing Xie, Fabien Millioz, William Romero, Alfredo Morales, Duván Gómez. Thank you guys for the research, the volleyball games, the reading sessions, parties, concerts, mangas, ‘chocolate for writing’, Spanish lessons, beautiful stories, for all the moments that we shared together.

I would like to thank my fiance Tibi for always being at my side, supporting me and encouraging me to follow my dreams. And I would like to thank my parents, and my sisters: Tina, Cristina and Olivia, for everything they have done and still do for me.

Contents

Contents	ix
List of Symbols	xi
Synthèse en Français	xiii
0.1 Introduction générale	xiii
0.2 Chapitre 1: Le tissu cardiaque à l'échelle microscopique	xiv
0.3 Chapitre 2: Imagerie 3D du tissu cardiaque par μ -CT en Rayons X à Con- traste de Phase	xvi
0.4 Chapitre 3: Traitement d'image et analyse	xvii
0.5 Chapitre 4: Plans de clivage: analyse statistique	xviii
0.6 Conclusion générale	xix
General introduction	xxi
1 Microscopic cardiac structure	
Structure cardiaque à l'échelle microscopique	1
1.1 Introduction	1
1.2 Models of cardiac structure	2
1.2.1 Helical ventricular myocardial band model	2
1.2.2 Doughnut and pretzel models	3
1.2.3 Myolaminae model	4
1.2.4 Conclusion	4
1.3 Cardiac tissue components	5
1.3.1 Myocytes	5
1.3.2 Cardiac extracellular matrix	5
1.3.3 Terminology confusion: myofibres, myolaminae, sheetlets, cleavage planes, shear layers and fibres	5
1.4 Acquisition techniques	6
1.4.1 Dissection and histology	6
1.4.2 Electron microscopy	7
1.4.3 Confocal microscopy	7
1.4.4 Polarized Light Imaging	7
1.4.5 Magnetic Resonance Imaging	8
1.5 Conclusion	8

2	Cardiac microarchitecture using 3D X-ray Phase Contrast μ-CT	
	Imagerie 3D du tissu cardiaque par μ-CT en Rayons X à Contraste de Phase	9
2.1	Introduction	9
2.2	What is the ESRF?	10
2.3	Synchrotron radiation μ -CT setup at beamline ID19	11
2.4	Data reconstruction	12
2.4.1	Absorption CT	12
2.4.2	Absorption and phase CT	12
2.5	Heart samples collection and preparation	13
2.6	X-ray phase contrast tomographic imaging of the acquired samples	16
2.7	3D phase contrast image interpretation	16
2.8	Cardiac microarchitecture from different locations of the human heart	17
2.8.1	Cardiac microarchitecture of the posterior septum (sample 8)	19
2.8.2	Cardiac microarchitecture of the anterior septum (sample 7)	25
2.8.3	Cardiac microarchitecture of the posterior left ventricle (sample 6)	25
2.9	Conclusion	28
3	Image processing and analysis	
	Traitement d'image et analyse	33
3.1	Introduction	33
3.1.1	Cardiac extracellular matrix	34
3.2	Spatial and frequency description of the tissue components	35
3.2.1	Myocytes	35
3.2.2	Capillaries	35
3.2.3	Data sampling and frequency content	36
3.3	Multiscale processing	36
3.3.1	Pre-processing with the Gaussian pyramid	37
3.3.2	Extracting the cleavage planes orientation	42
3.3.3	Binarisation step	44
3.3.4	Binarisation step - threshold error analysis	46
3.4	Cleavage planes thicknesses and inter-cleavage planes distances	49
3.4.1	Virtual lines creation	49
3.4.2	Main direction error analysis	50
3.5	Methodology Evaluation	51
3.5.1	Creation of a synthetic volume	51
3.6	Conclusion	55
4	Cleavage Planes: statistical analysis	
	Plans de clivage: analyse statistique	59
4.1	Introduction	59
4.1.1	Statistical analysis of the transmural laminar microarchitecture of the human left ventricle (sample 1, LV_ant_S5_1)	60
4.1.2	Segmentation step	60
4.1.3	Orientation detection	62
4.1.4	Cleavage planes statistics of the anterior left ventricle (sample 4, LV_ant_S1_2)	64
4.1.5	Cleavage planes statistics of the posterior left ventricle (sample 6, LV_post_S1_2)	66

4.1.6	Cleavage planes statistics of the lateral left ventricle (sample 5, LV_lat_S1_2)	66
4.1.7	Cleavage planes statistics of the samples from slice 1 of the left ventricle (sample 4, 5, 6, LV_ant_S1_2, LV_lat_S1_2, LV_post_S1_2)	68
4.1.8	Cleavage planes statistics of the sample from slice 2 of the left ventricle - Anterior left ventricle (sample 3, LV_ant_S2_2)	68
4.1.9	Comparison between different anterior left ventricle samples from 2 hearts (samples 1, 3 and 4)	70
4.1.10	Cleavage planes statistics of the posterior septum (sample 8, S_post_S1_2)	74
4.1.11	Cleavage planes statistics of the anterior septum (sample 7, S_ant_S1_2)	75
4.1.12	Cleavage planes statistics of the antero-posterior septum (sample 9, S_antposta_S2_2)	75
4.1.13	Cleavage planes statistics of the antero-posterior septum (sample 10, S_antpostb_S2_2)	78
4.1.14	Comparison between the septum samples (samples 7, 8 and samples 9, 10)	78
4.2	Conclusion	80

General conclusion and perspectives	83
--	-----------

Appendix	87
-----------------	-----------

A 3D X-ray Phase Contrast μ-CT images	87
---	-----------

Bibliography	105
---------------------	------------

List of Symbols and abbreviations

2D	Two Dimensional
3D	Three Dimensional
CP	Cleavage Planes
DTI	Diffusion Tensor Imaging
DT-MRI	Diffusion Tensor Magnetic Resonance Imaging
ECM	ExtraCellular Matrix
ESRF	European Synchrotron Radiation Facility
FFT	Fast Fourier Transform
HVMB	Helical Ventricular Myocardial Band
ID19	Insertion Device 19
LV	Left Ventricle
MRI	Magnetic Resonance Imaging
PCA	Principal Component Analysis
ROI	Region Of Interest
SEM	Scanning Electron Microscopy
TEM	Transmission Electron Microscopy
VG	Ventricule Gauche (Left Ventricle)

Synthèse en Français

0.1 Introduction générale

Les pathologies cardiaques restent une des affections les plus fréquentes. Pour mieux les comprendre il est nécessaire d'explorer la structure anatomique et ses relations avec le caractère fonctionnel de cet organe. Notre objectif est donc d'accéder à la connaissance de la micro-architecture 3D du tissu cardiaque pour mieux comprendre le fonctionnement général du coeur, en particulier la biomécanique myocardique ainsi que les processus d'activation électrique du muscle. Cependant la connaissance de l'ultrastructure du tissu se heurte aux limitations inhérentes des méthodes d'exploration comme l'histologie ou les techniques d'imagerie disponibles ainsi qu'à la difficulté de prélever des échantillons de coeur humain frais (aspects légaux et techniques).

Dans cette thèse, nous explorons de manière entièrement nouvelle la microstructure 3D du tissu cardiaque humain frais. Grâce à une collaboration étroite avec un médecin légiste, il a été possible de disposer d'échantillons de paroi ventriculaire gauche de 2 coeurs adultes sains qui ont pu être immédiatement imagés en μ -tomographie par contraste de phase au synchrotron de Grenoble (ESFR). Un ensemble de 2499 projections RX en contraste de phase a été acquis pour chaque échantillon, en plusieurs étapes, sur l'ensemble de sa hauteur (6 mm x 6 mm x 15 à 20 mm). Chaque échantillon a ensuite été reconstruit en 3D à une résolution spatiale isotrope de $3,5 \times 3,5 \times 3,5 \mu m^3$. La quantité de données à traiter, extrêmement grande puisque chaque échantillon reconstruit occupe 80 GB, a été ramenée à environ 30 GB par échantillon après une sélection des données utiles.

Le plan de la thèse est le suivant: après une introduction générale (Chapitre 1), nous proposons, Chapitre 2, un état de l'art des connaissances de la littérature à propos de la microstructure du tissu cardiaque. Nous précisons les limitations actuelles des techniques d'exploration. Au Chapitre 3, nous proposons une nouvelle technique d'imagerie pour

explorer des échantillons de coeur humain frais. Une comparaison visuelle entre l’histologie 2D, prise comme référence, et les volumes 3D acquis, permet d’identifier les composants du tissu présents dans les images RX par contraste de phase.

0.2 Chapitre 1: Le tissu cardiaque à l’échelle microscopique

Ce chapitre 1 constitue un état de l’art bibliographique des connaissances actuelles principales de la structure du tissu cardiaque à l’échelle submillimétrique. Les différents modèles de la structure cardiaque sont présentés, ainsi que les confusions sur la terminologie utilisée pour les décrire. Nous avons recensé trois types de modèles cardiaques. Le premier modèle présenté fait référence à une bande de myocarde ventriculaire hélicoïdale (HVMB), inspiré par l’organisation du muscle squelettique. Le modèle cardiaque a été obtenu sur la base de techniques de dissection: il considère le muscle cardiaque comme une seule bande de muscle, enroulée autour de la racine de l’aorte et du tronc pulmonaire. Ce modèle a influencé l’intervention chirurgicale ainsi que la compréhension du remplissage systolique cardiaque, la contraction et la dynamique. Le HVMB a été rejeté par certains auteurs sur la base histologique, et également sur la base de la diffusion en IRM, qui a montré l’existence d’un changement progressif de l’orientation des fibres dans le myocarde ventriculaire. Toutefois, il y a également des preuves qui soutiennent le HVBM, des observations histologiques, optiques et DT-MRI qui montrent que le HVBM suit quand même un chemin dans la paroi cardiaque.

La deuxième façon de décrire la morphologie cardiaque consiste à voir le myocarde comme la musculature vasculaire, avec la ramification et la fusion des myocytes. L’un des modèles basés sur cette idée est le modèle de “donut” pour le ventricule gauche (VG), obtenu en extrayant les fibres de longueur minimale. L’expression mathématique est un peu obscure pour les anatomistes et les cardiologues, et Jouk a expliqué clairement ce modèle: tout d’abord, prendre un morceau de papier et dessiner trois lignes parallèles, ces lignes pourraient être considérées comme les géodésiques de la surface plane, ensuite, rouler le papier en mettant la bordure supérieure contre la bordure inférieure et former un cylindre. Les lignes dessinées dans la première étape deviennent les géodésiques du cylindre. Ensuite plier le cylindre jusqu’à ce que la gauche atteigne l’extrémité droite, un tore sera généré et les lignes sont encore géodésiques. Enfin, la conjecture de Streeter

suppose que de l'intérieur à l'extérieur le muscle myocardique possède une structure de tori imbriqués comme les poupées russes.

Le modèle de "donut" a ensuite été étendu au ventricule droit (VD) conduisant ainsi au modèle de "bretzel". Dans ce modèle, les fibres suivent le chemin géodésique de deux beignets joints côte à côte (bretzel). Les ventricules sont composés de trois couches nommées: couches superficielles, moyennes et profondes, mais le modèle est contradictoire ou vague concernant la transition entre les couches, les études indiquant une transition douce de l'orientation des fibres.

La troisième façon de décrire la morphologie cardiaque s'appuie sur la présence de couches musculaires discrètes ou de feuilles lamellaires de myocytes.

Nous indiquons rapidement les principales techniques d'acquisition utilisées pour étudier la structure cardiaque. Tout d'abord, l'histologie est une technique ancienne toujours utilisée, considérée comme la référence malgré des limitations importantes dont la nécessité de découper la pièce à analyser en fines lamelles (approche 2D) induisant ainsi des déformations de la structure. L'histologie nécessite l'usage de colorations diverses pour mettre en évidence, de façon différenciée, tel ou tel composant élémentaire du tissu. Viennent ensuite les méthodes d'imagerie optique, associées à l'histologie. L'imagerie confocale permet d'accéder à une information en profondeur du tissu et fournit une première vision 3D de la couche superficielle (quelques micro mètres). L'imagerie microscopique en lumière polarisée mesure les déviations d'un faisceau de lumière cohérente induites par certains composants du tissu qui possèdent des propriétés de biréfringence (comme les myocytes), permettant ainsi d'en évaluer la direction et l'agencement en 3D (résolution $100\ \mu\text{m}$ dans le plan sur des coupes d'épaisseur $500\ \mu\text{m}$). Cette technique présente l'inconvénient d'une immersion préalable du tissu dans une résine.

Par rapport aux techniques précédentes, l'imagerie par résonance magnétique n'est pas invasive et peut être utilisée *in-vivo* pour imager le coeur entier. L'IRM du Tenseur de Diffusion (DT-MRI) peut accéder à l'orientation dominante des myocytes dans chaque voxel en raison de la diffusion plus forte des molécules d'eau dans la direction parallèle à la direction principale des myocytes. Cependant, la résolution spatiale typique de l'IRM clinique est faible ($1\ \text{mm} \times 1\ \text{mm} \times 2\ \text{mm}$), donc l'organisation 3D des myocytes au niveau microscopique reste inconnue. Les configurations d'IRM à haute résolution peuvent atteindre des tailles de voxel de $30\ \mu\text{m} \times 30\ \mu\text{m} \times 300\ \mu\text{m}$ ou $60\ \mu\text{m} \times 60\ \mu\text{m} \times 60\ \mu\text{m}$,

mais cela reste supérieur au diamètre des myocytes.

Enfin la compréhension et la caractérisation précises de la structure cardiaque nécessitent une technique d'imagerie 3D qui permette de visualiser à la fois des cellules individuelles et de grands échantillons afin d'accéder à l'organisation locale et globale du tissu.

0.3 Chapitre 2: Imagerie 3D du tissu cardiaque par μ -CT en Rayons X à Contraste de Phase

Ce chapitre 2 décrit d'abord la procédure d'acquisition des images réalisées au Synchrotron européen (ESRF): après une description générale du principe de fonctionnement du synchrotron, nous décrivons le système d'acquisition permettant d'obtenir les images μ -CT à contraste de phase et les échantillons de tissu cardiaque humain imagés. Des échantillons de tissus du ventricule gauche et du septum ont été préparés et imagés à une résolution isotrope de 3,5 μm , ce qui est suffisant pour visualiser les myocytes qui constituent la paroi ventriculaire du coeur.

Nous établissons ensuite un parallèle entre les composants visibles dans les images d'histologie et ce que l'on peut voir dans les micro-tomographies 3D à contraste de phase des échantillons de coeur humain: cette technique nous permet d'interpréter ces nouvelles images. Nous choisissons un échantillon imagé en 3D au synchrotron et nous le comparons à des coupes histologiques afin d'en identifier les composants.

Nous poursuivons par une analyse détaillée des volumes 3D de quelques échantillons représentatifs, en identifiant les principaux composants des tissus visibles dans les images, en examinant leur organisation en 3D (ce qui n'a jamais été réalisé de façon aussi approfondie en 3D) et en comparant qualitativement l'agencement des composants du tissu d'un échantillon à l'autre. Des exemples complémentaires figurent dans l'annexe 1.

Ensuite trois échantillons transmuraux de paroi du VG sont analysés: deux respectivement localisés dans le septum postérieur et antérieur et un dans le VG postérieur. Le premier échantillon transmural analysé visuellement en 3D est le septum postérieur. Il y a quelques controverses liées à l'architecture cardiaque du septum: y a-t-il ou non, une zone de séparation entre les deux ventricules? L'échantillon transmural 3D du septum

postérieur présente deux modèles d'organisation. L'un des motifs est décrit par les plans de clivage parallèles avec beaucoup de ramifications. L'orientation globale des plans de clivage change lentement de l'endocardium vers l'épicardium, jusqu'à ce qu'ils atteignent l'autre motif. Dans l'autre motif, les plans de clivage ne sont pas tellement prononcés (beaucoup plus minces) et les myocytes sont disposées de façon plus compacte. La transition entre les deux modèles est abrupte, comme on peut le voir dans les images jointes.

Les échantillons de septum antérieur et postérieur sont organisés différemment. Le septum postérieur montre deux modèles d'organisation, le premier étant plus fragmenté, avec beaucoup de plans de clivage parallèles et branchés, tandis que le second motif ressemble à celui du septum antérieur. Le septum antérieur montre un motif unique, comportant des myocytes disposées de manière compacte et quelques plans de clivage. Dans les motifs compacts, les échantillons de septum antérieur et postérieur présentent des zones dans lesquelles l'orientation des myocytes change brusquement.

Dans tous les échantillons, nous observons que les plans de clivage sont la plupart du temps localement parallèles et changent en douceur leur orientation. Cependant, dans certaines régions, des changements soudain dans l'orientation de groupes de myocytes voisins ont été observés, correspondant à des volumes de tissus qui se contractent presque dans des directions orthogonales. Il existe également de grandes zones où les plans de clivage se ramifient et fusionnent. Nous avons également confirmé l'existence de deux populations quasi-orthogonales de plans de clivage dans certaines régions du ventricule gauche (précédemment rapporté dans la littérature), qui ont un rôle important dans la biomécanique du mouvement cardiaque.

0.4 Chapitre 3: Traitement d'image et analyse

La matrice extracellulaire cardiaque comprend: l'endomysium qui entoure et sépare les myocytes et les capillaires individuels, le périnysium qui entoure et sépare les groupes de myocytes et l'épinysium qui entoure tout le muscle cardiaque. Chaque myocyte et capillaire est attaché aux cordons de collagène de l'endomysium et les groupes de myocytes sont séparés par des structures en lamelles de périnysium ("Plans de Clivage (CP)").

Afin de quantifier les distances inter-CP et les épaisseurs des CP, la première étape consiste à extraire les plans de clivage. Pour cela, nous avons adapté une méthode de seuillage

automatique (Otsu) sur une Différence de Gaussiennes. La taille des filtres Gaussiens destinés à éliminer les éléments indésirables de l'image comme les myocytes et l'endomysium est choisie à partir de l'étude des relations entre la forme et la taille des composants que nous voulons détecter dans le tissu cardiaque et leurs fréquences spatiales correspondantes.

La longueur des myocytes est entre $50 \mu\text{m}$ et $150 \mu\text{m}$, les fréquences spatiales correspondantes varient donc entre $0,02 \mu\text{m}^{-1}$ et $0,0066 \mu\text{m}^{-1}$ respectivement. Les capillaires ont un diamètre compris entre $8 \mu\text{m}$ et $10 \mu\text{m}$. Le diamètre de celui-ci est identique ou un peu plus petit que celui des myocytes. Leurs fréquences spatiales associées vont de $0,125 \mu\text{m}^{-1}$ à $0,1 \mu\text{m}^{-1}$ respectivement. La longueur des capillaires est d'environ 1 mm à 2 mm , donc leur contribution se situera à très basse fréquence: de $0,001 \mu\text{m}^{-1}$ à $0,0005 \mu\text{m}^{-1}$. Notre objectif est d'identifier et de séparer les différents composants du tissu selon leur taille et leur forme spécifiques, en particulier d'isoler les plans de clivage. Pour ce faire, nous avons privilégié un double filtrage par pyramide Gaussienne de chaque volume d'échantillon. Dans la pyramide Gaussienne, nous conservons les deux niveaux suivants: le niveau $\sigma_1 = 3$ qui vise à filtrer les données avec un filtre isotrope Gaussien de $13 \times 13 \times 13$ voxels et le niveau $\sigma_1 = 44$ qui vise à filtrer les données avec un filtre de taille $177 \times 177 \times 177$ voxels.

L'étape suivante est basée sur le fait que les plans de clivage sont localement parallèles et ont une orientation 3D privilégiée. Sur la base de cette propriété des CP, nous créons une grille virtuelle de lignes. Pour cela, nous avons extrait la direction perpendiculaire aux CP via la Transformée de Fourier Rapide (FFT) en trois dimensions. La méthode consiste à binariser la FFT 3D et à extraire la direction principale du nuage de points après binarisation. Cette orientation est de fait orthogonale à la direction principale des plans de clivage. Sur cette base, une grille de lignes traversant les CP perpendiculairement a été créée ce qui permet ensuite de mesurer à la fois l'épaisseur des CP ainsi que la distance qui les sépare. L'erreur possible induite par chaque étape de la méthode automatique mise en oeuvre est analysée. Enfin, les mesures issues de la méthode automatique sont comparées à une mesure manuelle sur un volume synthétique.

0.5 Chapitre 4: Plans de clivage: analyse statistique

Le but de ce chapitre est d'analyser quantitativement la matrice extracellulaire du périnysium pour tous les échantillons ESRF présentés au chapitre 2. La méthode utilisée

a été présentée au chapitre 3. Ce chapitre est axé sur l'application de la méthode sur l'ensemble des échantillons transmuraux. Toute l'étape présentée au chapitre 3 a été appliquée sur de petites parties de l'échantillon, en tenant compte du fait que l'orientation des plans de clivage évolue lentement en 3D. Nous présentons pour un échantillon transmural tous les résultats intermédiaires après chaque étape du traitement pour quantifier les distances inter-CP et l'épaisseur des CP. Nous avons également analysé l'erreur qui peut apparaître en fonction de l'extraction de l'orientation principale sur une région d'intérêt (ROI). Nous comparons les résultats statistiques obtenus en utilisant une orientation principale extraite d'une sous-ROI située au centre de l'échantillon avec le cas où l'échantillon est entièrement décomposé en 64 sous-ROI de même taille. Les statistiques mesurées sur les distances inter-CP et leur épaisseur sont présentées et analysées pour tous les échantillons. Les résultats montrent que l'épaisseur des CP varie approximativement entre 24 μm et 59 μm et que la distance inter-CP varie approximativement entre 70 μm et 280 μm , avec des variations locales importantes de l'écart type.

Nous avons comparé les échantillons situés à la même altitude dans le VG (tranche parallèle à la base): postérieures, antérieures et latérales du même coeur (tranche 1). Nous avons comparé les 3 échantillons du ventricule gauche antérieur de différentes tranches pour 2 coeurs humains différents et également les échantillons de septum antérieur et postérieur situés plus ou moins loin de la base (différentes tranches). La conclusion est que chaque échantillon a sa spécificité, et que les distances inter-CP et les épaisseurs de CP ne sont pas similaires, bien qu'il existe des régions de similarité. Les épaisseurs de CP et les distances inter-CP du ventricule antérieur, postérieur et latéral gauche de l'échantillon 1, du même coeur, sont généralement différentes, certaines régions ayant des valeurs similaires. La distance inter-CP du septum antérieur et postérieur est similaire à celle de la paroi centrale jusqu'à la profondeur de la paroi de 100%. Les épaisseurs des CP sont très similaires pour le septum antérieur et postérieur.

0.6 Conclusion générale

L'objectif de cette thèse était d'explorer la structure 3D microscopique du muscle cardiaque humain *ex-vivo*. Pour dépasser les limitations des techniques d'imagerie 3D comme l'IRM de diffusion ou le scanner, nous avons utilisé la micro-tomographie X par contraste de phase développée au synchrotron européen (ESFR). Dix échantillons de ventricule gauche

et de septum de coeur humain frais normal ont été préparés, imagés et reconstruits en 3D à une résolution isotrope de $3,5 \mu m$. Les volumes obtenus ont été comparés à des coupes histologiques qui ont servi de référence pour interpréter leur contenu et identifier les composants du tissu.

Nos expériences ont montré que la micro tomographie est une technique viable pour explorer, *ex-vivo*, l'arrangement 3D des myocytes à l'échelle microscopique, permettant ainsi de mieux comprendre la micro architecture 3D du tissu cardiaque. Pour la première fois, il a été possible d'observer l'agencement 3D des différents composants tels que les myocytes, les capillaires et la matrice extracellulaire, de l'épicarde à l'endocarde, à une échelle allant du μm au cm. Nous avons réalisé une analyse descriptive de trois échantillons prélevés dans le ventricule gauche postérieur ainsi que dans le septum antérieur et postérieur. La visualisation de volumes de données de plusieurs dizaines de GB n'a pas été possible avec les logiciels usuels, nous avons donc été contraints soit d'afficher de petites portions d'échantillon à pleine résolution soit d'afficher les échantillons dans leur ensemble à une résolution moindre.

Ensuite nous nous sommes focalisés sur l'analyse de la matrice extracellulaire, plus particulièrement sur les plans de clivage (CP). Nous avons développé un protocole de traitement d'image pour extraire automatiquement les plans de clivage et calculer des statistiques sur leur épaisseur et la distance qui les sépare en 3D. La méthode de calcul est basée sur le fait que les plans de clivage sont localement parallèles et possèdent une orientation 3D privilégiée. Nous avons montré que la méthode proposée est efficace pour mettre en évidence les CP présents dans le myocarde et pour quantifier de nouveaux biomarqueurs tels que l'épaisseur des CP et la distance inter-CP. Nous avons montré que ces deux descripteurs structurels varient peu lorsque l'on traverse la paroi du VG de l'épicarde vers l'endocarde, au sein d'un même échantillon de tissu mais qu'ils peuvent varier significativement entre deux échantillons de tissus pris dans le septum ou dans le VG antérieur ou postérieur.

Nous avons également confirmé la présence de deux populations quasi-orthogonales de CP dans certaines régions du VG (déjà rapporté dans la littérature) dont le rôle dans la biomécanique cardiaque est certainement primordial. Enfin, les données statistiques quantitatives que nous avons extraites montrent que l'épaisseur des plans de clivage varie grosso-modo entre $24 \mu m$ et $59 \mu m$ et que la distance entre les plans de clivage se situe approximativement entre $70 \mu m$ et $280 \mu m$, avec des variations locales significatives.

General introduction

Gaining insight about the 3D micro-architecture of cardiac tissue has become indispensable for a better understanding of the general functioning of the heart, especially the cardiac biomechanics as well as the electrical activation process of the muscle. However, knowledge of the tissue ultrastructure is hindered by the inherent limitations of traditional exploration methods such as histology or the different imaging techniques available, as well as by the difficulty of obtaining fresh human heart samples (legal and technical aspects).

In this thesis, we take a novel approach to exploring the 3D microarchitecture of fresh human cardiac tissue. Thanks to a tight collaboration with a forensic doctor, it was possible to obtain samples from the left ventricle wall of two healthy adult hearts, which were immediately imaged in phase contrast μ -tomography at the European Synchrotron Radiation Facility (ESRF) in Grenoble. A set of 2499 phase contrast RX projections was acquired for each sample, in several stages, over its entire height (6 mm x 6 mm x 15 to 20 mm). Afterwards, each sample was reconstructed in 3D at an isotropic spatial resolution of $3,5 \times 3,5 \times 3,5 \mu m^3$. The huge amount of data to process (80 GB for each reconstructed sample) was reduced to approx. 30 GB per sample through a selection of useful data.

This thesis is structured as follows: After a state of the art concerning the cardiac tissue microstructure (Chapter 1), we highlight the limitations of current exploration techniques and we present a new imaging technique for exploring fresh human heart samples (Chapter 2). A visual comparison between 2D histology (taken as reference) and the acquired 3D volumes allows us to identify the tissue components present in the phase contrast images.

Our first contribution is a descriptive analysis of the content of several samples taken from the anterior left ventricle, the posterior left ventricle and the septum. For the first time, it is possible to observe the 3D arrangement of myocytes, capillaries and the extracellular matrix, from epicardium to endocardium, at a scale ranging between a few μm to 1 cm. Visualizing data volumes of several GB in size was not possible with conventional software, therefore we resorted to either displaying small parts of the samples at high resolution, or entire samples at a lower resolution.

Chapter 3 is focused on a numerical analysis of the 3D images. Considering the large image dimensions, a multiscale processing strategy was chosen. After a dimensional analysis (spatial frequencies) of tissue components, we decided to focus our analysis on the architecture of the extracellular matrix. A Gaussian filtering strategy was implemented, followed by an automatic, adaptive segmentation technique capable of isolating the extracellular matrix (especially the cleavage planes). This adaptive processing constitutes our second contribution.

Afterwards, in Chapter 4, we analyze two structural and geometric properties of the cleavage planes isolated in the binarized images: their positions in 3D (by extracting statistics about the distances between neighbouring cleavage planes) and their thicknesses. We show that these two structural descriptors do not vary much when moving from the epicardium to the endocardium inside the same transmural sample, but they can significantly vary between samples of the septum and of the anterior and posterior left ventricle. We have also confirmed the existence of two quasi-orthogonal populations of cleavage planes in certain regions of the left ventricle (previously reported in the literature), whose role in the cardiac motion biomechanics is certainly important. Lastly, the quantitative data that we extracted show that the thickness of the cleavage planes varies roughly between $24 \mu\text{m}$ and $59 \mu\text{m}$ and that the distance between two successive cleavage planes varies approximately between $70 \mu\text{m}$ and $280 \mu\text{m}$, with significant local variations of the standard

deviation.

Microscopic cardiac structure Structure cardiaque à l'échelle microscopique

1.1 Introduction

Cardiovascular diseases remain one of the most serious health problems in the world, motivating research that deepens our understanding of the myocardial function. This requires a good knowledge of the myocardial architecture, the myocytes and the extracellular architecture, to understand relations between mechanical function, hemodynamics and adaptive structural changes in cardiac diseases. It has been shown that increasing ventricular volume is associated with a decrease in wall thickness and fibres diameter ([Ross *et al.* (1967)], [Streeter *et al.* (1969)], etc.) and the fibres orientation determines the propagation of the electric waves in the heart and the contraction of the cardiac tissue ([Doste *et al.* (2017)], [Zhao *et al.* (2012)], [Trew *et al.* (2006)], etc). There is also a strong link between the structural remodeling and cardiac diseases ([Goblot *et al.* (2016)], etc). Despite all the effort and the advances in imaging techniques, the cardiac architecture remains controversial.

We start by presenting the main models of the cardiac structure, the main cardiac elements referred by these models, the terminology used and the confusions in terminology. These models are also linked to what can be seen with the acquisition techniques that were used in the development of the models, therefore we also dedicate a section to acquisitions.

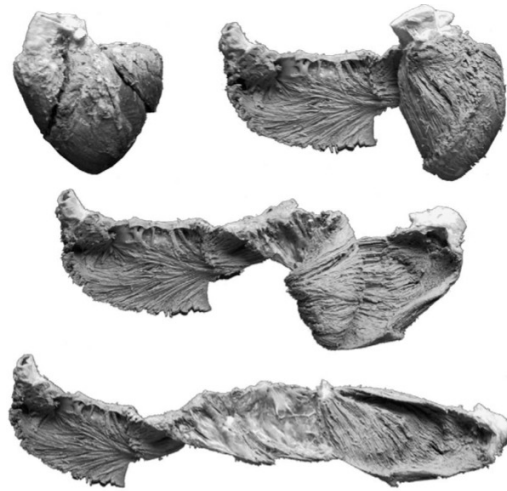


Figure 1.1: *Phases of the dissection procedure of the Torrent-Guasp's concept [Torrent-Guasp (1975)].*

1.2 Models of cardiac structure

Over time, the myocardium organisation has been widely studied and several models have been proposed. The three main cardiac models are discussed here.

1.2.1 Helical ventricular myocardial band model

The earliest description of the cardiac structure was inspired by the organisation of the skeletal muscle. Based on dissection techniques, the myocytes are considered to be grouped in distinct bundles, like the skeletal muscle. Based on this idea, several different models have been proposed ([Mall (1911)], [Robb and Robb (1942)], [Lev and Simkins (1956)], [Torrent-Guasp (1975)]). [Mall (1911)] and [Robb and Robb (1942)] introduce the idea of the helical pattern of the myocardium: four muscle bodies were proposed, anchoring on the fibrous trigones and the aortic and pulmonary roots, meanwhile [Torrent-Guasp (1975)] viewed the cardiac muscle as a single band of muscle, coiled around the aortic root and the pulmonary trunk (Figure 1.1).

In the Torrent-Guasp's concept, the helical ventricular myocardial band (HVMB) is one of the controversies of the cardiac model proposed. This model has influenced surgical procedure [Torrent-Guasp *et al.* (2001)] and the understanding of the cardiac systolic filling ([Torrent-Guasp *et al.* (2004)]), contraction and dynamics [Kocica *et al.* (2006)], [Torrent-Guasp *et al.* (2005)]. The HVMB has been rejected by some authors on the basis of histological [Anderson *et al.* (2005)], [Anderson *et al.* (2006)], optical [Jouk *et al.* (2000)], and DT-MRI [Schmid *et al.* (2005)] evidence of the smooth change in the ventricular fibre orientation across the myocardium. The HVMB has however been shown to follow a favoured path, based on observations from histological [Hort (1960)], optical [McLean and Prothero (1991)] and DT-MRI [Gilbert *et al.* (2007)] experiments.

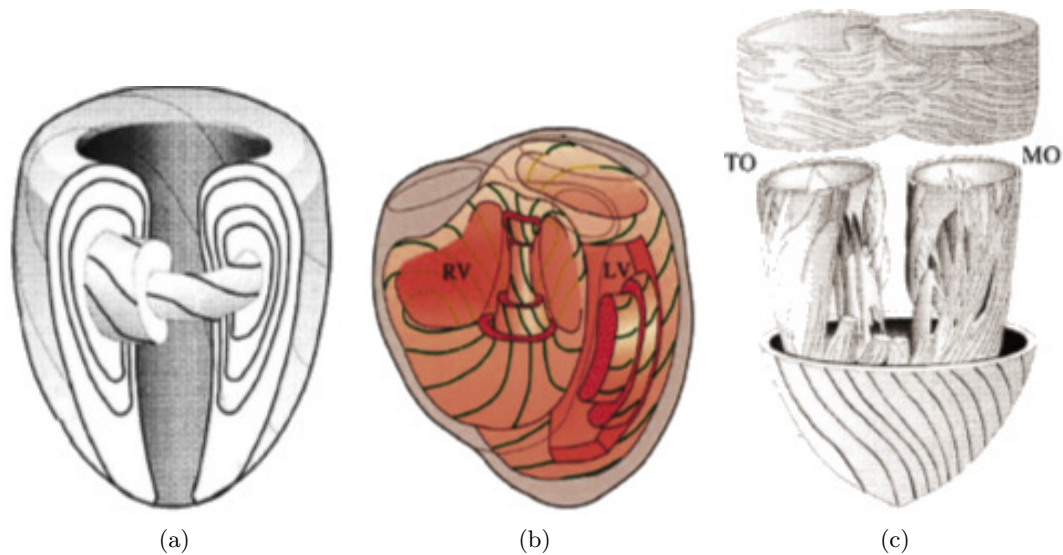


Figure 1.2: a) Doughnut (toroidal) geodesics model of the LV [Streeter (1979)]. b) Nested pretzel geodesics model of the LV and RV [Jouk et al. (2000)]. c) Three-layered ventricle [Rushmer et al. (1953)].

1.2.2 Doughnut and pretzel models

Another way of describing the cardiac morphology is based on the idea of seeing the myocardium as a vascular musculature, with branching and merging myocytes. One of the models based on this idea is the doughnut model for the left ventricle (LV) proposed by [Streeter (1979)], from the work of [Krehl (1891)] and [Hort (1960)]. Streeter used quantitative measurements of microscopic fibres angles to extract the cardiac model. This model is obtained by extracting the shortest path length of the fibres, shaped as doughnuts, of decreasing size and imbricated one in another like an onion (Figure 1.2a).

The doughnut model was later extended also to the right ventricle (RV) by [Jouk et al. (2000)], leading to the pretzel model. In this model, the fibres follow the geodesic path of two doughnuts joined side to side (pretzel) (Figure 1.2b). Another model based on the fibres path is the three-layered myocardium or the functional syncytial mesh proposed by [Rushmer et al. (1953)] shown in (Figure 1.2c), further developed by [Anderson et al. (2005)] and extended by [Greenbaum et al. (1981)], [Sanchez-Quintana et al. (1990)], [Sanchez-Quintana et al. (1995)], [Sanchez-Quintana et al. (1996)]. As the name implies, the ventricles are composed of three layers named: superficial, middle and deep layers however the model is contradictory or vague concerning the transition between layers, where evidence points to a smooth transition of principal fibre direction through the myocardium [Gilbert et al. (2007)].

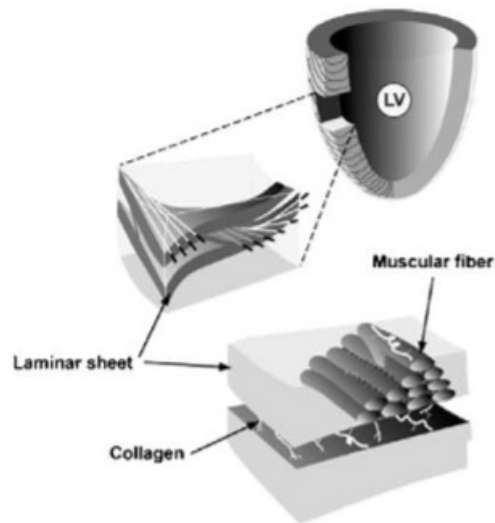


Figure 1.3: *Laminar structure proposed by LeGrice [LeGrice et al. (1995)].*

1.2.3 Myolaminae model

One idea of the cardiac micro-architecture that is receiving much attention is related to the presence of discrete muscle layers or laminar sheets of myocytes [Gilbert *et al.* (2007)]. The myolaminae model has been proposed by Hort ([Hort (1957)b], [Hort (1960)], [Hort (1957)a]), who observed the macroscopic sheets structures using dissection. “Open spaces or sliding planes between groups of muscle fiber” are noticed by [Spotnitz *et al.* (1974)], and [Grant (1965)] notes that “if the “fibres” are parallel, by the branching they form “planes” which appear to rotate”. Caulfield and Borg [Caulfield and Borg (1979)] notice that a network of extracellular matrix appears to provide tight coupling of myocytes within the sheet and looser coupling between adjacent sheets.

LeGrice *et al.* [LeGrice *et al.* (1995)] performed the first quantitative study of the myocyte laminar organisation and proposed a conceptual and mathematic model [LeGrice *et al.* (2001)], [LeGrice *et al.* (1997)], in which the myocardium is organised in ordered laminar structures, separated by cleavage planes, running radially from the endocardium to the epicardium (Figure 1.3). Costa and his colleagues [Costa *et al.* (1999)] used the same methodology as [LeGrice *et al.* (1995)] on six dogs. In three dogs they notice a generally smooth variation of the cleavage planes from epicardium to endocardium. These changes were associated with the *trabeculata compacta* interface.

1.2.4 Conclusion

The models proposed use different approaches and techniques and some of the models proposed are not compatible. A very important factor is: at which level, scale or resolution was it analysed and which techniques were used to extract the cardiac model? The existence of different non-mutually exclusive models leads also to some confusion on the

terminology used to describe them, which we address in the next section.

1.3 Cardiac tissue components

1.3.1 Myocytes

The ventricular muscle cells/ myocytes are the main structural component of the myocardium, occupying around 70% of the ventricular wall volume under normal circumstances [Villarreal (2004)]. Cardiac myocytes resemble elongated ellipsoids with a major-axis dimension of 10 to 20 μm and a length of 80 to 100 μm [Severs (2000)]. Myocytes are bunched and connected end to end by the intercalated disk [Streeter (1979)], [Cheng *et al.* (2005)].

1.3.2 Cardiac extracellular matrix

Cardiac myocytes and the vascular system are surrounded by a complex extracellular matrix (ECM), containing collagen, elastin, fibronectin, laminin and proteoglycans [Bishop and Lindahl (1999)]. The ECM is responsible for the mechanical loading of the heart and plays a central role in guiding the contractions during the systole and in helping the relaxation during diastole.

Structurally, the cardiac ECM includes: endomysium that surrounds and separates individual myocytes and capillaries, perimysium that surrounds and separates groups of myocytes and epimysium that surrounds the entire heart muscle. The perimysium extracellular matrix contains the cleavage planes as well as various components such as blood vessels, capillaries, lymphatic vessels etc. [Pope *et al.* (2008), Prado *et al.* (2002)].

1.3.3 Terminology confusion: myofibres, myolaminae, sheetlets, cleavage planes, shear layers and fibres

In skeletal muscle, a *myofibre* is a multinucleated single muscle cell. In cardiac morphology, this term has different meanings: myofibre can be synonym with myocytes [Streeter (1979)], or myofibre is used to refer to a group of minimum three myocytes surrounded by perimysial ECM [Anderson *et al.* (2005)].

Myolaminae is used to describe sheet-like structures of attached myocytes separated by cleavage planes [Cheng *et al.* (2005)]. *Laminar sheets* of myocytes are groups of myocytes surrounded by the perimysium extracellular matrix [LeGrice *et al.* (2005)]. *Sheetlets* is another term used to describe laminar arrays of myocytes [Ferreira *et al.* (2014)]. *Shear layers* [Ferreira *et al.* (2014)] and *cleavage planes* are terms used to describe the perimysium extracellular matrix. The term *fibre* is used for a continuous axial direction of individual myocytes [Fernandez-Teran and Hurle (1982)]. Gilbert *et al.* [Gilbert *et al.* (2007)] use the term *fiber* in order to denote the net axial direction of myocytes. A graphical representation of these elements is given in Figure 1.4.

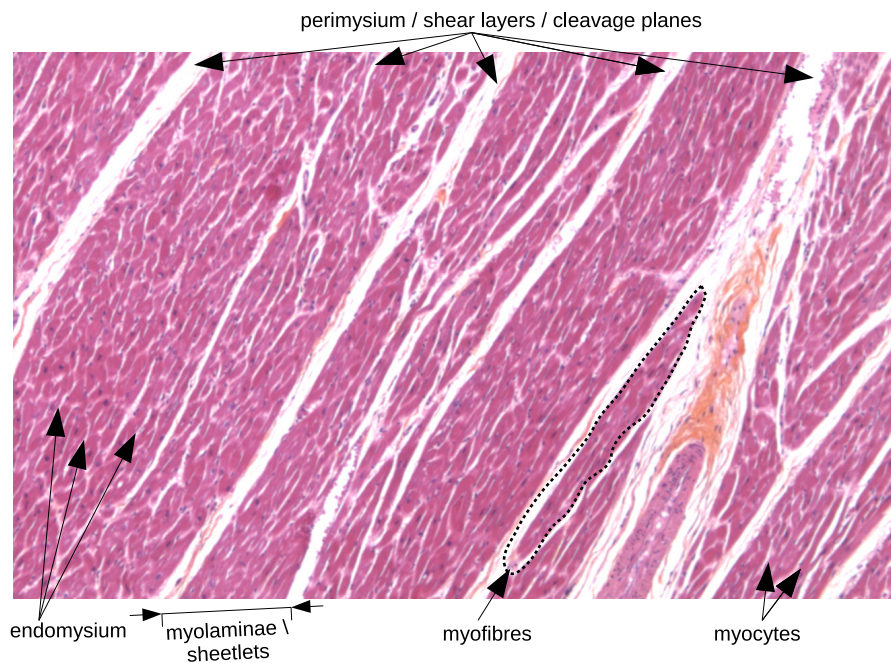


Figure 1.4: Terminology used to describe the cardiac tissue components.

1.4 Acquisition techniques

1.4.1 Dissection and histology

The most often used investigation techniques are histology and dissection. Optical images of histological sections deliver high resolution *ex-vivo*, of maximum resolution of $0.3 \mu\text{m}$ [Egerton (2005)], 2D imaging, but they can suffer from distortions when cutting the thin samples. In addition, both histology and dissection are somewhat subjective in the sense that they depend on how the researcher chose to cut the sample.

Nevertheless, histological techniques are the most used techniques in the study of cardiac structures such as sheet angles [Harrington *et al.* (2005)] for understanding the thickening mechanics during heart movements. Dual sheet orientations were presented in [Dokos *et al.* (2002)] who examined the laminar cardiac structure in six pig's hearts. They showed that "the patterns of sheet intersection were not uniform in the circumferential direction, varying significantly over sub-millimetre dimension". The two populations of laminar sheets were also reported by [Costa *et al.* (1999)] and [LeGrice *et al.* (1995)], who carried out the first quantitative histological analysis of the laminar structure of the ventricles.

In [Harrington *et al.* (2005)] the existence of two families of sheets is reported at $+45^\circ$ and -45° . $+45^\circ$ sheets are from the lateral region, near the epicardium, -45° sheets can be found in the midwall, while near the endocardium the first family is again found. They revealed, for the first time, alternating transmural families of predominant sheet angles. The study was performed using ovine hearts.

1.4.2 Electron microscopy

Despite the fact that these techniques yield important 2D morphological information, they are not fully adapted to reconstruct complex 3D microstructures that are necessary to characterize the myocardial tissue architecture in detail. High-resolution 3D techniques such as transmission or scanning electron microscopy (TEM, SEM), with a maximum resolution of 0.2 nm for TEM [Egerton (2005)] and 50 nm for SEM [Egerton (2005)]. [Weber (1989)], [LeGrice *et al.* (1995)] have been used to study the cleavage planes arrangement and their bifurcations, however those studies were limited to small tissue samples of approximately 60 μm . [Kanzaki *et al.* (2010)] and [Kanzaki *et al.* (2012)a] also used SEM to visualise the myocytes and to compare a normal heart with abnormally branched cardiomyocytes in the hypertrophic cardiomyopathy heart sample after removing the connective tissue.

The laminar distribution of the endomysial collagen / extracellular matrix has been widely analysed using electron microscopy in the human mitral papillary muscle by [Icardo and Colvee (1998)], in sheep myocardial and Purkinje cells by [Morita *et al.* (1991)] and in dog and rabbit myocardium by [Dolber and Spach (1987)] and [Prado *et al.* (2002)].

1.4.3 Confocal microscopy

Confocal microscopy can offer a very high 3D resolution, of 0.4 μm , but cannot acquire large image volumes (35 μm) [Pope *et al.* (2008)], [Young *et al.* (1998)]. Confocal microscopy has been used to study the excitation-contraction in cardiac myocytes [Sachse *et al.* (2009)]. Confocal microscopy can deliver very high resolution, but the field of view is narrow (35 μm). Some of the significant studies related to the 3D cardiac microstructure are performed by [Young *et al.* (1998)], [Sands *et al.* (2005)], [LeGrice *et al.* (2004)]. Confocal microscopy allows a depth of 60-80 μm , however these studies extended the confocal microscopy technique to allow the reconstruction of larges 3D images of sample volumes from a series of optical sections through thick tissue specimens (35 μm).

1.4.4 Polarized Light Imaging

Polarized Light Imaging (PLI) can be used to obtain maps of the orientation of myocardial cells in larger volumes but at a lower resolution. The width of the voxel can vary according to the degree of enlargement of the objective lens that runs from 10 μm x 10 μm to 500 μm x 500 μm , while the thickness is 500 μm [Jouk *et al.* (2007)]. In [Desrosiers *et al.* (2012)], [Jouk *et al.* (2007)], a fetal heart was divided into a set of parallel contiguous slices and each slice was imaged with PLI, thus constructing a 3D map of the myocyte orientations in the entire heart at a resolution of 100 μm x 100 μm x 500 μm . This resolution remains insufficient for visualizing individual myocytes, and what is actually seen is the averaged orientation of a population of myocytes in each voxel.

1.4.5 Magnetic Resonance Imaging

Compared with the previous techniques, Magnetic Resonance Imaging is non-invasive and can be used *in-vivo* to image the entire heart. Diffusion Tensor MRI (DT-MRI) can recover the dominant orientation of myocytes in each voxel because of the stronger diffusion of water molecules in the direction parallel to that of the myocytes. DT-MRI can thus map myocyte orientations throughout the entire heart *in-vivo* and can serve to detect abnormalities [Wang *et al.* (2012)], [Ferreira *et al.* (2014)].

In [Helm *et al.* (2005)b], [Helm *et al.* (2005)a], [Helm *et al.* (2006)] MRI was used to analyse the laminar architecture. They also reported two types of laminar sheets and inter-individual variations of sheet orientations with a bimodal distribution, as did [Kung *et al.* (2011)]. The sheet reconstructions show the same pattern of stacks of sheets in several studies using MRI on dogs [Helm *et al.* (2006)], mouse [Jiang *et al.* (2004)], rabbit [Helm *et al.* (2006)], rat [Chen *et al.* (2005)]. MRI has also been used to investigate the cardiac anisotropy [Bernus *et al.* (2015)].

The cardiac microstructure was investigated by [Axel *et al.* (2014)], pointing out the difficulty of the *in-vivo* DTI of the heart, “due to the technical challenge of probing for incoherent diffusion motion (on the order of microns) on a background of much larger coherent bulk wall motion (on the order of millimeters)”. However, the typical spatial resolution of MRI is low (1 mm x 1 mm x 2 mm) therefore the 3D organisation of myocytes at a microscopic level remains unknown. High-resolution MRI setups such as [Baltes *et al.* (2009)] can achieve $30\ \mu\text{m} \times 30\ \mu\text{m} \times 300\ \mu\text{m}$ or $60\ \mu\text{m} \times 60\ \mu\text{m} \times 60\ \mu\text{m}$ voxel sizes, but even this remains above the diameter of cardio-myocytes.

1.5 Conclusion

As can be noted, the type of imaging acquisition technique is very important for the analysis of cardiac tissue, but Fox and Hutchins [Fox and Hutchins (1972)] point out that “The only level of the network of cells that can be referred to accurately as a fibre is a single cell. The “fibre” is often only one cell in length before it splits and branches”. Therefore, a precise understanding and characterisation of the cardiac structure requires a 3D imaging technique that allows visualising individual cells, and in large samples in order to capture not just the local but also the higher-level organisation. The next chapter deals with the imaging technique that allows us to accomplish precisely that.

Cardiac microarchitecture using 3D X-ray Phase Contrast μ -CT Imagerie 3D du tissu cardiaque par μ -CT en Rayons X à Contraste de Phase

2.1 Introduction

This chapter starts with the image acquisition process at the European Synchrotron Radiation Facility (ESRF): after a short general description about what the ESRF is and how it works, we describe the experimental setup used to acquire the 3D X-ray Phase Contrast μ -CT images, as well as the human heart samples that were imaged.

Afterwards, we draw a parallel between what can be seen in “classical” histology images versus what we can see in 3D X-ray Phase Contrast μ -CT images of the heart samples, this process allows us to interpret these new images.

We proceed with a detailed examination of the 3D images of some representative samples, identifying the main tissue components visible in the images, examining their structure in 3 dimensions (which was never done before to such an extent) and qualitatively comparing the tissue arrangements between the displayed samples. Complementary examples are given in Appendix A.

2.2 What is the ESRF?

The European Synchrotron Radiation Facility (ESRF) is a particle accelerator located in Grenoble, France, used as an X-ray source 100 billion times brighter than those used in hospitals, its main application being the investigation of matter down to the most minute detail, even at the atomic level.

The basic functioning principle of the ESRF is the following: when high-energy electrons circulating in a storage ring are deflected by magnetic fields, they produce what is called *synchrotron light*, in the form of X-rays in the case of the ESRF. The electrons need to have a very high energy (6 GeV), this is why a particle accelerator is needed.

The ESRF is composed of a linear accelerator (LINAC), in which electrons generated from an electron gun are packed into bunches at the start of the LINAC, and then gradually accelerated by electromagnetic waves until they are traveling close to the speed of light. After the LINAC, the electrons are injected into the booster synchrotron, a ring with a circumference of 300 meters. The electrons travel around this ring many thousands of times, at each lap gaining a little more energy, until they reach their target energy of 6 GeV. They are then inserted into the storage ring (Figure 2.1).

The storage ring has a circumference of 844 metres, in which the electrons travel for hours in high-vacuum conditions. All along the circumference of the storage ring, there are several types of magnets: bending magnets, undulators and focusing magnets. As the electrons pass along a magnet, they are forced to change direction, and in the process, they lose some of their energy and emit synchrotron radiation.

The bending magnets are the ones forcing the electrons to change direction and travel in a circle through the storage ring. They are also a source of synchrotron light, which is emitted tangentially to the curved path of the electron beam and is directed towards the *beamlines*. The undulators are a series of small magnets with alternating polarity, in which the electrons release X-rays a million times more intense than those produced in the bending magnets; these X-rays have brightness and coherence properties that are close to lasers. The focusing magnets are there to ensure that the electron beam is as narrow as possible.

All around the storage ring there are a series of *beamlines*, in which the actual experiments take place. A beamline consists of an optics cabin, an experimental cabin and a control cabin. The optics cabin contains X-ray optics designed to modify the X-ray beam coming from the synchrotron to suit the experiment being performed; they can focus the beam or select desired wavelengths, or energies. The experiment cabin is where the sample to analyse is placed. Depending on the experiment, there might be apparatus to keep the sample in certain conditions (temperature, pressure etc.) and the workspace may include devices to position the sample precisely with respect to the beam. Around the sample there are detectors whose role is to record the X-rays that pass through, are reflected or are scattered by the sample.

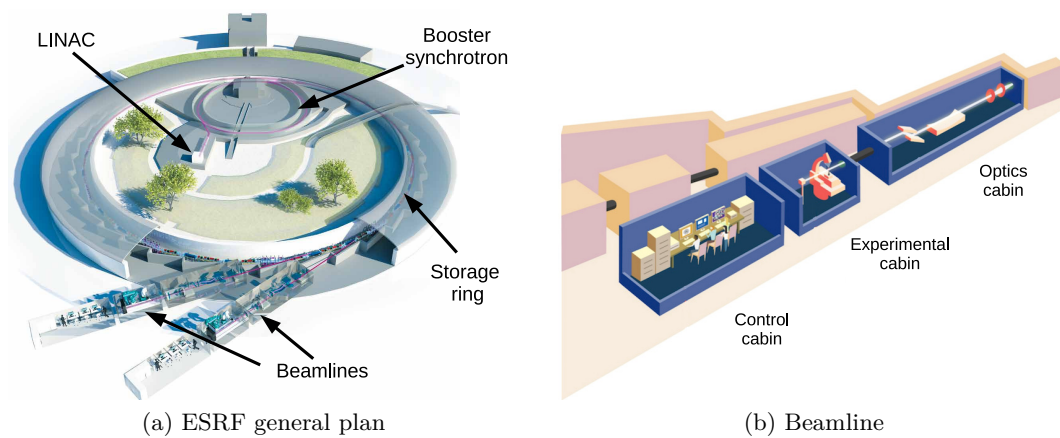


Figure 2.1: a) ESRF: electrons are generated at the start of the Linear Accelerator (LINAC), accelerated through the LINAC and the booster synchrotron up to 6 GeV, then they are injected into the storage ring. The synchrotron radiation in the form of X-rays is released into beamlines (placed all along the storage ring), in which the actual experiments are carried out. Adapted from the ESRF brochure “A Brilliant Light For Science”, <http://www.esrf.eu/home/education/resources.html>.

b) A beamline is composed of an optics cabin, where the X-ray beam is prepared, an experimental cabin, where the sample and the detectors are placed, and a control cabin for the operators. Adapted from <http://www.esrf.eu/about/synchrotron-science/beamline>

2.3 Synchrotron radiation μ -CT setup at beamline ID19

Typical μ -CT is based on absorption contrast, which is directly linked to the density of different elements of the sample. In soft tissue such as heart samples, absorption contrast is poor, however *phase contrast*, meaning how much the X-rays are *delayed* in the tissue, is much more pronounced and this is what we use [Cloetens *et al.* (1999)]. One of the simplest phase contrast setups is called *in-line propagation*. It consists in placing the detector further away from the sample and recording interference patterns formed by the beam crossing the sample. This is where synchrotron radiation is useful, as the technique requires coherent X-ray radiation, which conventional sources cannot produce. After the 3D tomographic reconstruction, the obtained 3D image represents the phase decrement index of each voxel.

The actual setup at beamline ID 19 (Insertion Device 19) consisted of X-ray radiation at 19 keV with a bandwidth of $\sim 1\%$. To obtain phase contrast, the detector was placed 750 mm behind the sample [Snigirev *et al.* (1995)]. The detector is composed of a scintillator (converting X-rays to visible light), a lens system (to focus the light on the sensor and adjust magnification) and a CCD sensor. The optical setup was chosen to yield a voxel size of $3.5 \mu\text{m}$ using the 2048×2048 FReLoN (Fast Readout Low Noise) camera developed at ESRF [Labiche *et al.* (2007)].

3D reconstruction of the sample’s interior requires the acquisition of several projections through the sample. To this end, the sample is placed on a stage and a large set of projections is acquired, each at a slightly different angle, spanning a range of 180° or

360° [Salomé *et al.* (1999)]. 3D reconstruction was done using the software developed by [Weitkamp *et al.* (2011)].

2.4 Data reconstruction

2.4.1 Absorption CT

The ability of a material to attenuate X-rays depends on its atomic number. The relationship between the X-ray beam attenuation and the material properties is described by the Beer-Lambert law. Let $\mu(X)$ (where $X = (x, y, z)$ is the voxel coordinates) be the 3D linear attenuation coefficient of the material, for a X-ray beam of wavelength λ , and $p_\theta(u, v)$ the projection of the material on a 2D detector (u, v) , at the angle θ . According to the Beer-Lambert law, the 2D projection can be expressed as:

$$p_\theta(u, v) = \ln \left(\frac{I_\theta^0(u, v)}{I_{\theta,0}(u, v)} \right) = \int_{D_{\theta,u,v}} \mu(x, y, z) ds \quad (2.1)$$

where $I_\theta^0(u, v)$ is the X-ray intensity of the incident beam and $I_\theta(u, v)$ is the X-ray intensity of the beam having passed through the material. $D_{\theta,u,v}$ is the X-ray path joining the punctual X-ray source and the pixel (u, v) on the detector.

The solution of the inverse problem (equation 2.1), provides the 3D attenuation coefficient $\mu(X)$ of the material. It is obtained from a set of 2D projections $p_\theta(u, v)$ acquired at different angles. This inverse problem can be solved using either *analytical* techniques, such as the Filtered Back Projection (FBP) algorithm [Bracewell and Riddle (1967)]:

$$\mu(x, y, z) = \int_0^\pi \tilde{p}_\theta(x \cos \theta + y \sin \theta, z) d\theta \quad (2.2)$$

where $\tilde{p}_\theta(u, v)$ is the projection filtered with a conventional 1D ramp filter, or *algebraic* techniques such as the ART, SMART, SIRT algorithms.

2.4.2 Absorption and phase CT

Biological tissues consist of components whose linear attenuation coefficients are low and very similar, explaining why conventional X-ray absorption imaging does not provide sufficient contrast. An efficient way to increase contrast consists in recording X ray phase information.

Several phase retrieval algorithms have been developed: phase-attenuation using Born and Rytov approximation ([Gureyev *et al.* (2004)]), phase attenuation duality algorithm ([Wu and Liu (2005)]), modified Bronnikov algorithm proposed by Groso and his colleagues ([Groso *et al.* (2006)] by introducing a correction factor, the phase-attenuation duality algorithm proposed by Wu and al. ([Wu and Liu (2005)]), the transport of intensity equation solution proposed by Paganin and his coworkers ([Paganin *et al.* (2002)])

One of the simplest method when a signal propagation distance is used is the Paganin's method [Paganin *et al.* (2002)]. Paganin's method is based on the assumption that the object is homogeneous (an assumption fulfilled in soft tissue) thereby assuming a proportionality between the linear attenuation coefficient and the phase index. The proportionality factor- is a parameter of the algorithm and depends on the composition of the sample and the energy used. The method relies on the transport of intensity equation approach, which in this particular case can be expressed as a simple frequency filtering in the Fourier domain of the image intensity. We used the Paganin's method for reconstructing our samples.

2.5 Heart samples collection and preparation

Ten fresh human heart samples were supplied by the Medico-Legal Institute of Lyon IML HCL ($n^{\circ}DC - 2012 - 1588$), taken from the hearts of two males aged 32 and 35 years. These patients suffered a violent death, had no past medical history, no treatment and no addiction. Less than 24 h after death, the hearts were removed and preserved in a 10% formalin solution to ensure good preservation, prior to their examination by the forensic pathologist. A slight shrinkage effect due to the formalin solution was present but limited by the short time between death and the imaging procedure. Fixation by formalin is the most routinely used technique in histology. In the heart study, this method has provided the assessment of the arrangement/orientation of the myocardial fibres for many decades [Veinot *et al.* (2001)]. The only artifacts reported with the formalin fixation are the formalin pigment sedimentation or the modification of the tissues due to a lack of fixation time [Dettmeyer *et al.* (2013)].

The samples were extracted from the septum and the left ventricle (LV) walls of the heart. They belonged to slices 1, 2 and 5 (Figure 2.2). The samples extracted from heart no. 1 belong to slice 5. Those extracted from heart no. 2 belonged to slices 1 and 2. The thickness of each slice was roughly 5 mm. The distance between two slices depended on the size of the LV. Slice 1 was close to the base, slice 2 was around a third of the distance from the base and slice 5 lay close to the apex. The length of the samples depended on the local thickness of the wall (details given in Table 2.1).

To improve image contrast, the tissue samples had to be transferred into ethanol before imaging. The samples were first rinsed in deionised water, plunged into a demineralised water bath for rehydration and immersed in successive baths (lasting 30 min) increasing the ethanol concentration from 10% to 70% in 10% steps. Finally, each sample was placed in a plastic container 7 mm of diameter before X-ray imaging (Figure 2.3). The imaging setup used in this experiment is non-destructive for the sample.

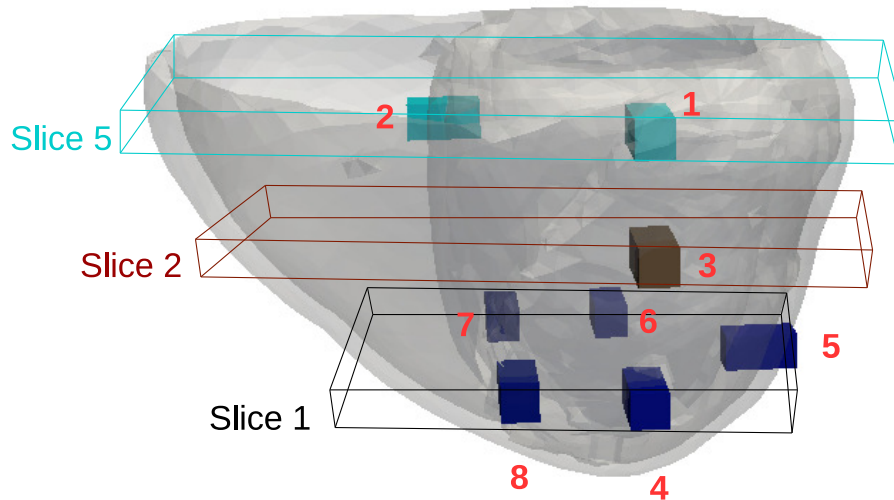


Figure 2.2: Location of the 8 samples extracted from two human hearts. Slice 5 comes from heart no. 1. Slices 1 and 2 come from heart no. 2. Slice 5 contains samples 1 and 2. Slice 2 contains sample 3. Slice 1 contains samples 4, 5, 6, 7 and 8. See Table 2.1. Adapted from [Varray et al. (2017)].



Figure 2.3: Cardiac samples placed in test tubes, prior to image acquisition at the ESRF.

Sample n°	Sample	Acquisition name	Location	Heart	Slice	Length (mm)	Length (voxels)
1	LV_ant_S5_1	t5_ech18	Left ventricular anterior	1	5	22.2	6350
2	S_post_S5_1	t5_ech19_20	Septum posterior	1	5	15.6	4450
3	LV_ant_S2_2	t2_VGant	Left ventricular anterior	2	2	16.9	4820
4	LV_ant_S1_2	t1_VGant	Left ventricular anterior	2	1	15.6	4420
5	LV_lat_S1_2	t1_VGlat	Left ventricular lateral	2	1	15.9	4550
6	LV_post_S1_2	t1_VGpost	Left ventricular posterior	2	1	15.9	4550
7	S_ant_S1_2	t1_septumant	Septum anterior	2	1	16.8	4810
8	S_post_S1_2	t1_septumpost	Septum posterior	2	1	18.6	5300
9	S_antposta_S2_2	t2_septumantposta	Septum anterior-posterior	2	2	25	7807
10	S_antpostb_S2_2	t2_septumantpostb	Septum anterior-posterior	2	2	25	7807

Table 2.1: Description of the samples imaged at the ESRF. Slices 1 and 2 belong to heart no. 2 and slice 5 to heart no. 1. The length of the eight reconstructed tissue samples depends on the local thickness of the wall (z -axis). Each voxel measures $3.5 \mu\text{m}$. See Figure 2.2 for a graphical representation.

2.6 X-ray phase contrast tomographic imaging of the acquired samples

For each sample we acquired 2499 projections, each one lasting ~ 0.4 s. yielding a total acquisition time of ~ 20 min sample piece. Due to the maximum height allowed by the detector (smaller than the height of the samples), several successive acquisitions were performed for each sample (3-5 acquisitions for samples from heart no. 2, and 9 acquisitions for samples from the heart no.1). An overlap of 97 voxel planes (0.34 mm) was insured between acquisitions when shifting the sample vertically. These acquisitions were merged to recreate the entire volume of each sample. For the $15\text{ mm} \times 6\text{ mm} \times 6\text{ mm}$ sample in Figure 2.4, the total acquisition time of all pieces is 1 h 17 min.

Phase retrieval was done at each projection angle using the algorithm from [Paganin *et al.* (2002)]. This algorithm assumes homogeneous objects, an assumption fulfilled in soft tissue. After phase retrieval, reconstruction was done using filtered backprojection yielding $2048 \times 2048 \times 2048$ voxels for each scan. The final dimensions of the reconstructed volumes after removing the overlapping slices by post-processing are given in Table 2.1.

2.7 3D phase contrast image interpretation

For illustration purposes we choose a small part of a sample from the inferior part of the left ventricle, at the junction between the apical third and the equatorial third (t1_VGpost), as illustrated in Figure 2.4, to be compared with a 2D histological section from a region contiguous to the 3D μ -CT section. The small part of the posterior left ventricle sample (t1_VGpost) is presented in Figure 2.6 and contains 0.44×10^9 voxels for a file size of 1.75 GB. The 3D visualisation was made with CreaTools [Serrano *et al.* (2012)], a software tool created in the CREATIS lab.

Three orthogonal planes are shown in order to illustrate different types of details that can be seen. The plane orthogonal to the X axis illustrates projections of myocyte orientations appearing as long, thin filaments. The lumen of a blood vessel can be seen with round shaped erythrocytes.

It is interesting to compare the X-ray phase contrast images with optical images of histological sections. To this end, Figure 2.5b depicts such a histological image taken from approximately the same area of the heart as Figure 2.5a and with a similar slice orientation ([Mirea *et al.* (2015)]). Figure 2.5d is another histological section, but with approximately the same location and orientation as Figure 2.5c. The two image pairs in Figure 2.6 are structurally similar. In the above pair, myocytes appear as long, filament-like structures (white in the X-ray phase-contrast images, red in the optical images). The endomysium extracellular matrix that surrounds the myocytes and capillaries appears as thin, black lines in Figure 2.5a and as thin, white lines in Figure 2.5b. For the other image pair, myocytes are separated by thin, short, curved areas, and bundles of myocytes are separated by long, straight areas. The long straight areas form the perimysium extracellular matrix,

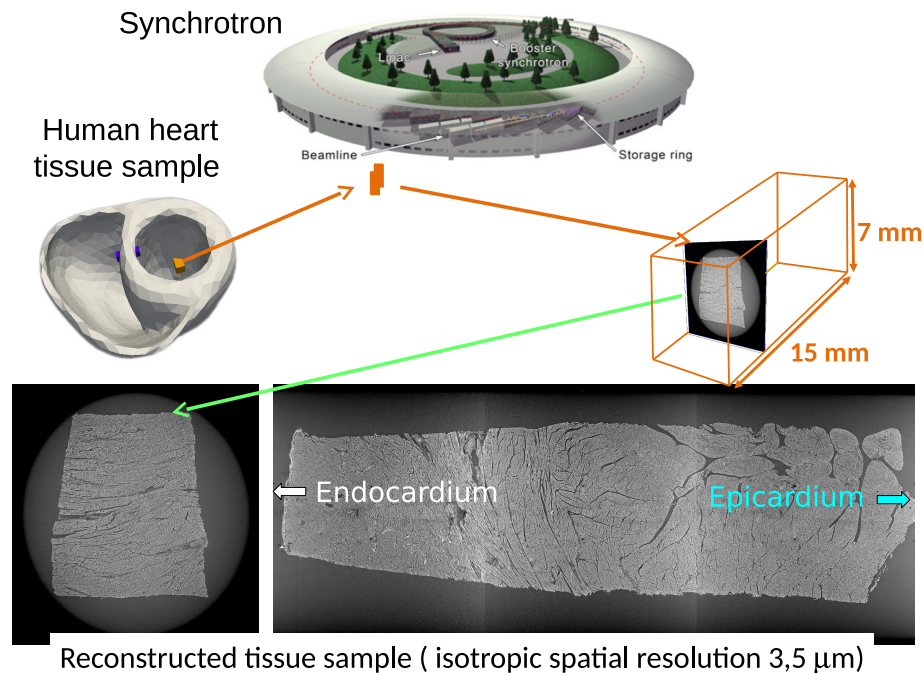


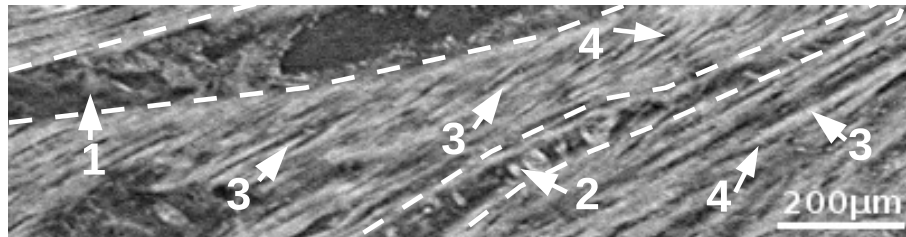
Figure 2.4: At the ESRF, we acquired a large set of angular projections through each sample, from which the 3D volume was reconstructed. A transverse section through the sample placed in the test tube, as well as a longitudinal section from epicardium to endocardium of the 3D reconstructed sample are shown.

which in 3D are planar structures, as can be seen in the next subsection, where they will be referred to as cleavage planes (CP).

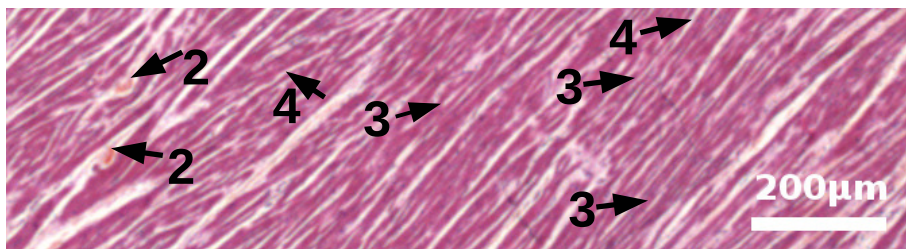
A 3D ROI extracted from the posterior left ventricle, slice 1 (t1_VGpost) at a distance of 2 mm from the epicardium is presented in Figure 2.7. A gray-level reversal has been applied, to have the extracellular matrix in white, like in the optical images of histological sections. In Figure 2.7a, numerous myocytes (dark) are visible in transversal section (M), surrounded by a continuous network of endomysium collagen (light) (E). The perimysium (light) (P) network separating groups of myocytes can also be seen. A large cleavage plane is also present. An arteriole (A) running inside the cleavage plane is visible in transversal section, as well as a lymphatic vessel (LV) in transversal section. The three layers of the venule and arteriole walls can be clearly seen. Many adipose cells (AC) lie in the vicinity of the blood venules (BV). In Figure 2.7b we show a section parallel to the CP from Figure 2.7a. The lymphatic vessel, the blood venule and the arterioles are visible in longitudinal section. We can also see myocytes in longitudinal section.

2.8 Cardiac microarchitecture from different locations of the human heart

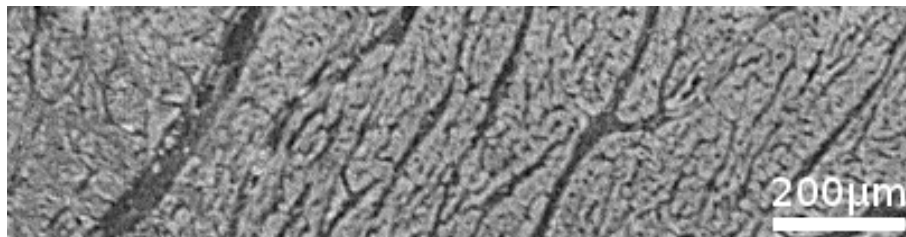
We now present three transversal samples: posterior septum, anterior septum and posterior left ventricle in order to understand the organisation of the CP structures. It is



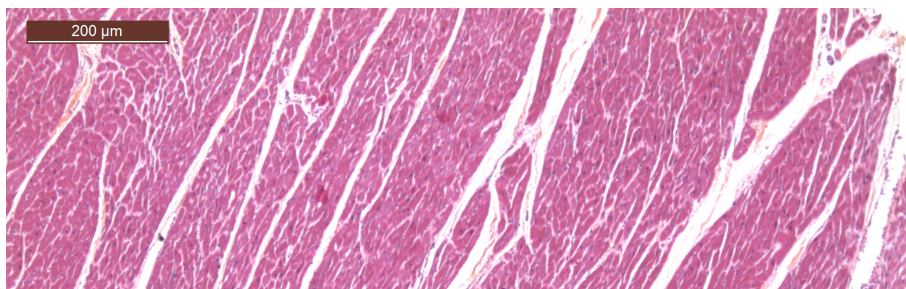
(a) X-ray phase contrast image, X plane



(b) histological section, X plane



(c) X-ray phase contrast image, Y plane



(d) histological section, Y plane

Figure 2.5: a) X-ray phase contrast image section perpendicular to the X axis (see Fig. 2.6); 1 - blood vessel; 2 - capillary with red blood cells; 3 - projections of myocyte orientations (white); 4 - intercellular space (black). b) histological section similar to a) [Eroschenko (2008)]. Both a) and b) show myocytes as thin long filament-like structures. c) X-ray phase contrast image section perpendicular to the Y axis. d): histological section similar to c). Both c) and d) show myocytes and bundles of myocytes.

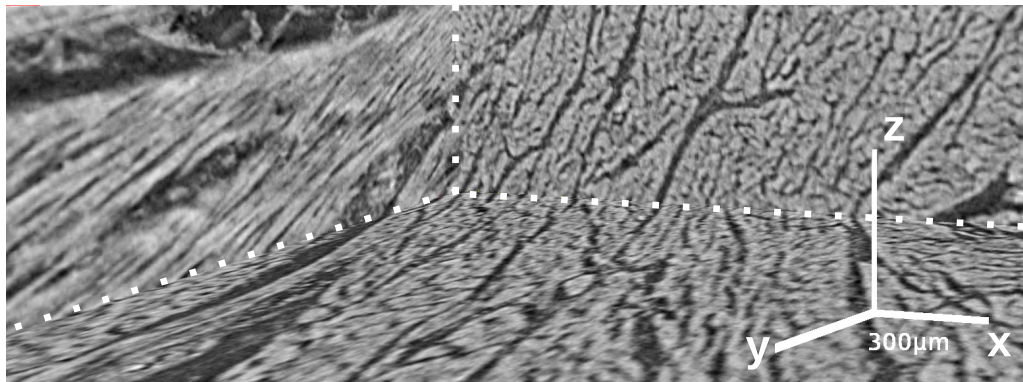


Figure 2.6: X-ray phase contrast 3D image of a heart sample from the inferior part of the lateral wall of the left ventricle.

the first time that we see this organisation at such a high resolution in 3D. The organisation of the CP will be analysed quantitatively in Chapter 4.

2.8.1 Cardiac microarchitecture of the posterior septum (sample 8)

One of the main controversial architectures is that of the septum. Several researchers emphasize the idea that there exists a 'natural entrance' into the ventricular wall. After performing a study on 25 normal postmortem human hearts using dissection and histology of sections in two orthogonal planes, Greenbaum and his colleagues state that "the septum is formed from subendocardial fibers of the right and left ventricle together with a middle layer composed of circumferential fibers continuous with those from the corresponding layer of the free wall of the left ventricle" [Greenbaum *et al.* (1981)].

Later, Jouk *et al.* [Jouk *et al.* (2000)] performed a study on 18 midgestation fetal human hearts using quantitative polarized light microscopy. They describe the septum in a similar manner, as a trilaminar structure like a sandwich of orthogonal sub-endocardial fibers and in the middle a layer of latitudinal fibers. They point out that "fibers of the latitudinal layer of the septum are potentially able to make contact at its upper or lower parts with similarly oriented fibers of the latitudinal layers of the right or left ventricle". They also remark that a lack of connectivity of the layers implies a change in the orientation of the muscle fibers. Anderson and his colleagues [Anderson *et al.* (2005)] reported at the base of the left ventricle a distinct collection of circular fibers oriented parallel to the ventricular equator.

There are also groups of researchers that emphasize the idea that there is no layer ('controlled incision' or 'blunt disruption') that connects the left and right ventricles. They consider that the intact ventricles are "naturally well coupled, both anatomically and functionally", so that "two hearts can beat as one" [Yacoub (1995)].

A 3D transmural section from the posterior septum is presented in Figure 2.8. The layers of perimysial extracellular matrix (cleavage planes), and the laminar sheets of myocytes can be clearly seen. The perimysial extracellular matrix is organised in planar

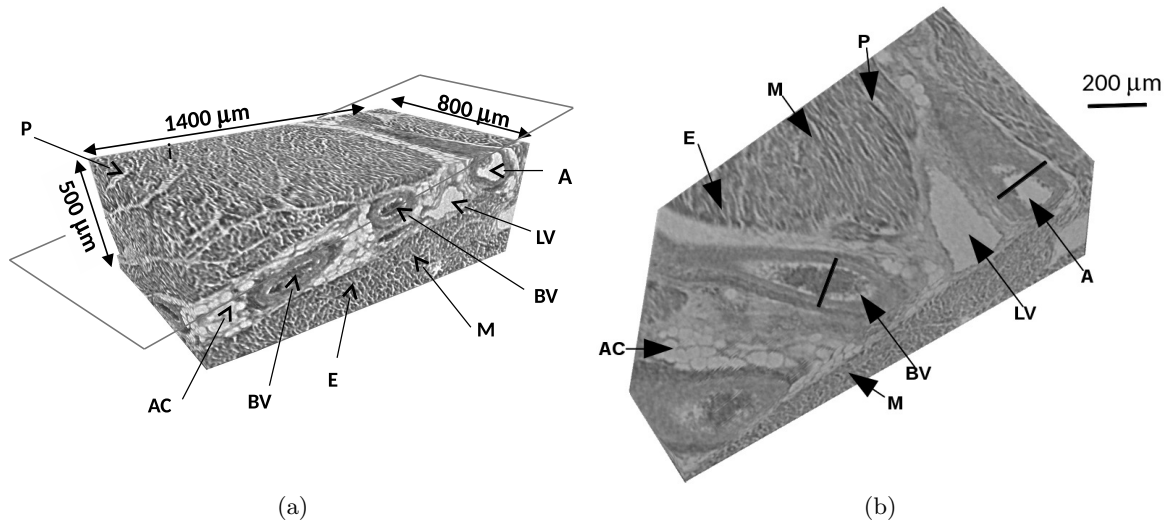


Figure 2.7: (a): 3D ROI of the posterior left ventricle, slice 1 (LV_post_S1_2). M = myocytes (dark), E = endomysium collagen (light), P = perimysium network (light), A = arteriole inside a cleavage plane, LV = lymphatic vessel, AC = adipose cells, BV = blood venules. (b): sectioning plane (shown in blue on the left subfigure) crossing vessels embedded in the cleavage plane.

structures that bifurcate and reunite, surrounding various numbers of myocytes.

The two faces of the transmural parallelepiped (the top face and the front face as displayed in Figure 2.8) show how the perimysial extracellular matrix is organised in 3D. On the front face, the layers of extracellular matrix, the cleavage planes, are parallel and very numerous close to the left ventricle. On the top face we see that the cleavage planes in fact split/bifurcate surrounding groups of myocytes, and are not straight. Their orientation is changing smoothly as we approach the right ventricle portion, also the distances between planes are gradually increasing and the density of planes decreases (Figure 2.8).

The transmural parallelepiped will be split in 4 blocks for zooming in on the cardiac structure. In block (d) (Figure 2.9), the three faces displayed illustrate different aspects of

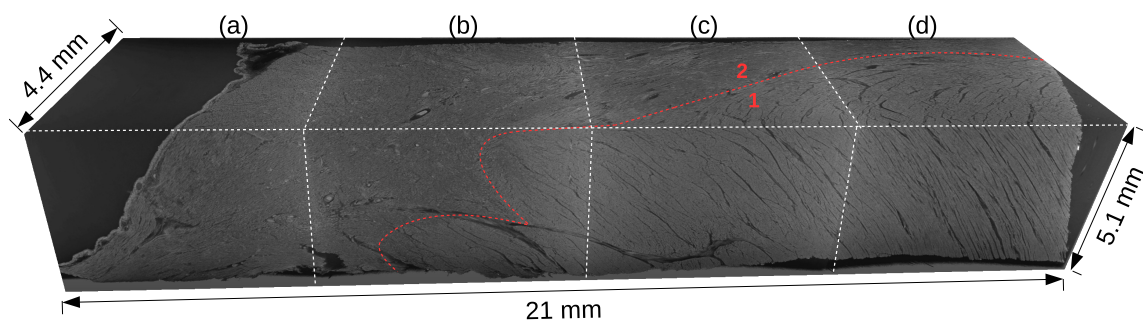


Figure 2.8: 3D reconstructed volume of a posterior septum sample (S_post_S1_2) imaged using 3D X-ray Phase Contrast μ -CT. The red curve separates two regions of different micro-architecture. The region 1 shows many cleavage planes with smoothly changing orientation comparatively to the region 2.

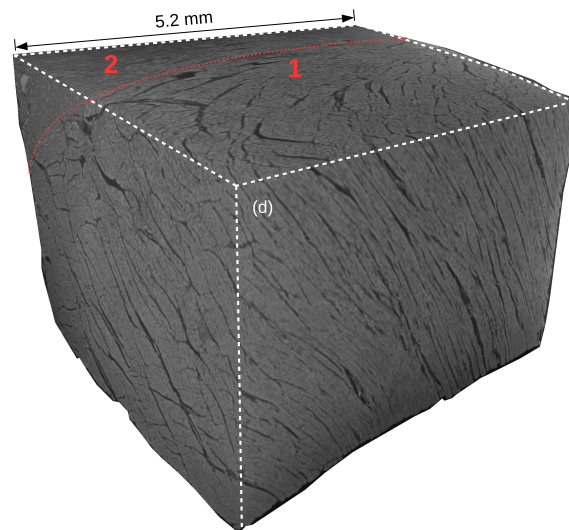


Figure 2.9: *Zoom-in on the rightmost cube (d) of the posterior septum sample shown in Figure 2.8.*

the 3D structure. The bottom-right face shows cleavage planes that are parallel and very dense, with the orientation varying smoothly. The other faces of the block are shown in more detail in Figure 2.10b.

The sections (d1) (Figure 2.10b) and (d2) (Figure 2.10c) are somewhat similar in structure, and in each of them we see two organisation patterns, one corresponding to the left ventricle and the other to the right ventricle. The separation zone between the left and right ventricles can be clearly seen as a change in texture and is marked with black arrows in both (d1) and (d2). It is noteworthy that in the zone corresponding to the RV, the myocytes are oriented in the same direction and the perimysium is very thin. In the other zone corresponding to the LV, the organisation is more fragmented, with groups of myocytes surrounded by the cleavage planes of the perimysial extracellular matrix (red arrows and red ellipses, Figure 2.10c and Figure 2.10b) creating different imbricated shapes (circular, square...) showing many splits and merges.

At least two cleavage plane populations characterized by different orientations can be seen in Figure 2.10. The reason for this fragmentation of the myocytes by the perimysium may be the required *freedom of movement* in different directions during contractions. Similar structures with two populations of cleavage planes of different orientations can be seen in the reconstruction of a transmural block using confocal microscopy [Sands *et al.* (2005)] (Figure 2.11), however the authors do not mention them in their publication.

In the next block from the posterior septum (Figure A.1), the cleavage planes are less dense but they are still parallel to each other (Figure A.1d and Figure A.1c). The volume corresponding to the right ventricle occupies a larger part of the subsample than in Figure 2.9. We can still observe a smooth variation in the orientation of myocytes throughout this subsample.

In the subsample from Figure A.2b almost the entire volume is occupied by the right

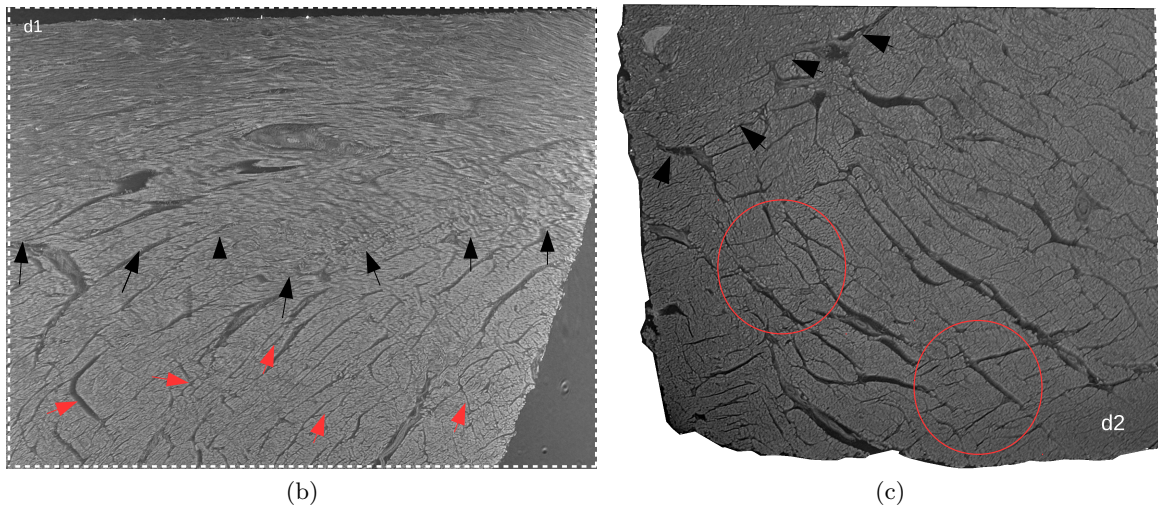
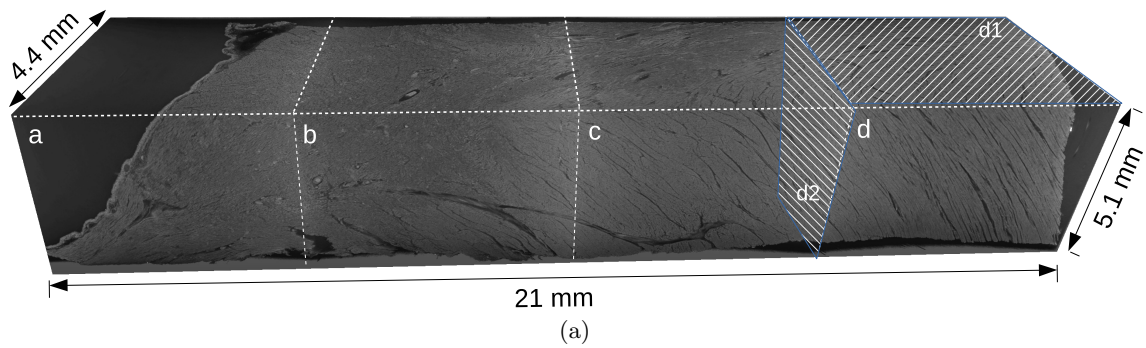


Figure 2.10: Zoom-in on two orthogonal sections through the posterior septum sample from Figure 2.8. Each of these sections shows two organisation patterns, one corresponding to the region 1 and the other to the region 2. The approximate separation between patterns is indicated by the black arrows. Some cleavage planes are indicated by red arrows and red ellipses.

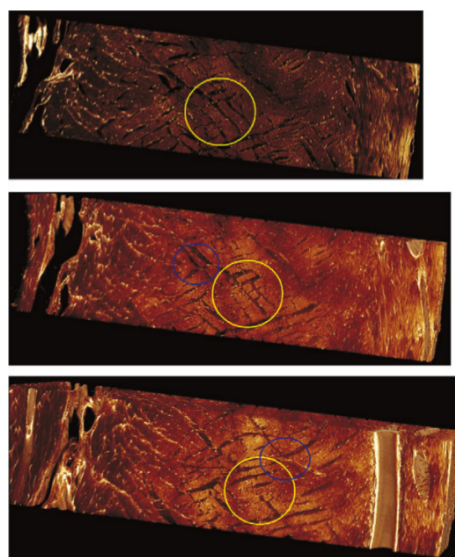


Figure 2.11: Myocytes surrounded by the cleavage planes are revealed through serially confocal imaging by [Sands et al. (2005)]. [Gilbert et al. (2007)] notice the two co-existing sheet populations.

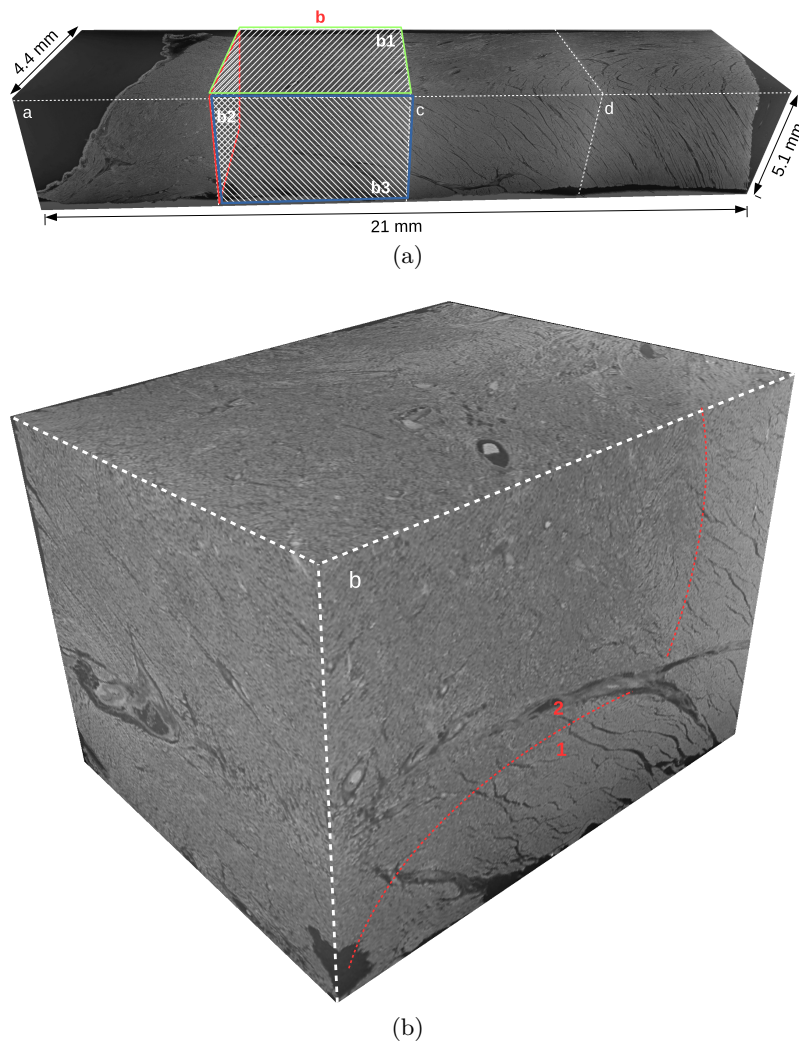


Figure 2.12: Zoom-in on the subsample marked (b) of the posterior septum sample from Figure 2.8. The red dashed line marks the approximate separation between the two regions.

ventricle, in which the myocytes are very dense and the cleavage planes cannot be clearly seen. If we examine Figure A.3b, we see that the group of myocytes changes direction suddenly. In Figure A.3c, tiny, parallel cleavage planes can be seen with smoothly varying orientation. In Figure A.3d we can again see the separation between the left and right ventricles as an abrupt change in texture.

The last posterior septum part that we examine is shown in Figure A.4a and Figure A.4b. In this region, myocytes are organised in compactly, separated by thin cleavage planes (see Appendix A). The myocytes are visible mainly in transverse section in Figure A.4c and in longitudinal or in oblique section in Figure A.4d (see Appendix A). It is very evident in Figure A.4d how the myocytes are parallel to the pericardium.

To conclude, the 3D transmural section from the posterior septum presents two cardiac organisation patterns. One of the patterns is described by parallel cleavage planes with ramifications. The cleavage planes smoothly change their overall orientation from

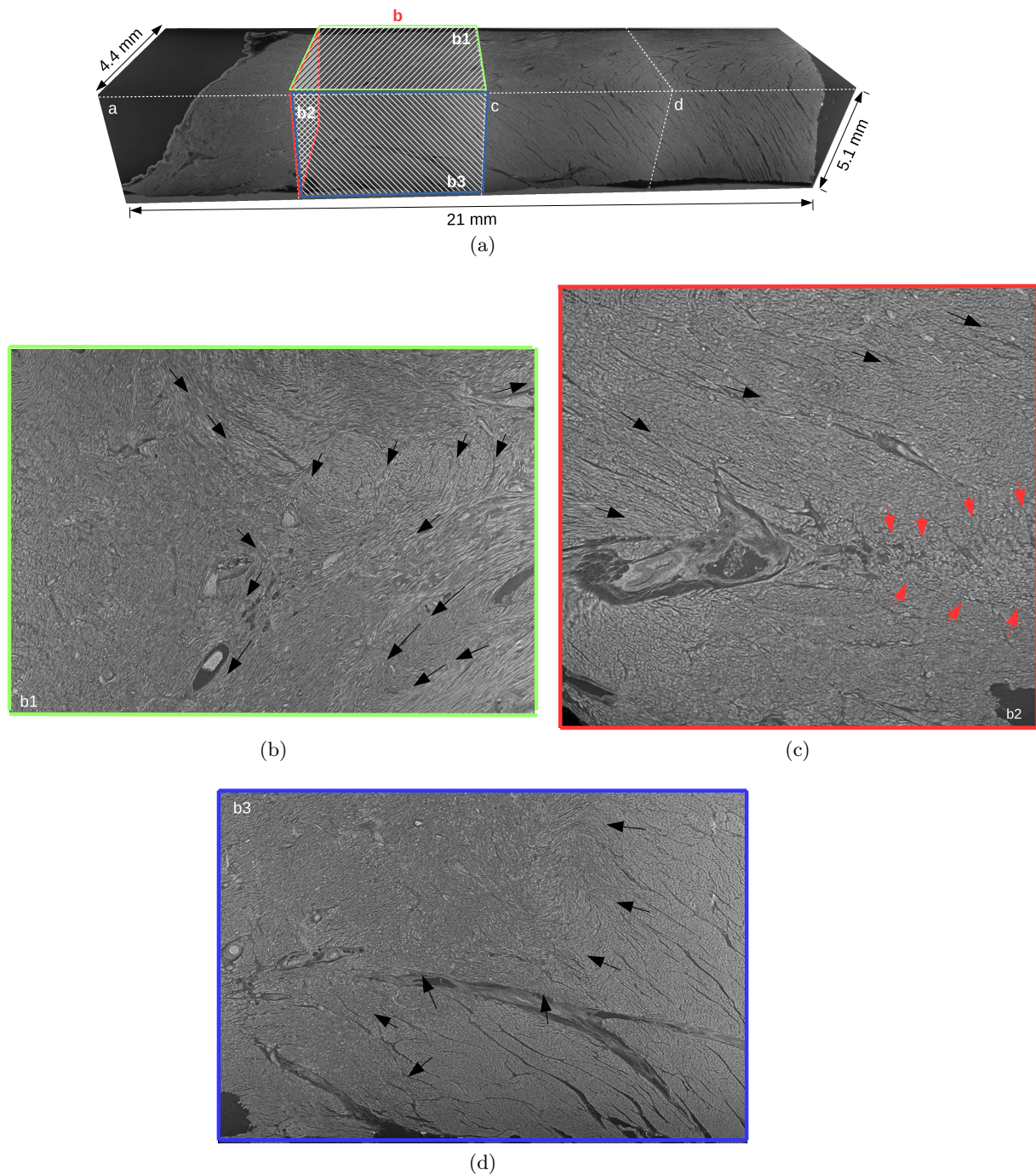


Figure 2.13: *a) Zoom-in on the top face of subsample (b) of the posterior septum sample from Figure 2.8. As opposed to subsamples (c) and (d), we can now see abrupt changes in the orientation of myocytes (black arrows mark the changes). b) Zoom-in on the left face of subsample (b) of the posterior septum sample from Figure 2.8. Myocytes keep their orientations (black arrows). The cleavages planes are thin. The myocytes (red arrows) change their orientation in the neighborhood of the transversally-cut cleavage plane, in which several blood vessels and adipose cells can be seen. Zoom-in on the front face of subsample (b) of the posterior septum sample from Figure 2.8. This section shows two organisation patterns, one corresponding to the region 1 and the other to the region 2. The approximate separation between patterns is indicated by the black arrows.*

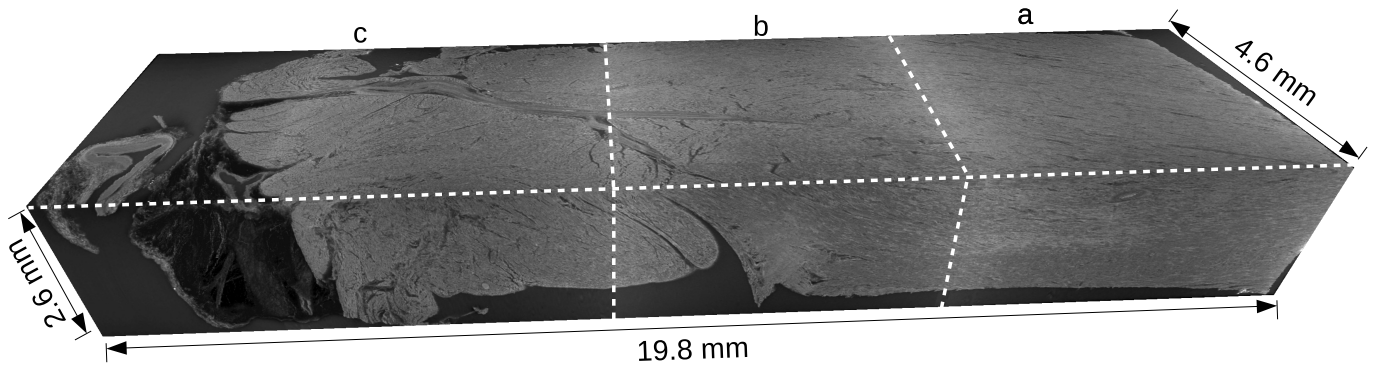


Figure 2.14: *Anterior septum image ($S_{ant_S1_2}$) obtained using 3D X-ray Phase Contrast μ -CT.*

endocardium to epicardium, until they reach the other pattern. In the other pattern, the cleavage planes are not so pronounced (much thinner) and the myocytes are arranged more compactly. The transition between the two patterns is abrupt, as can be seen in the attached images.

2.8.2 Cardiac microarchitecture of the anterior septum (sample 7)

A 3D transmural section from the anterior septum is presented in Figure 2.14. Most of the layers of perimysial extracellular matrix (cleavage planes) are very fine and can barely be seen, with the myocytes tightly packed. Unlike the sample from the posterior septum, the tissue seems to have only one organisation pattern. The myocytes and the cleavage planes change their direction very smoothly. The transmural sample will be split in blocks to better present the cardiac structure.

The first block (Figure 2.15 and Figure 2.15c) has myocytes and cleavage planes oriented in the same direction (Figure 2.15c). The structure is compact, with very dense myocytes and the few cleavage planes that can be seen are very thin (Figure 2.15d). Some areas exhibit wavy myocytes and collagen (Figure 2.15c).

In conclusion, the anterior and posterior septum are organised differently. The posterior septum shows two organisation patterns, the first being more fragmented, with many parallel and branching cleavage planes, while the second pattern resembles that of the anterior septum. The anterior septum shows a single pattern, with compactly-arranged myocytes and few cleavage planes. In the compact patterns, both the anterior and the posterior septum exhibit areas where the myocyte orientations change abruptly.

2.8.3 Cardiac microarchitecture of the posterior left ventricle (sample 6)

As can be seen in the Figure 2.17, the cleavage planes are parallel, their orientation varies smoothly and they are slightly curved. Advancing into the sample in the x direction, we start to see cleavage planes of other orientations, as can be seen in Figure 2.17b. Two populations of orthogonal cleavage planes can be seen in Figure 2.17b.

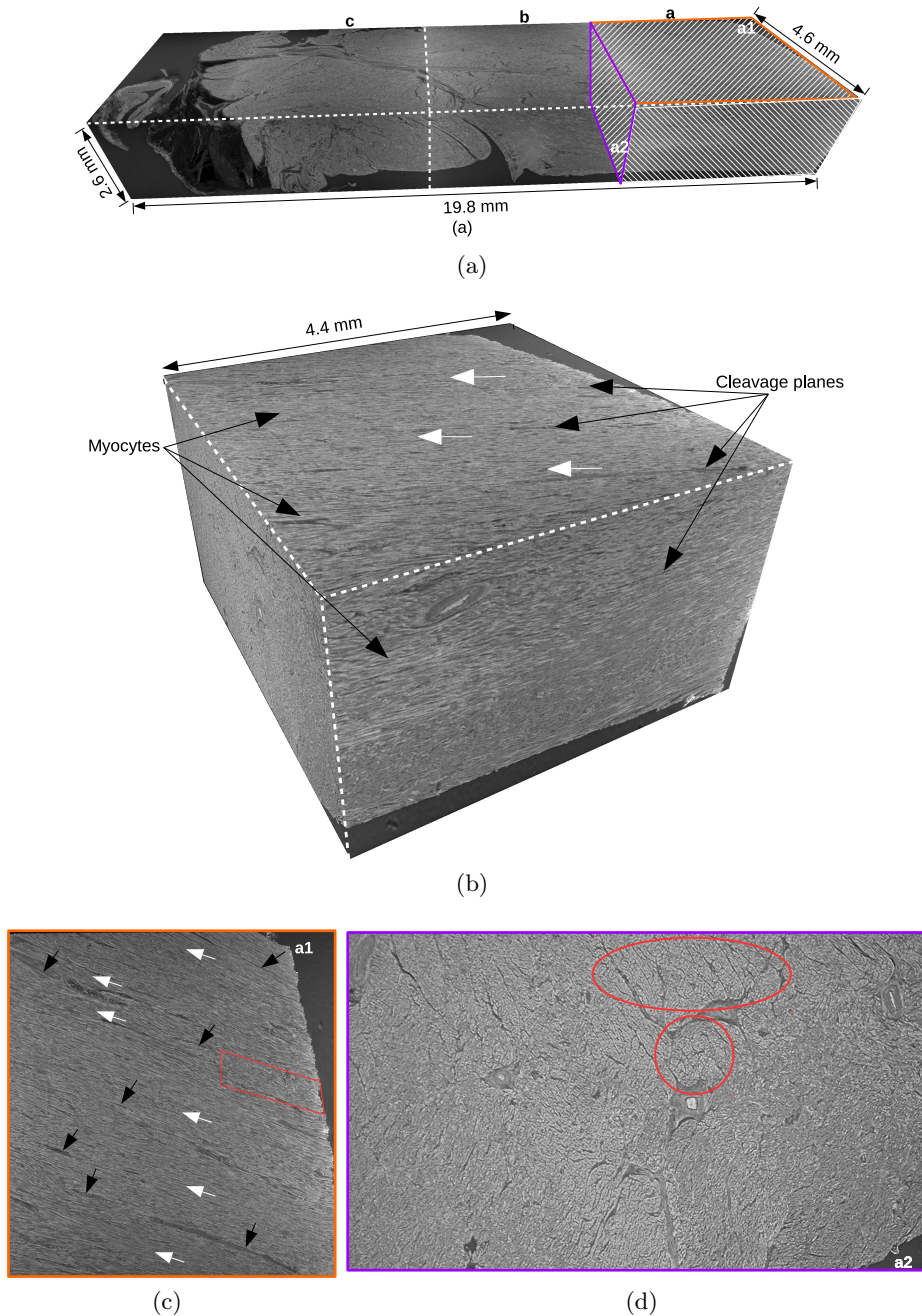


Figure 2.15: Zoom-in on the cube marked (a) of the anterior septum sample shown in Figure 2.14. The cleavage planes (dark grey) and myocytes (light grey) have the same direction (white arrows). Zoom-in on the top and left faces of the anterior septum sample from Figure 2.15. (a1): The black arrows show examples of thin cleavage planes; the white arrows show the direction of the cleavage planes and myocytes; the red polygon shows wavy myocytes and collagen. (a2): The myocytes appear mostly in transverse section; we can observe groups of myocytes surrounded by cleavage planes (red ellipses).

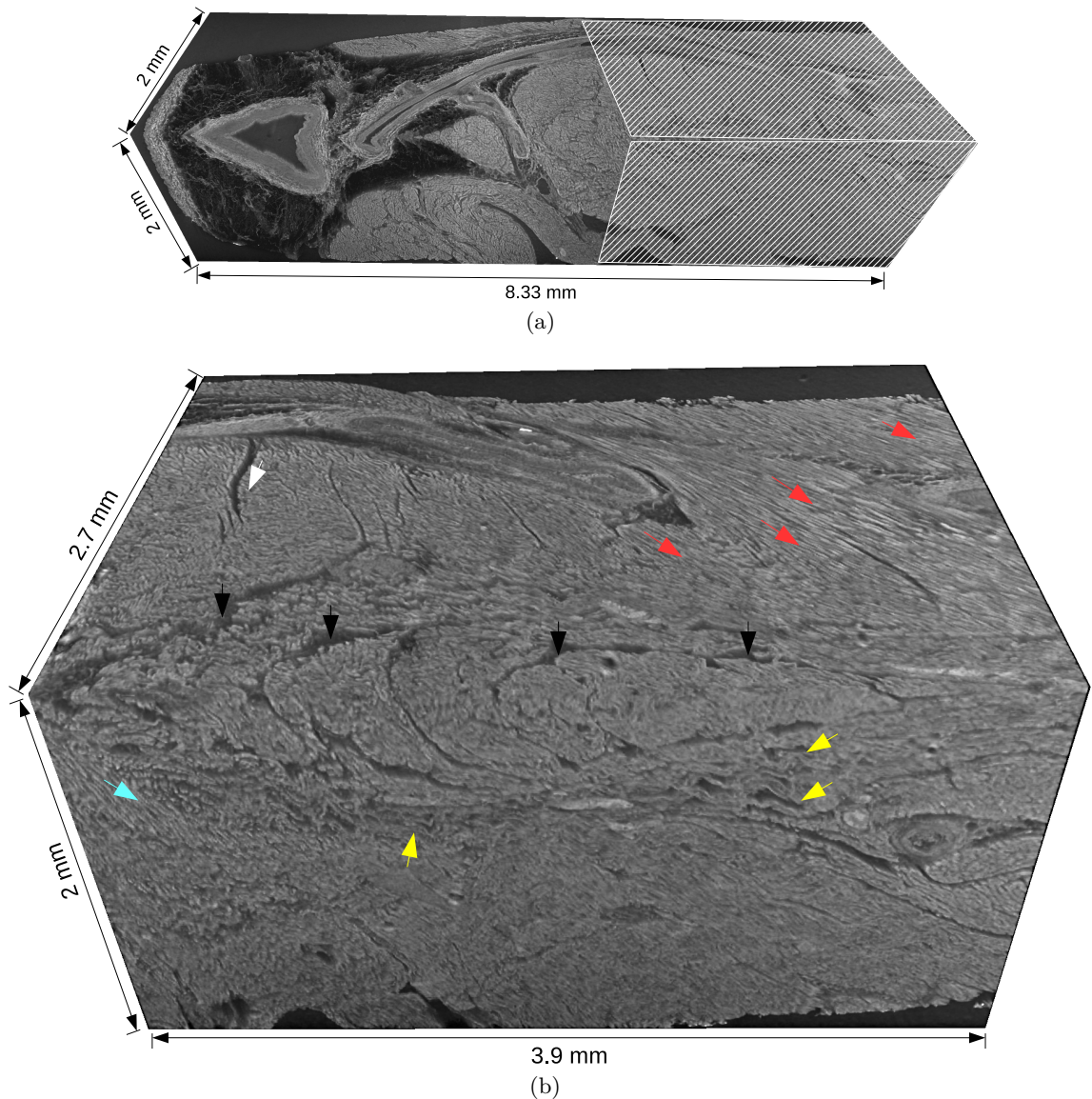


Figure 2.16: Zoom-in on part (c) of the anterior septum sample from Figure 2.14. Figure 2.16b: a zoom on the hatched section. On the top face, close to the artery, we see myocytes in longitudinal (red arrows) and in transverse section (white arrow); The black arrows show parallel cleavage planes surrounding groups of myocytes. On the front face, yellow arrows point to wavy myocytes. The light blue arrow (on the left side) shows myocytes switching direction from transversal to longitudinal section.

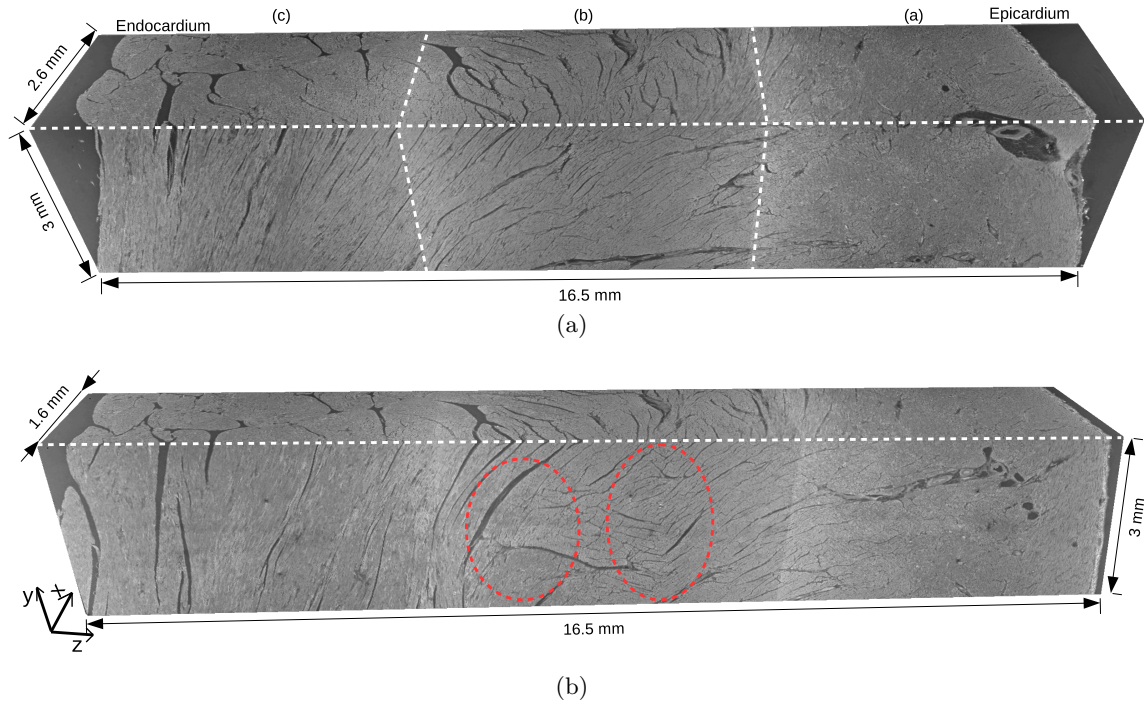


Figure 2.17: *Raw image of a posterior left ventricle sample (LV_post_S1_2) imaged using 3D X-ray Phase Contrast μ -CT. Figure 2.17a: a wider 3D crop (2,6 mm thick); Figure 2.17b: a narrower 3D crop (1,6 mm thick); We can observe two orthogonal populations of CP in the midwall of the sample.*

Close to the epicardium (Figure 2.18b), the myocytes are very dense and the perimysium extracellular matrix is very thin, with only small, hard to see cleavage planes. The orientation varies smoothly. We can see zones where the perimysium surrounds groups of myocytes.

The middle of the sample (Figure 2.19b) is more fragmented by the perimysium extracellular matrix. The cleavage planes are dense and generally parallel, but we can also see ramifications and zones where the myocytes suddenly change in orientation. We can see many areas where the perimysium surrounds groups of myocytes.

The papillary muscle is presented in Figure 2.20. The fragmentation pattern is different, with fewer thick CPs compared to the middle of the sample Figure 2.19. Also, can be seen zones where the myocytes suddenly change orientation.

2.9 Conclusion

The recent developments in μ -CT allow us to use the technique as a novel 3D imaging tool at a high resolution, to be able to visualise the cardiac tissue. The purpose is to allow a real 3D quantification of cardiac structures. Before we quantify the cardiac structure we present three samples to visualise the 3D cardiac structure, to be able to extract characteristics of the cardiac structures, especially cleavage planes, in order to be able to

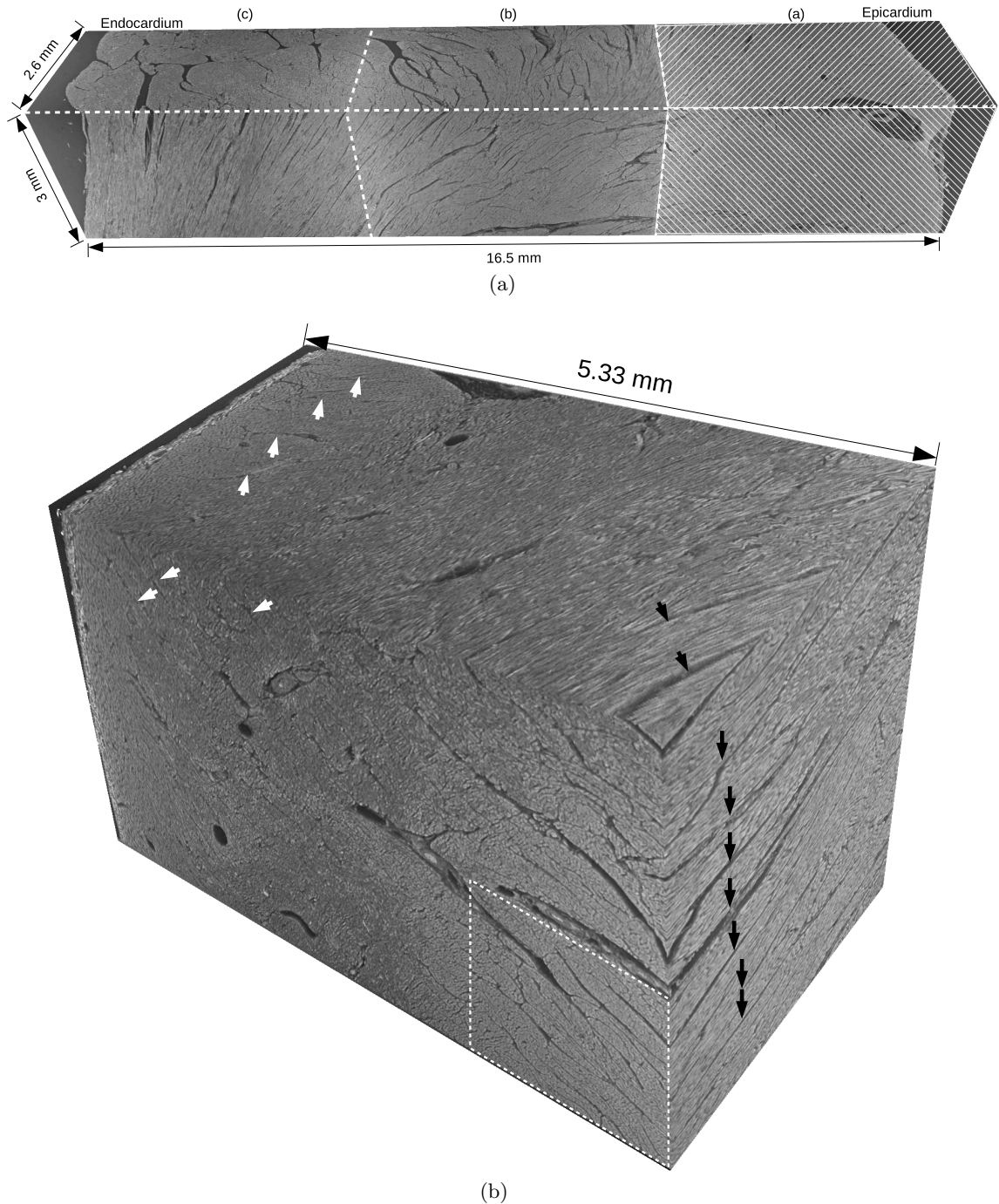


Figure 2.18: Zoom-in on the rightmost cube (marked (a)) of the posterior left ventricle sample shown in Figure 2.17a. Thick, parallel CPs can be seen in the more fragmented part (black arrows), as well as much smaller CPs in the more compact tissue part (white arrows). In 3D, the CP ramifications form closed myocyte "bundles" (white rectangle).

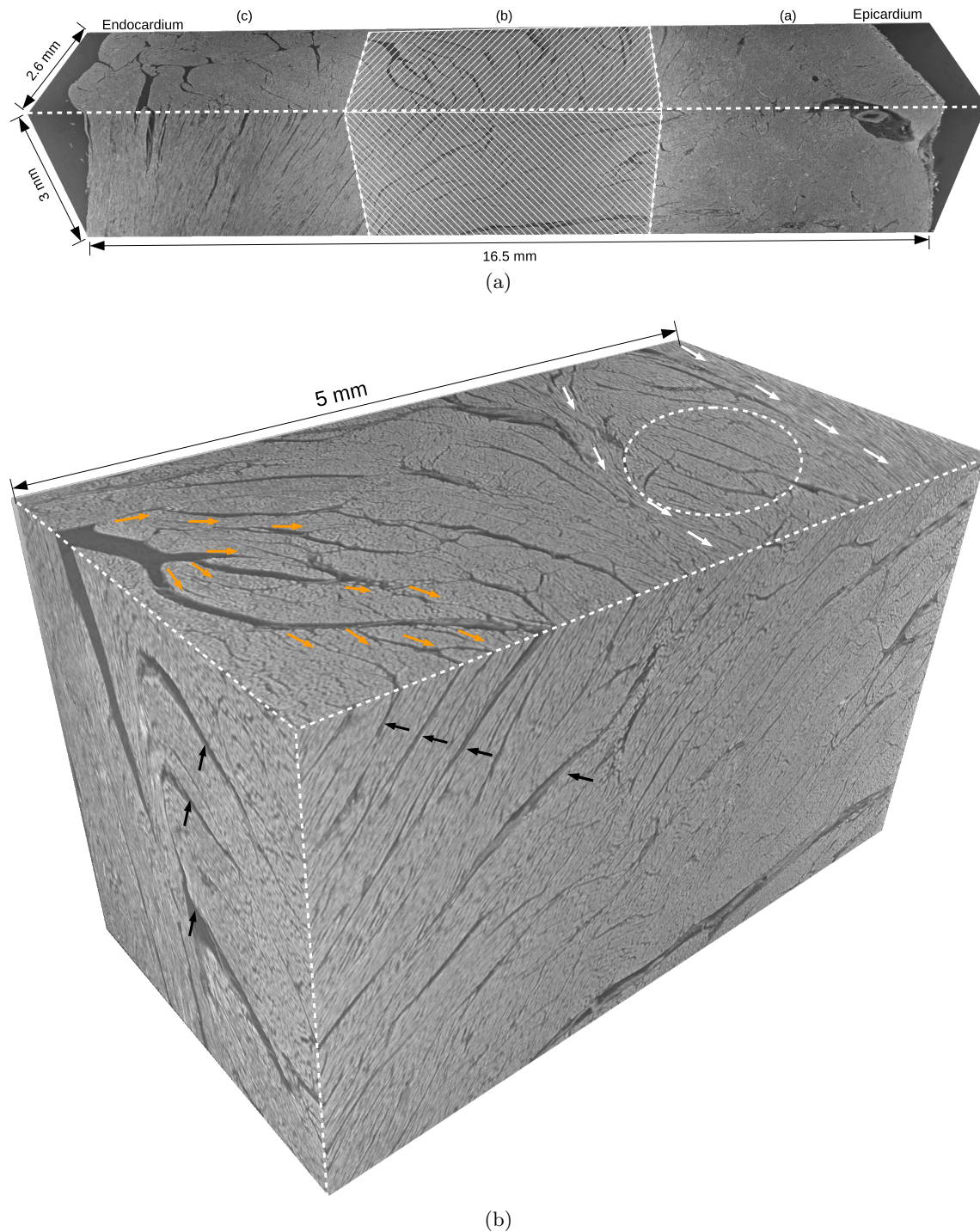


Figure 2.19: Zoom-in on the middle cube (marked (b)) of the posterior left ventricle sample shown in Figure 2.17a. Large, parallel CPs can be seen (black arrows). In 3D, the CP ramifications form closed myocyte "bundles" (orange arrows and white circle). The white arrows show an area where the myocyte orientation is very different from the surroundings.

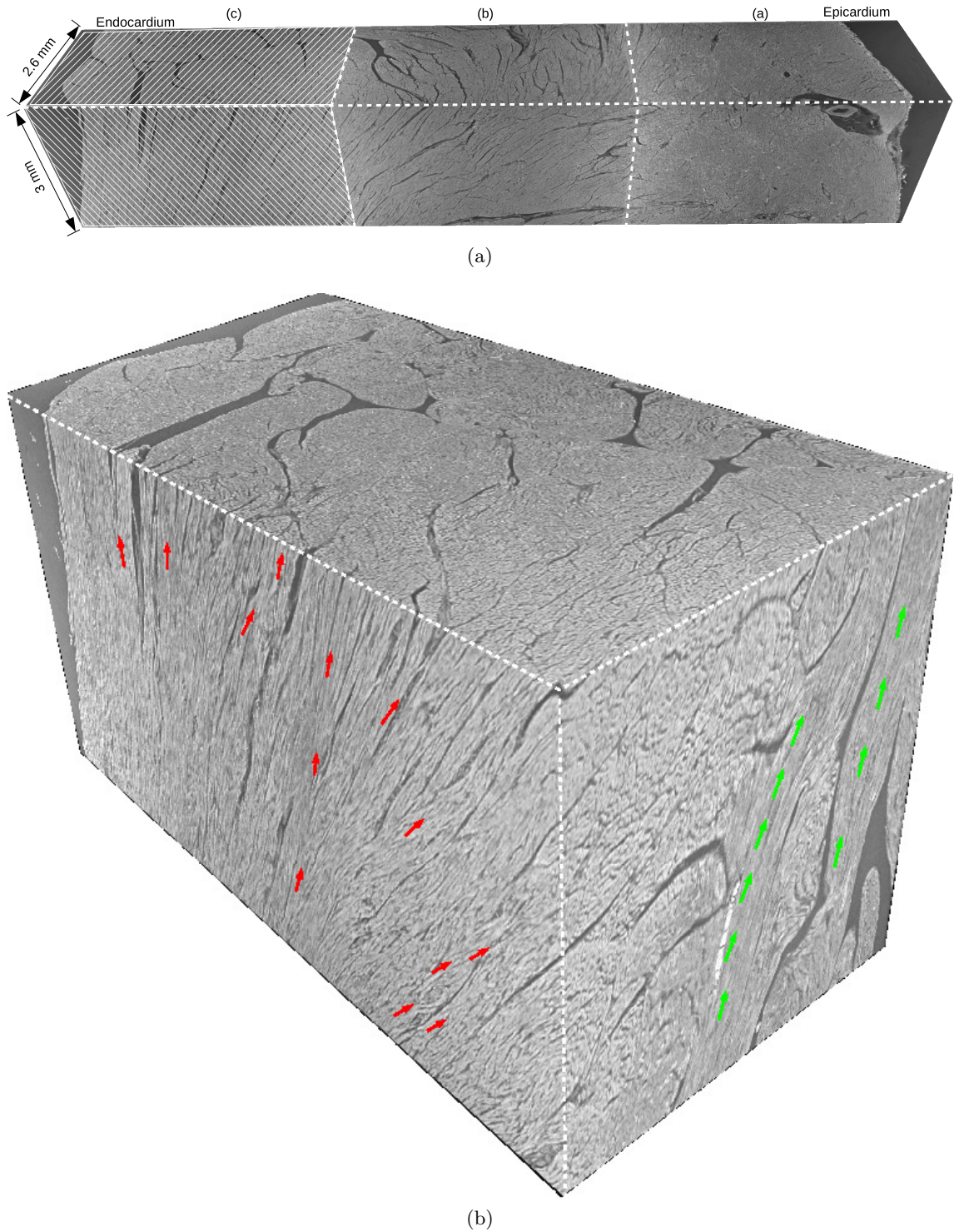


Figure 2.20: Zoom-in on the leftmost cube (marked (c), closest to the endocardium) of the posterior left ventricle sample shown in Figure 2.17a. We can again see wide cleavage planes, but the fragmentation pattern is different, with fewer thick CPs compared to Figure 2.19b. Red and green arrows mark the local myocyte orientations. It is interesting how around the green arrows, the myocytes are oriented in longitudinal section, only to switch to a transverse section in the immediate vicinity.

propose a quantification method based on image processing.

First, we compared some Phase Contrast μ -CT image samples with histology, in order to understand the new imagery technique. We have shown that X-ray phase contrast images are a viable tool for examining the microstructure of the heart. They can show the same structures as those seen in histological sections, without having to carefully prepare a set of slices. The greatest advantage of X-ray phase contrast images is the ability to capture 3D structures, from which much more information can be extracted, either through visual inspection by a human expert or through analysis with automatic algorithms.

Second, we presented for the first time, transmural 3D cardiac samples from the anterior septum, the posterior septum and the posterior left ventricle, at a very high resolution of $3.5\mu m$. All three samples are very different in texture and in the cleavage plane organization. We saw that the anterior septum contains only one, compact type of tissue organization pattern, without prominent cleavage planes, while the posterior septum shows two types of textures (one compact corresponding to the right ventricle and the other more fragmented corresponding to the left ventricle) and a separating zone between the two patterns. The cleavage planes are very well seen in the posterior septum and in the posterior left ventricle. Also, the presence of cleavage planes that surround groups of myocytes was observed.

In all the samples the cleavage planes are most of the time parallel and smoothly change their direction. However, in some areas, sudden changes in the orientation of neighbouring groups of myocytes were observed, corresponding to tissue volumes that contract in almost orthogonal directions. There are also large zones where the cleavage planes are branching and merging. We have also confirmed the existence of two quasi-orthogonal populations of cleavage planes in certain regions of the left ventricle (previously reported in the literature), whose role in the cardiac motion biomechanics is certainly important.

The cardiac structure revealed by the three samples presented is highly complex, and a simple visualisation is not enough to characterise the structure. An image processing treatment and a statistical approach is required to analyse the structure and extract quantitative information. The next step is to develop such an algorithm to extract the cleavage planes and to characterize their thicknesses and the inter cleavage plane distances.

Image processing and analysis Traitement d'image et analyse

3.1 Introduction

A good knowledge of the cardiac microarchitecture is essential for understanding the myocardial mechanics and electrical activity of human hearts, as well as the relations between mechanical function, hemodynamics and the adaptive structural changes in cardiac diseases [Weber *et al.* (1994)], [Kanzaki *et al.* (2012)b]. For this reason, detailed information about the organization and the spatial relationship between cardiac elements is required. However, our understanding of the cardiac architecture is limited by the lack of 3D descriptions of the cardiac organization at a small or microscopic scale as was presented in Chapter 2.

One of the main components that define the 3D myocardial tissue organization and function is the cardiac extracellular matrix. The cardiac extracellular matrix includes: endomysium that surrounds and separates individual myocytes and capillaries, perimysium that surrounds and separates groups of myocytes and epimysium that surrounds the entire heart muscle.

In this chapter, we develop a method to quantitatively investigate the transmural 3D microstructure of the left ventricle of the human heart, using very high resolution X-ray phase contrast micro-tomography 3D images presented in Chapter 2. An image processing protocol is developed to automatically extract cleavage planes and compute statistics of their thickness and distance separating them.

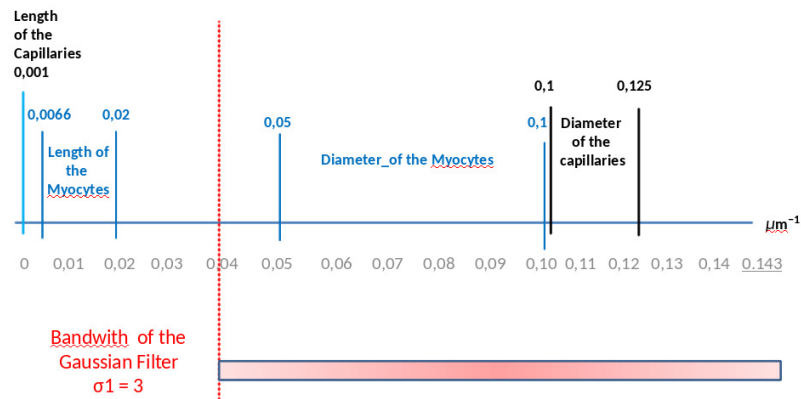
This chapter is structured as follows: First, we explain the necessity of a good knowledge of the cardiac microarchitecture. Then, a spatial and frequency description of the cardiac components is presented in section 3.2. The multi scale processing is described in section 3.3 and the extraction of statistics about cleavage plane thicknesses and inter cleavage plane distances is described in section 3.4. The methodology evaluation is presented in section 3.5. Finally, the conclusion is presented in section 3.6.

3.1.1 Cardiac extracellular matrix

The cardiac extracellular connective tissue network plays a major role in the structure organisation and reflects the hierarchy of myocyte architecture. Each myocyte and capillary is tethered with endomysium collagen cords and groups of myocytes are separated by perimysium laminar structures ("planes"). The collagen can be seen like a honeycomb that imposes the myocardial structure organisation. The 3D arrangement of the cardiac connective network is essential for understanding the myocardial mechanics and electrical activity of the human heart, and the relations between mechanical function, hemodynamics and the adaptive structural changes in cardiac diseases. As the myocardium is an elastic network of myocytes held together by the connective tissue matrix, the elastic properties of the connective tissue matrix dictate the mechanical function of myocardium. [Hanley *et al.* (1999)] tested the cardiac muscle stretching properties and the conclusion of their studies was that the collagen network imposes the stretching and the extension limits of the cardiac myocyte. After the myocyte stretching process they observed that the connective tissue network was rearranged to align more closely with the myocytes direction. [Caulfield and Borg (1979)] saw the perimysial network as organising individual myocytes into a functional unit and providing a framework for distributing the contractile force within the ventricular wall. Also, [LeGrice *et al.* (2005)] argue the idea that « the connective tissue matrix stores the energy during the systole and also contributes to the elastic recoil of the ventricles during rapid filling».

Robinson and his co-workers [Robinson *et al.* (1983)] proposed specific mechanical roles for the cardiac connective tissue matrix based on their anatomical observations. It is most probable that each of the components of the connective tissue hierarchy contributes to the mechanical properties of passive myocardium. Robinson and colleagues argued that the epimysium protects sarcomeres from being overstretched [Robinson *et al.* (1983)].

For this reason, detailed information about the organisation and the spatial relationship between the cardiac tissue components is required. Our aim is to identify and separate the various components of the tissue according to their specific size and shape. In this chapter we present the second contribution of this thesis: we develop a novel method to access the 3D arrangement of those micro-structures and provide a quantitative analysis of the three-dimensional extracellular matrix spatial organisation [Mirea *et al.* (2016)].

Figure 3.1: *Spatial frequency of the components.*

3.2 Spatial and frequency description of the tissue components

Let us first analyse the relationships between the shape and size of the components we want to detect within the cardiac tissue and their related spatial frequencies.

3.2.1 Myocytes

The myocytes have an elongated shape which size varies according to their location within the cardiac tissue. If we consider the range of the myocyte diameters between $10 \mu\text{m}$ and $20 \mu\text{m}$ ([Streeter (1979)], [Gerdes *et al.* (1986)], [Sato *et al.* (1996)], [Spach *et al.* (2004)], [Kocica *et al.* (2006)]), then the corresponding spatial frequencies will range between $0,1 \mu\text{m}^{-1}$ and $0,05 \mu\text{m}^{-1}$ respectively. The myocytes are stacked in small groups (5 to 6) within the tissue. The thickness of a stack can range roughly from $50 \mu\text{m}$ to $120 \mu\text{m}$. Each stack is packed in perimysium. Similarly, if we consider the range of the myocytes length between $50 \mu\text{m}$ and $150 \mu\text{m}$, then the corresponding spatial frequencies will range between $0,02 \mu\text{m}^{-1}$ and $0,0066 \mu\text{m}^{-1}$ respectively.

3.2.2 Capillaries

The tissue is perfused by capillaries with a diameter between $8 \mu\text{m}$ and $10 \mu\text{m}$. Their diameter is identical or a bit smaller than that of the myocytes. Their related spatial frequencies will range from $0,125 \mu\text{m}^{-1}$ to $0,1 \mu\text{m}^{-1}$ respectively. The length of the capillaries is about 1 mm to 2 mm [Robert and Freitas (2004)], so their frequency contribution will be very low: from $0,001 \mu\text{m}^{-1}$ to $0,0005 \mu\text{m}^{-1}$. The myocytes and the capillaries are embedded within the extracellular collagen matrix denoted endomysium. The cleavage planes belong to this extracellular matrix. The spatial component frequencies are represented in Figure 3.1

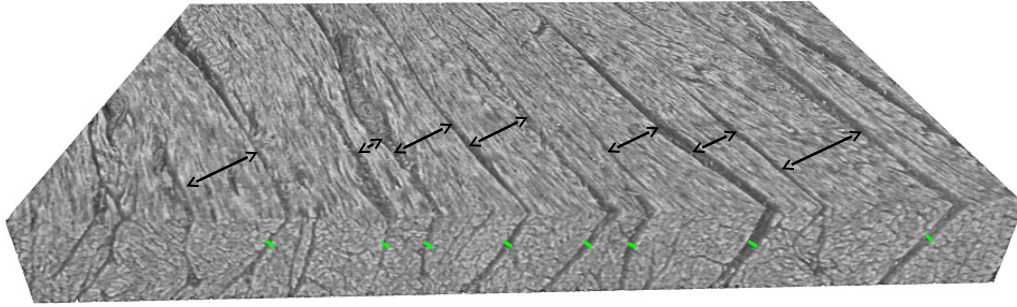


Figure 3.2: *Illustration of the extracellular collagen network in an anterior LV tissue sample. The cleavage planes (CP) (planar dark grey vertical planes) separate the groups of myocytes. The black arrows represent the distance separating the CP and the green segments show their thickness.*

3.2.3 Data sampling and frequency content

The spatial resolution available in the reconstructed data has practical consequences on the detection of the various components. If e_n is the edge of each reconstructed voxel, for $n \in \{1, \dots, N\}$, where N stands for the spatial dimension ($N=3$ for a volume), then the highest frequency f_n^{\max} correctly detected in the data spectrum, in each dimension, is given by :

$$f_n^{\max} = \frac{1}{2 \cdot e_n} \quad (3.1)$$

In our reconstructed 3D data, each voxel is isotropic, with an edge $e_n = 3.5 \mu\text{m}$ so the maximum frequency available in the data, in each spatial direction, will be $f_n^{\max} = \frac{1}{2 \cdot 3.5} = 0.143 \mu\text{m}^{-1}$.

3.3 Multiscale processing

We propose an image processing protocol to automatically extract cleavage planes and compute statistics on their individual thickness and distance separating them two by two. The distances and the thicknesses that we want to determine are illustrated in Figure 3.2. The method relies on the fact that the cleavage planes are locally parallel and have a privileged direction.

The first aim is to automatically extract the cleavage planes by processing the 3D data. As presented in Chapter 2, the cleavage planes correspond to the extracellular matrix called perimysium. We must take into consideration the huge size of each reconstructed tissue sample (80 GB), considered as the raw data, and the total amount of raw data (~ 600 GB) to process. The size and computation time are important limiting factors that justify a multiscale approach and the use of a simple segmentation method. Each reconstructed tissue sample is divided into contiguous sub-volumes processed separately. To be able to extract the cleavage planes (CP), we use a multiscale Gaussian pyramid approach. We

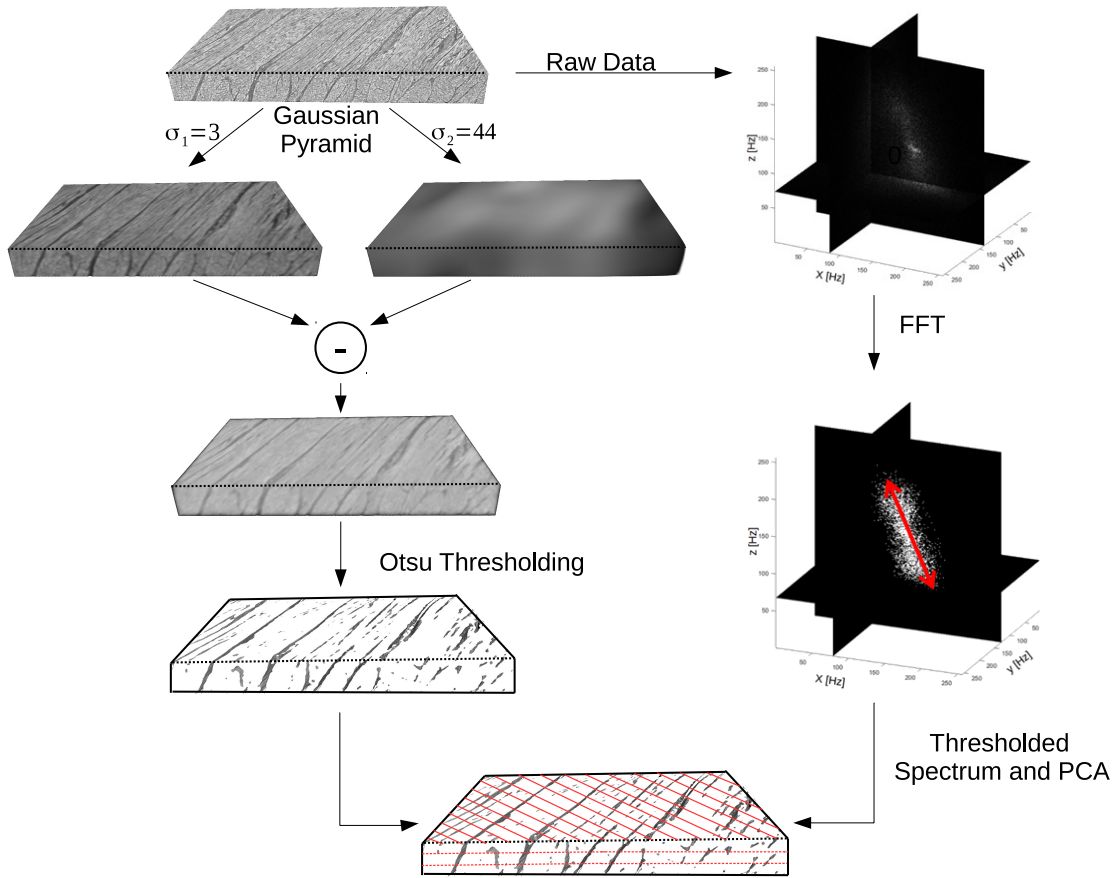


Figure 3.3: *Processing steps for extracting cleavage planes (CP) thickness and inter-CP distance. Left side, a Difference of Gaussians serves to filter noise and select the CP, followed by thresholding. Right side, a Fast Fourier Transform (FFT) is applied on the raw sub-volume, followed by thresholding and Principal Component Analysis (PCA). The orientation, perpendicular to the CP is extracted.*

first suppress noise and thin structures as endomysium, and preserve larger structures corresponding to cleavage planes. Then we perform a binarisation operation. We apply a global 3D thresholding using the Otsu method [Otsu (1979)] on each pre-processed sub-volume to binarise the data and select the CP only. Independently of these steps we compute the FFT of each raw sub-volume, binarise the spectrum and use a PCA method to extract the main orientation of the tissue components. We then build a grid of lines, perpendicularly to the main orientation, that crosses the CP to calculate statistics related to their thicknesses and inter CP distances. The entire process is illustrated in Figure 3.3 and described in detail in the following.

3.3.1 Pre-processing with the Gaussian pyramid

We know, the length of a myocyte lies within the range 50 - 150 μm and its diameter within the range 10 - 20 μm . The myocytes are stacked in small groups (5 to 6) within the tissue. The tissue is perfused by capillaries whose length is between 1 mm - 2 mm and the

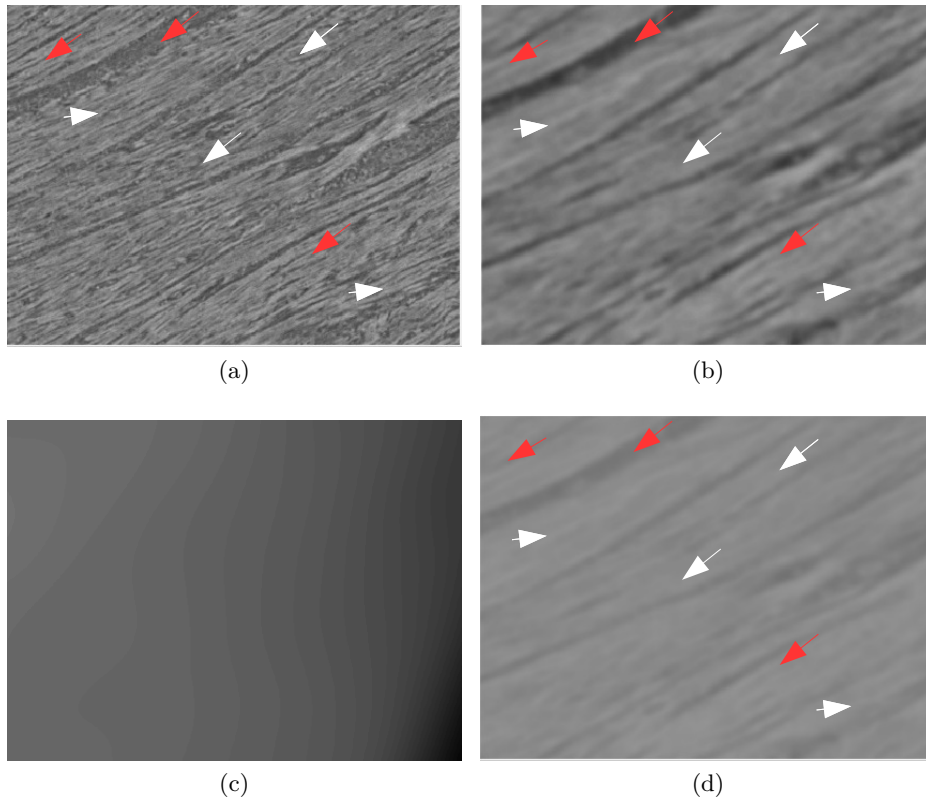


Figure 3.4: (a) Raw Image; (b) image (a) filtered by the Gaussian filter level $\sigma_1 = 3$. Note the blurring effect on the endomysium (small gaps separating individual myocytes) (white arrows) all the while preserving cleavage planes (red arrows); (c) image (a) filtered by the Gaussian filter level $\sigma_2 = 44$. Only very slow variations are preserved; (d) Resulting filtered image of Gaussians output (b)-(c).

diameter between 8 - 10 μm . The myocytes and the capillaries are embedded within the extracellular collagen matrix denoted *endomysium*. Our aim is to identify and separate the various components of the tissue according to their specific size and shape.

We now focus on the extraction of the cleavage planes. To do so, we compute the Gaussian pyramid of the sub-volume, from which we retain the two following levels: the level $\sigma_1 = 3$ that aims to filter data with an isotropic Gaussian filter of size 13 x 13 x 13 voxels and the level $\sigma_2 = 44$ that aims to filter data with an isotropic Gaussian filter of size 177 x 177 x 177 voxels.

The smoothing effect of level $\sigma_1 = 3$ is low: it blurs small-scale structures such as the endomysium (Figure 3.4 (b)) and suppresses high frequency noise. On the contrary, the smoothing effect of level $\sigma_2 = 44$ is very strong: it preserves only the very low frequency components of the background which generally correspond to an image acquisition artifact (like vignetting) (Figure 3.4 (c)). We then compute the difference between these two levels of the pyramid in order to select the structures of interest while eliminating the noise and background. The results are shown in Figure 3.4 and Figure 3.5.

To illustrate the processing steps, we select 256 voxels of the sub-volume lying along a

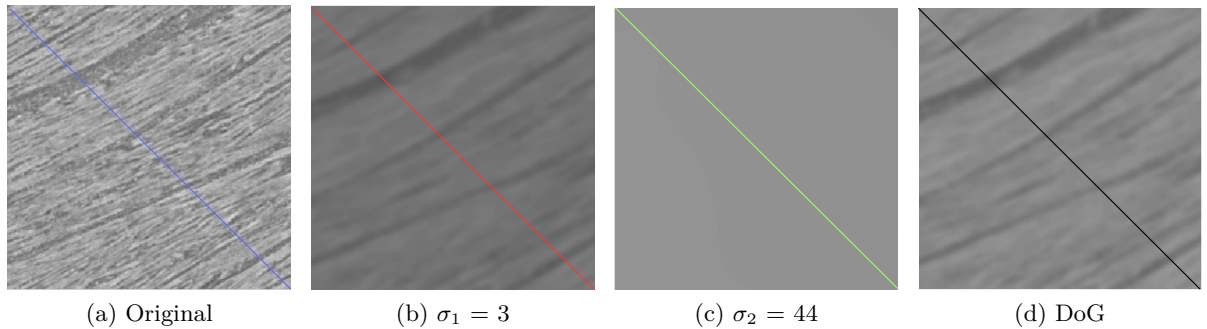


Figure 3.5: *Result of filtering operations on an image: (a) shows the original image; (b) shows the result of filtering with a Gaussian filter width $\sigma_1 = 3$ whose effect is to blur small structures; (c) is the result of filtering with $\sigma_2 = 44$ which only preserves the slowest variations; (d) is the Difference between the two Gaussians. The line represents pixels that we sample to illustrate the effects of filtering (see Figure 3.6 and Figure 3.7).*

line (the diagonal lines in Figure 3.5), perpendicular to the cleavage planes. We examine the properties of this line both in the spatial and frequency domains during the filtering process. In Figure 3.6a we see the original line profile (blue) in the spatial domain, corresponding to the intensity of the selected voxels. The rapid local intensity variations are due to the presence of the endomysium. The red profile obtained after filtering the data with Gaussian filter $\sigma_1 = 3$, shows much less pronounced amplitude variations in the endomysium but preserves the larger gaps corresponding to the presence of the cleavage planes. The green profile Figure 3.6a is the result of filtering the data with the Gaussian filter $\sigma_2 = 44$. If we compute the difference between the two filtered profiles (DoG), we obtain the black profile shown in Figure 3.6a. The cleavage planes are enhanced (red arrows) and now easy to detect Figure 3.4.

Let us now examine what happens in the frequency domain. The module of the FFT of each line profile displayed in Figure 3.6a is shown in Figure 3.6b. Figure 3.6d represents a zoom of Figure 3.6b. We show the spectrum of the profile of the original diagonal line (see Figure 3.5a) (blue), as well as the FFT of the two Gaussian filters, Figure 3.6c, of the selected levels of the pyramid $\sigma_1 = 3$ in red and $\sigma_2 = 44$ in green.

The profile of the original diagonal line contains 256 voxels. Its Fourier transform will therefore contain 256 frequency points. Because of the symmetry, only 128 points will cover the whole spectrum. The sampling step of the Fourier spectrum thus corresponds to $X_f = \frac{f_n^{\max}}{128}$. Knowing the maximum frequency contained in the data, it comes that the sampling step equals: $X_f = \frac{0.143\mu m^{-1}}{128} = 0.0011 \mu m^{-1}$.

The spectrum of the Gaussian filter with $\sigma_1 = 3$ has negligible amplitude beyond the frequency point 36 (Figure 3.6c, red), corresponding to a spatial frequency equal to $0.04 \mu m^{-1}$ which explains why the DoG spectrum no longer contains energy beyond this frequency (Figure 3.6d, black). This value corresponds to a structure of a size $X_f = \frac{1}{2 \times 0.04} = 12.4 \mu m$. This matches well with the range of myocytes diameters, between $10 \mu m$ and $20 \mu m$, and explains why the chosen filters are well suited for blurring myocytes

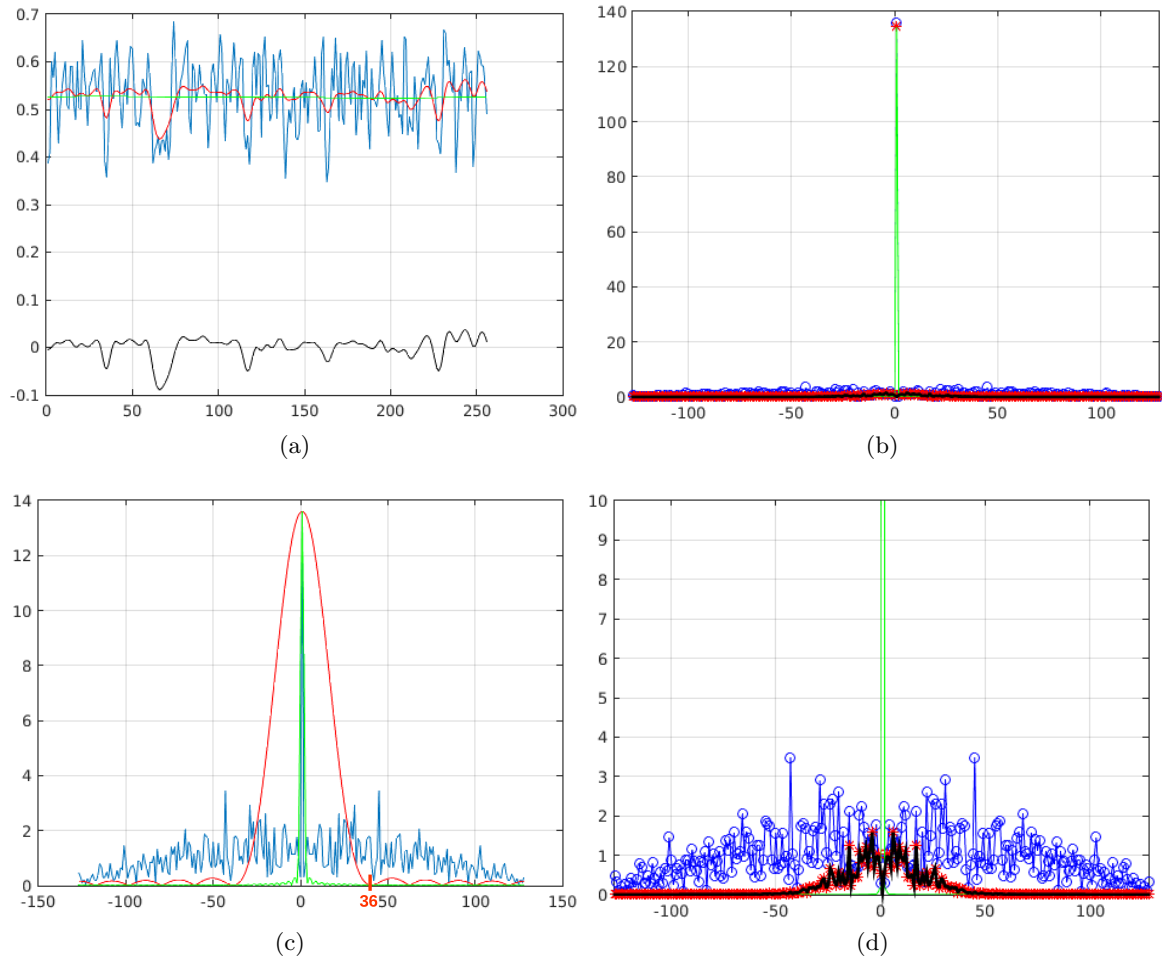


Figure 3.6: *Effect of the filtering process, displayed along a line perpendicular to the cleavage planes (diagonals in 3.5). (a) original profile (blue), superimposed to the profiles filtered with Gaussian filters $\sigma_1 = 3$ (red), $\sigma_2 = 44$ (green), and the resulting profile (DoG) (black). We see how the rapid variations have been reduced, while the larger gaps are preserved. (b) FFT of the diagonal presented in (a), and a zoom of (b) is presented in (d). (c) Spectrum of the original (blue), superimposed to the spectrum of the Gaussian filters $\sigma_1 = 3$ (red) and $\sigma_1 = 44$ (green).*

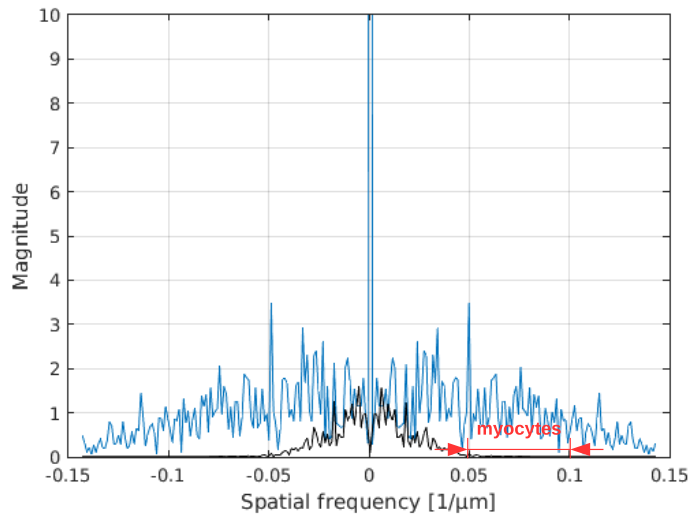


Figure 3.7: *Spectrum of the original profile (blue), displayed in Figure 3.5a, superimposed to the resulting profile (DoG) (black). The attenuation of the high-frequency components (over $0.05 \mu\text{m}^{-1}$) as well as the suppression of very low frequency components is clearly visible.*

and endomysium.

Similarly, we note that the spectrum of the Gaussian filter with $\sigma_2 = 44$ has a very narrow shape centered on the zero frequency, which explains the suppression of the very low frequency components in the DoG resulting profile (Figure 3.6d, black).

We display (Figure 3.7) the spectrum of the result applying these filters, which corresponds to a multiplication in the frequency domain between the spectrum of the line and the spectrum of the filter. The spectrum of the resulting profile after the double filtering (DoG) (black) superimposed to the original profile (blue).

Let $V_{in}(x, y, z)$ be the 3D input image (sub-sample), $g_{\sigma}(x, y, z)$ a Gaussian filter of mean equal to zero and standard deviation σ and $V_{out}(x, y, z)$ the output image (filtered sub-volume). The Difference of Gaussians (DoG) is given by Equation 3.2 and the results can be seen in Figure 3.4.

$$V_{out}(x, y, z) = V_{in}(x, y, z) * g_{\sigma_1}(x, y, z) - V_{in}(x, y, z) * g_{\sigma_2}(x, y, z) \quad (3.2)$$

where $*$ denotes the convolution operator and

$$g_{\sigma}(x, y, z) = \frac{1}{2\pi\sigma^2} \cdot e^{-\frac{x^2 + y^2 + z^2}{2\sigma^2}} \quad (3.3)$$

is a 3D Gaussian convolution kernel.

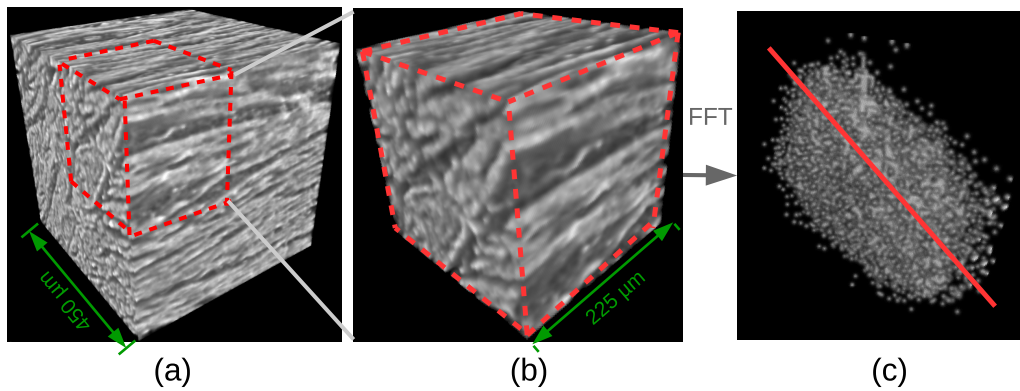


Figure 3.8: (a) Raw-image of a 3D cardiac tissue region with several parallel cleavage planes. The myocytes are shown in light grey, the endomysium and perimysium in dark grey. (b): Display of a 3D sub-region of (a) (red cube). (c): Thresholded 3D FFT spectrum of (b). We note the elongated shape of the spectrum in a direction orthogonal to the cleavage planes.

3.3.2 Extracting the cleavage planes orientation

Apart from the multiscale processing step, we also compute the preferential average orientation of the cleavage planes using a strategy based on the 3D Fast Fourier Transform (FFT). The approach is based on the following property: a discontinuity in the spatial domain (such as a cleavage plane) will introduce strong components in the frequency domain mainly in a direction *perpendicular* to the discontinuity. The amplitude of the spectral components introduced by the discontinuity and the cut off frequency depend on the exact shape and size of the discontinuity, but the tendency of spectral components to align themselves perpendicularly to the discontinuity will always be observed.

An ideal (perfectly straight) cleavage plane is discontinuous only along the direction orthogonal to the plane. Therefore, the cleavage plane will introduce spectral components in the FFT aligned with that direction: the method we propose consists in detecting this direction. An actual (not-so-ideal) example is shown in Figure 3.8 which exhibits a reconstructed tissue sample with several parallel cleavage planes. Its binarised 3D FFT spectrum (the thresholding operation is explained below) is shown on the right. Even though the tissue contains other micro-structures which also contribute to the global shape of the FFT, we can see that the *principal orientation* remains orthogonal to the cleavage planes.

Let us now consider the extracellular matrix. An ideal (perfectly straight, cylindrical) myocyte exhibits more discontinuity in the planes orthogonal to its long axis. Therefore, the spectral components of its FFT will belong to a plane orthogonal to the direction of its long axis. An actual (not-so-ideal) example is shown in Figure 3.9 which exhibits a reconstructed cardiac tissue sample with only myocytes separated by endomysium. The shape of its binarised 3D FFT spectrum resembles a flattened ellipsoid which main direction is orthogonal to the long axis of the myocytes. The FFT ellipsoid is thinner along

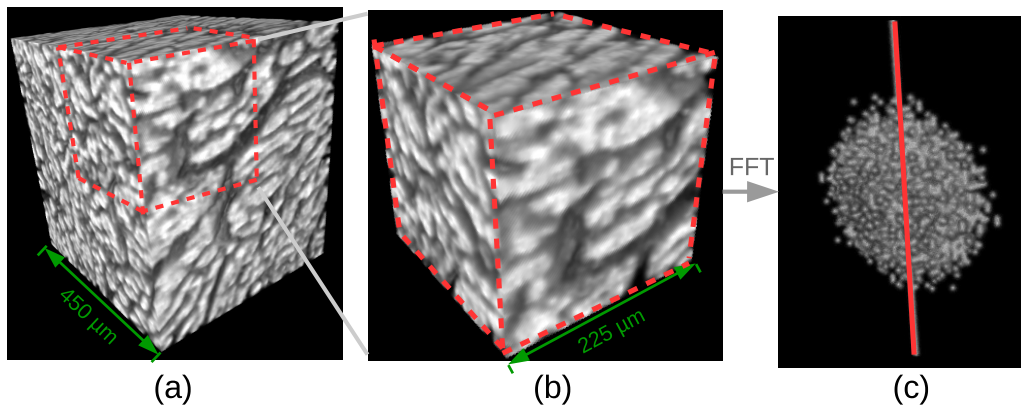


Figure 3.9: (a) Raw image of a 3D cardiac tissue region with myocytes and endomysium. The myocytes are shown in light grey and the endomysium in dark grey. (b) Display of a 3D sub-region of (a) (red-cube). (c) Thresholded 3D FFT spectrum of (b). The shape of the spectrum resembles a flattened ellipsoid orthogonal to the average myocyte direction (long axis).

the direction of the myocytes than in directions orthogonal to the myocytes.

In practice, an actual cardiac tissue sample is more complex than the two above examples and may contain myocytes and endomysium in various orientations, as well as cleavage planes. However, the cleavage planes remain locally parallel and the general distribution of the spectral components of higher amplitude remains orthogonal to the cleavage planes, as illustrated in Figure 3.10.

Because visualizing 3D structures on paper is quite challenging, we supplement the 3D figures with 2D slices taken through the corresponding sub-volumes (Figure 3.11).

These observations justify the following approach for extracting the main direction of the cleavage planes (the normal to the cleavage planes): we compute the 3D Fast Fourier Transform (FFT) of a cubic region of interest (256 x 256 x 256 voxels) extracted from a sub-volume of the original reconstructed volume. We threshold the FFT to keep only 25 % of the mean of the first lowest-frequency components that make up 85 % of the energy in the FFT spectrum. Because of the properties discussed previously, the spectral components above the threshold will have the tendency to be distributed in a direction orthogonal to the cleavage planes. Therefore, if we take the coordinates in the FFT domain of these spectral components.

We perform a Principal Component Analysis (PCA) of the 3D binarised Fourier spectrum as proposed in [Varray *et al.* (2013)], to recover the *principal direction* of these spectral components. The direction orthogonal to the cleavage planes is then selected.

Following is a short summary of how PCA works. PCA represents data (in our case, FFT voxel coordinates) in a new orthogonal coordinate system in which the axes (basis vectors) follow the modes of greatest variance in the data. The first axis of the new coordinate system is the one along which the data has the highest spread, in our case the main direction of the FFT components. The second axis, orthogonal to the previous one,

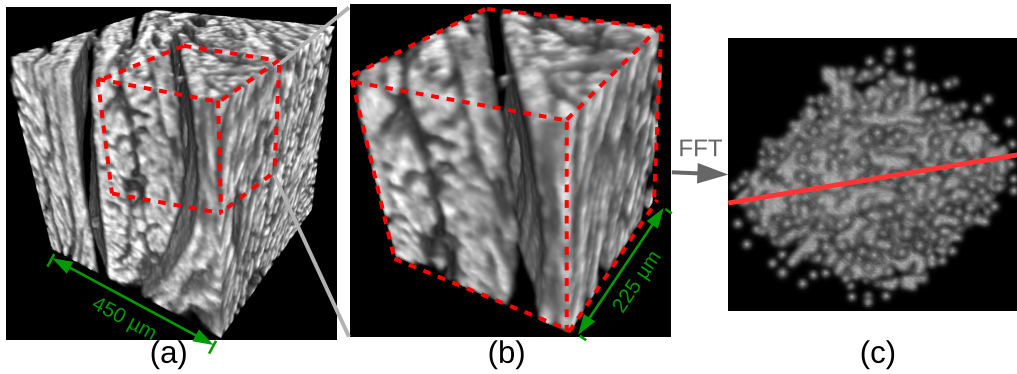


Figure 3.10: (a) Raw image of a 3D cardiac tissue region with myocytes, endomysium and cleavage planes. The myocytes are shown in light grey and the endomysium in dark grey. (b) Display of a 3D sub-region of (a) (red cube). This sub-region contains myocytes oriented horizontally (perpendicular to the page) on the left side of the cleavage plane and vertically on the right side of the cleavage plane. (c) Thresholded 3D FFT spectrum of the (b) The shape of the spectrum is more complex, but the principal direction remains that of the cleavage plane.

is the axis of the second greatest variation and so on.

The PCA method is based on the computation of the eigenvalues and their corresponding eigenvectors of the covariance matrix of the data (voxel coordinates x_i in our case):

$$C_x = \frac{1}{M} \sum_{i=1}^M (x_i - m)(x_i - m)^T \quad (3.4)$$

where $x_i = [x_1, x_2, x_3]^T$, is an FFT voxel coordinate in three dimensions, M is the total number of voxels considered (spectral components above the amplitude threshold) and m is the average coordinate of all FFT voxels above the threshold:

$$m = \frac{1}{M} \sum_{i=1}^M ([x_1 \ x_2 \ x_3]_i^T) \quad (3.5)$$

The first eigenvector (corresponding to the largest eigenvalue) gives the direction of the axis of greatest variation in the data, therefore the direction along which FFT components are spread out, therefore the direction perpendicular to cleavage planes.

3.3.3 Binarisation step

The next processing step is a binarisation operation. We apply a 3D Otsu thresholding [Otsu (1979)] globally on the whole pre-processed sub-volume (Gaussian difference) to obtain the cleavage planes.

The main idea of the Otsu method is to divide the voxels in two classes based on their grey level value. The voxels of low grey-value (below the threshold) are assigned to the background, while voxels of high grey-value (above the threshold) are assigned to the foreground. The threshold is chosen such as to minimize the dissimilarity of voxel values

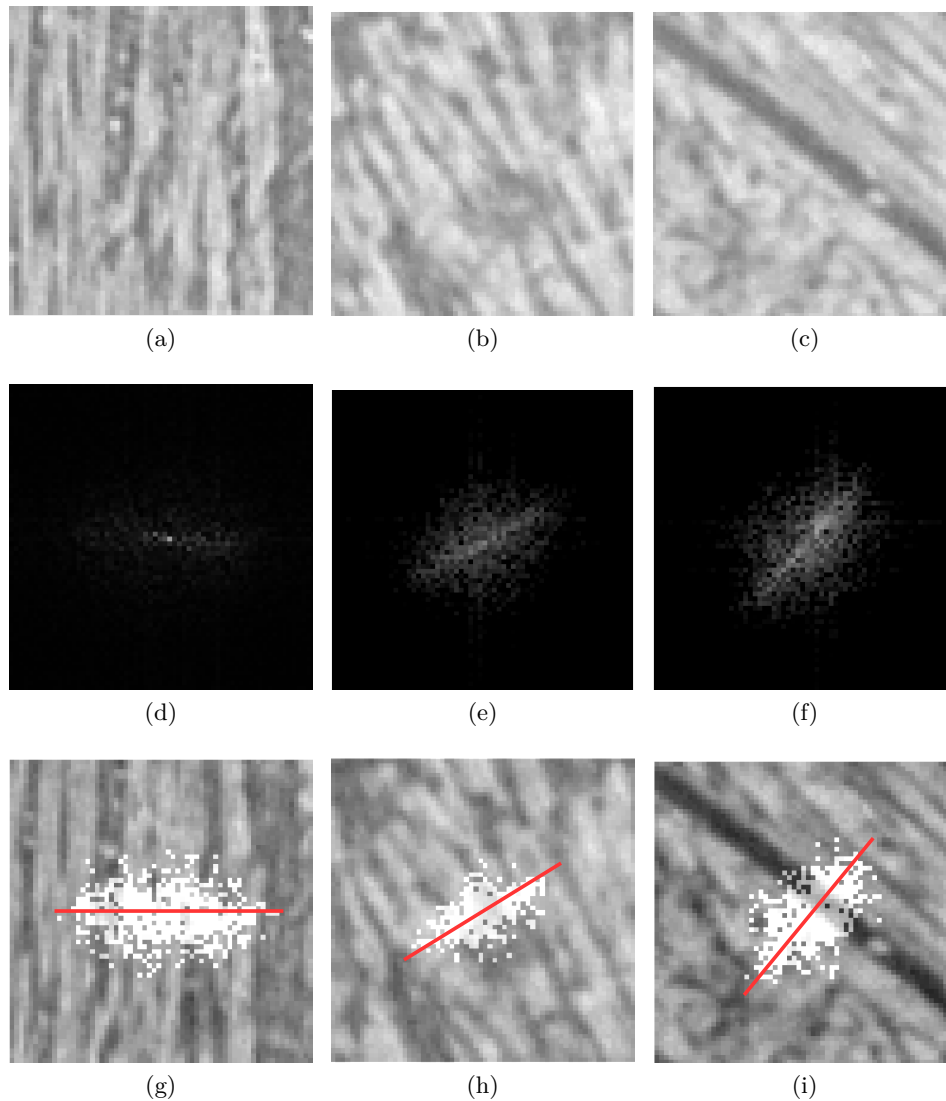


Figure 3.11: (a), (b), (c): 2D sections (256 x 256 pixels) through the samples reconstructed sub-volume shown in Figures 3.8, 3.9 and 3.10 respectively. (d), (e), (f) corresponding slices through the 3D FFT (before thresholding). (g), (h) and (i) represent the 2D sections and the principal direction detected from the thresholded FFT. We see that the spectral components of highest amplitude have a tendency to orient themselves perpendicularly to the discontinuities.

inside each class or equivalently to maximize the dissimilarity of voxel values belonging to different classes. Mathematically, this corresponds to choosing a threshold th that minimizes the intra-class variance:

$$th = \min_t((\sigma_B) \cdot \omega_B(t) + (\sigma_F) \cdot \omega_F(t)) \quad (3.6)$$

where $\sigma_B(t)$ and $\sigma_F(t)$ are the variances of the background respectively foreground grey levels and $\omega_B(t)$ and $\omega_F(t)$ are the proportions of pixels in the background and in the foreground if the threshold t were used.

The normalized histogram $H(j)$ of an image (volume) represents the fraction of pixels with grey levels $j \in 0 \dots G - 1$. From this, $\omega_B(t)$ is computed as

$$\omega_B(t) = \sum_{j=0}^t H(j) \quad (3.7)$$

and $\omega_F(t) = 1 - \omega_B(t)$.

3.3.4 Binarisation step - threshold error analysis

To investigate the impact of the threshold value on the cleavage plane detection and their quantification properties, we choose a ROI from *t1_VGant_z1_pag0003*. We vary the threshold on either side of the Otsu value (-0,012 in this case) with a step of 0.003 and we compare the obtained histograms corresponding to the thickness of the cleavage planes and the distance between them. Figure 3.12 demonstrates that the shape of the cleavage plane thickness histogram remains very similar when the threshold varies around the Otsu value. The histogram corresponding to the distances separating the cleavage planes, Figure 3.13, exhibits more differences when the threshold varies: that can be easily interpreted if we consider that more detected cleavage planes leads to a larger number of short distances between them.

To quantitatively compare the various histograms (Figure 3.13 and Figure 3.12) after normalization, we compute the *Earth Mover's Distance* (EMD), known in mathematics as the Wasserstein metric. The EMD is based on a solution of a transportation problem [Hitchcock (1941)], known as the Monge-Kantorovich problem [Rachev (1985)], that measures the minimum effort necessary to move “amounts” from one bin to another one until the two histograms are the same. The EMD is proportional to the “amount” to move and the distance over which each amount is moved. In the case of normalized histograms, the “amount” represents the percentage of pixels in each bin [Rubner *et al.* (1998)], [Rubner *et al.* (2000)].

Let H_a be the inter-CP distance histogram obtained with a threshold a and H_b the inter-CP distance histogram obtained with a threshold b , and c_{ij} the cost to move a pixel from bin $i \in H_a$ to bin $j \in H_b$. The problem is to find the flows f_{ij} that minimize the

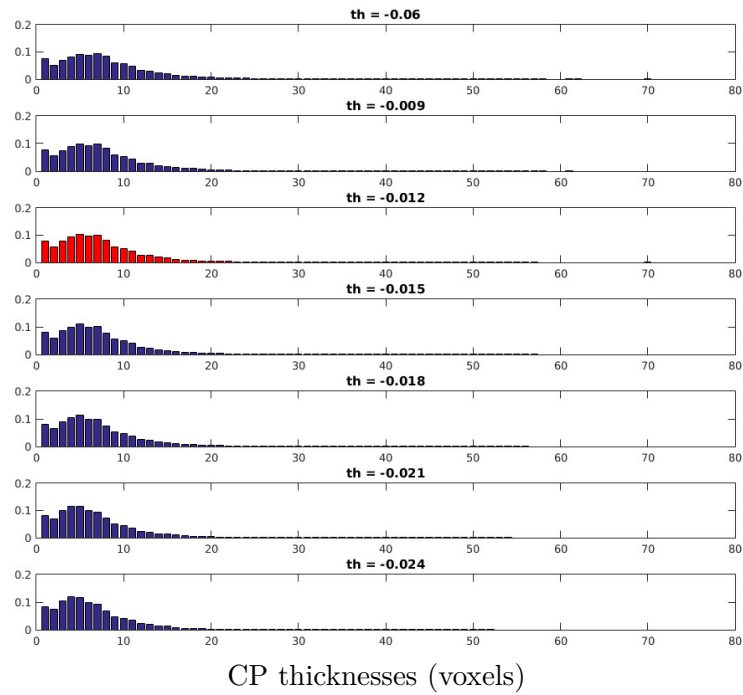


Figure 3.12: *Thicknesses of the detected cleavage planes computed using different threshold values.*

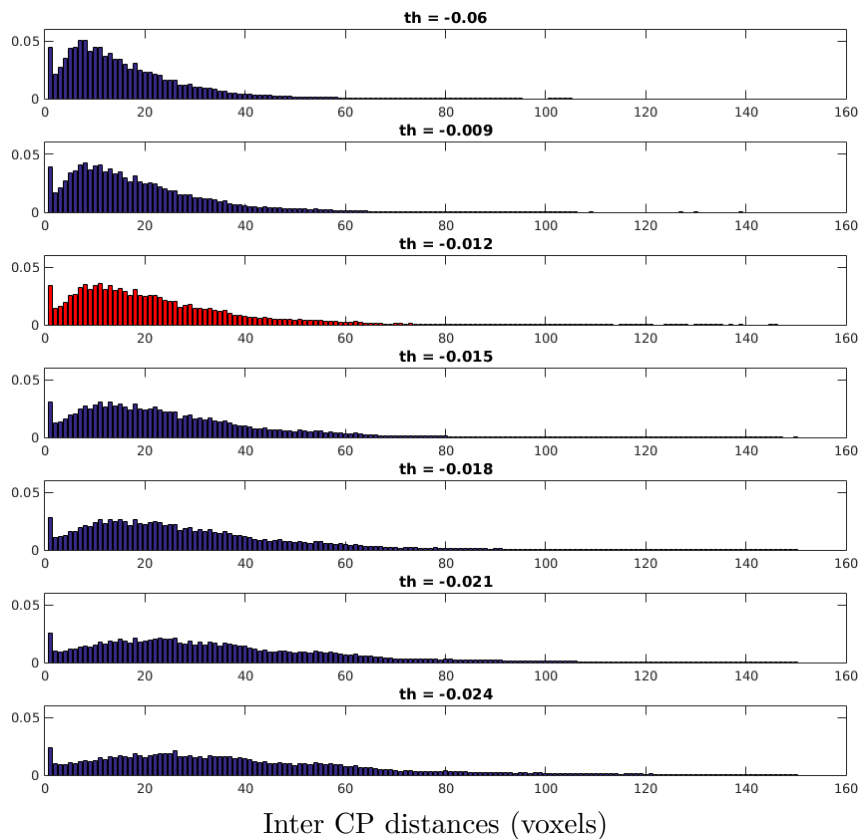


Figure 3.13: *Inter CP distances computed using different threshold values.*

overall cost given by:

$$\sum_{i \in H_a} \sum_{j \in H_b} c_{ij} f_{ij} \quad (3.8)$$

with the constraints:

$$f_{ij} \geq 0, \quad i \in H_a, j \in H_b \quad (3.9)$$

$$\sum_{i \in H_a} f_{ij} \leq \beta_j, \quad j \in H_b \quad (3.10)$$

$$\sum_{j \in H_b} f_{ij} \leq \alpha_i, \quad i \in H_a \quad (3.11)$$

$$\sum_i \sum_j f_{ij} = \min \left(\sum_i \alpha_i, \sum_j \beta_j \right) \quad (3.12)$$

where α_i is the supply of pixels of bin i (its excess above the desired content, if any) and β_j is the capacity of bin j (its deficit below the desired content, if any). The first constraint imposes to move the "amount" only from H_a to H_b . The second constraint imposes that H_b can not receive more than its capacity. The third constraint imposes that H_a can not give more than it contains. The last condition forces to move the maximum amount of supplies possible.

After we found the optimal flow, f_{ij} , the earth mover's distance is defined as the work normalized by the total flow:

$$\text{EMD}(\alpha, \beta) = \frac{\sum_{i=1}^{\alpha} \sum_{j=1}^{\beta} c_{ij} f_{ij}}{\sum_{i=1}^{\alpha} \sum_{j=1}^{\beta} f_{ij}} \quad (3.13)$$

The EMD is computed between histograms obtained with successive threshold values (a single step inside the threshold variation interval), then between histograms obtained with the two extremes of the threshold interval.

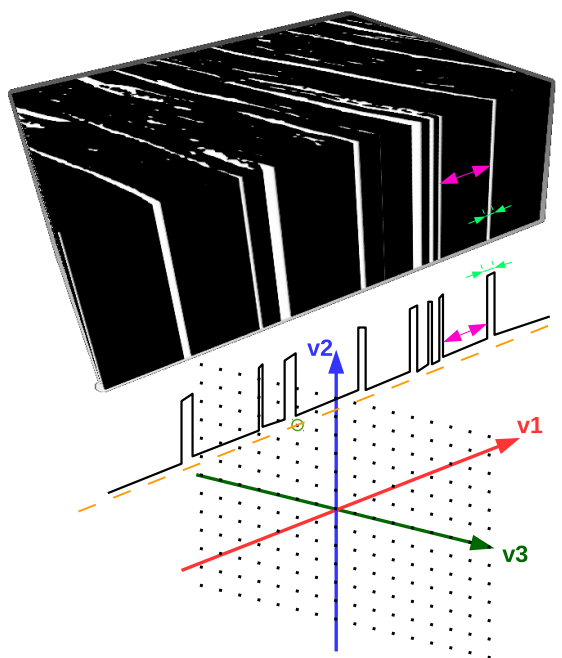
Results obtained for the various histograms corresponding to the inter CP distances and CP thicknesses for each threshold used are presented in Table 3.1. Globally the evolution of the histogram remains low even if new short distances appear.

The EMD between the histograms of cleavage plane thicknesses obtained with $\text{th} = -0.006$ and a $\text{th} = -0.024$ is 1,24 voxels. This can be interpreted as a very small change (on average of about 1,24 voxels) of the average thickness. It is very low, meaning a high stability in the results.

The EMD between the inter-cleavage plane distance histograms obtained with $\text{th} = -0.006$ and a $\text{th} = -0.024$ is 21.55 voxels. It is much larger than the EMD for thicknesses, but this is normal, because the X axis in the histograms covers a much broader range, therefore the movements are done on a greater distance.

Value 1	-0.006	-0.009	-0.012	-0.015	-0.018	-0.21
Value 2	-0.009	-0.012	-0.015	-0.018	-0.21	-0.24
Earth mover's inter CP distances	2.96	3.26	3.44	3.68	3.96	4.23
Earth mover's CP thicknesses	0.31	0.23	0.20	0.17	0.16	0.15

Table 3.1: Earth mover's distance

Figure 3.14: *Virtual line creation.*

3.4 Cleavage planes thicknesses and inter-cleavage planes distances

3.4.1 Virtual lines creation

After the main orientation extraction using PCA, the next step is to create the virtual lines in order to compute the inter cleavage plane distances and the cleavage plane thicknesses. The first step is to choose the center of each line that crosses the 3D volume perpendicular to the main direction of the CP (in the direction of the first vector obtained using PCA). Line centers are taken on a rectangular grid, with the grid axis given by the other two directions (v_2 and v_3) obtained from PCA, like in Figure 3.14. A very dense grid step of 1 voxel is used (about 330000 lines per subsample). Through these centers, we take lines in 3D aligned with the principal vector v_1 , and on these lines we sample voxels with a step of 1 (rounding the voxel sampling coordinates to the closest integer values) in the binary image. We then measure the widths of continuous dark areas (myocyte sheets, inter-cleavage plane distances) and of continuous white areas (cleavage plane thicknesses) (see Figure 3.14) and include each measurement, from each line, in the statistics.

The statistics are presented in the form of histograms of inter-cleavage plane distances

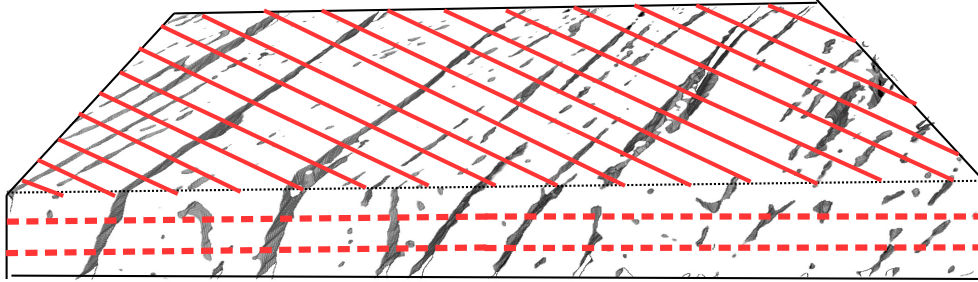


Figure 3.15: Zoom on the lines (solid red) crossing the image. The red dots illustrate that the lines, placed at a certain distance from one another in all directions, cross the entire volume, not just the top surface shown.

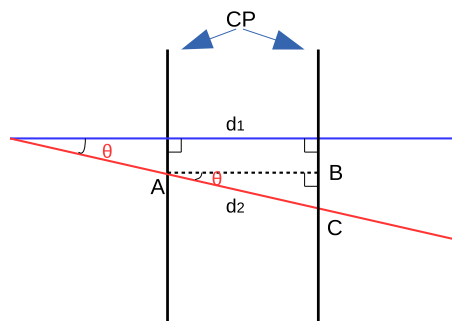


Figure 3.16: Virtual line error analysis. Black lines represent the CPs, the blue line represents the virtual line orthogonal to the CPs and the red line represents the virtual line with a slightly rotated orientation.

and histograms of cleavage plane thicknesses per each tissue sample, such as in Figure 3.22g and Figure 3.22h). The entire statistics computation process is illustrated in Figure 3.3.

3.4.2 Main direction error analysis

In theory, the distance and thickness measurement error introduced by an error in the PCA main vector orthogonality to the CP is given by the formula: $d_2 = d_1 / \cos(\theta)$, with d_1 the true measurement and d_2 the measurement with a slightly rotated orientation by an angle θ (see Figure 3.16). In practice, due to the discrete space in which we work, there might be additional errors coming from the slightly different sampling on the lines generated in the second orientation. The goal is to check if these errors are significant.

The error induced by the main direction extraction is analysed on a synthetic volume. The synthetic volume creation is presented in the next section. On the synthetic volume, the main directions obtained using PCA are rotated with 10° around all 3 coordinate axis. The results are presented in Figure 3.17. As can be seen, the histograms of the inter CP distances and of the CP thicknesses are very similar. The mean inter-CP distances and mean CP thicknesses have only a small variation between each rotation case, as can be

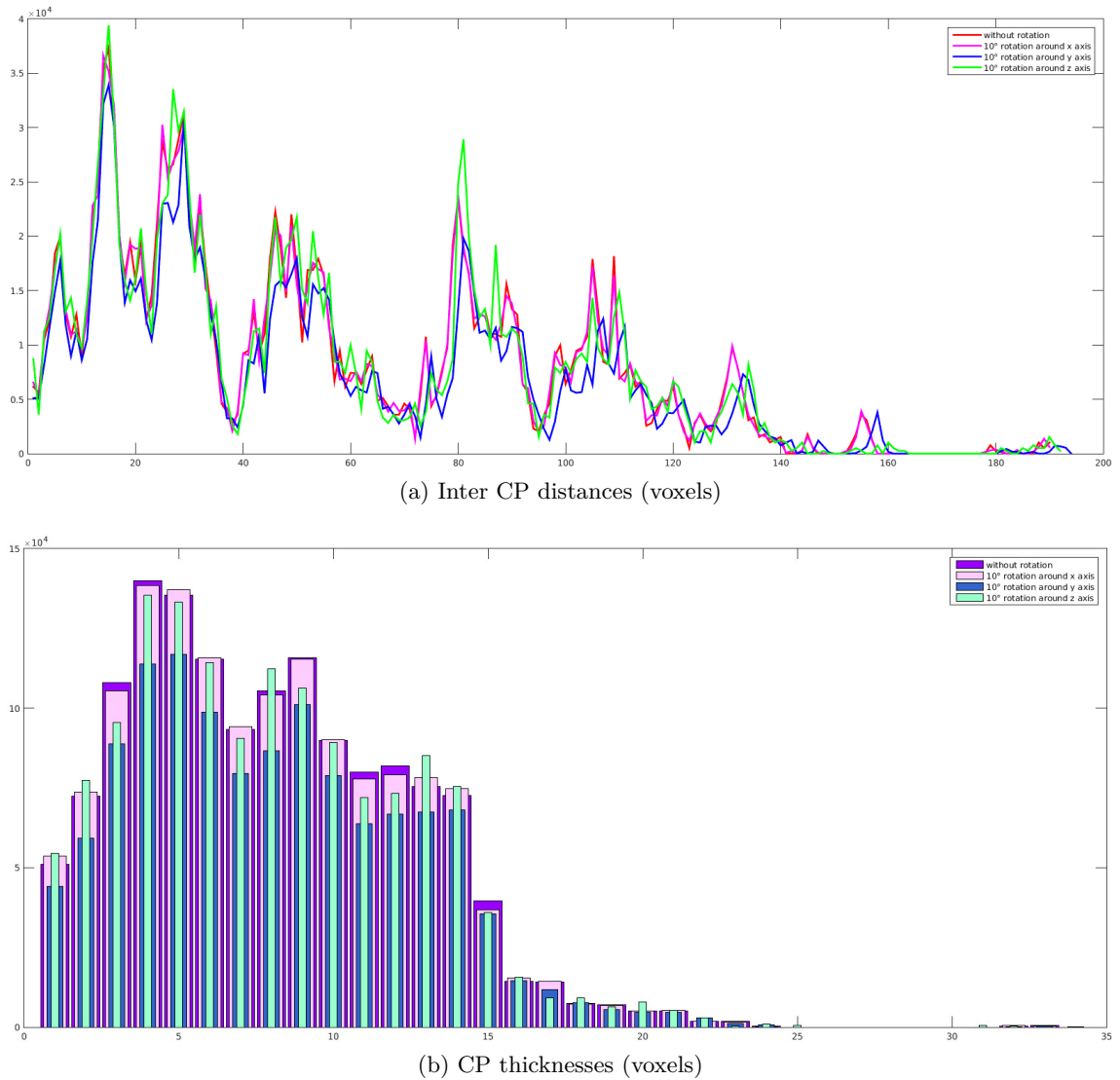


Figure 3.17: *Inter CP distance histograms (3.17a) and CP thickness histograms (3.17b) obtained using the original direction from PCA, and rotations of this direction by 10° around each coordinate system axis.*

seen in Table 3.2. In conclusion, as long as the orientation error is small, the distance and thickness measurements are not affected significantly.

3.5 Methodology Evaluation

3.5.1 Creation of a synthetic volume

In order to validate our protocol for the automatic extraction of cleavage planes and computing statistics of their thickness and the distance separating them, we create a synthetic volume of reference. First we extract a planar section (thickness 1 voxel) from a reconstructed slice (thickness 256 voxels) of an actual sample of 3D tissue (Figure 3.18). Second, we create a new 3D volume by duplicating this section 256 times in the z direc-

mean	without rotation	10° around x axis	10° around y axis	10° around z axis
inter-CP distances (voxels)	8.20	8.20	8.33	8.25
CP thicknesses (voxels)	54.93	54.88	54.67	54.90

Table 3.2: Inter-CP distances and CP thicknesses mean

tion to get a synthetic slice of reference that respects the thickness of the original one. Figure 3.18 illustrate the creation process of the synthetic volume of reference. In this reference volume, the cleavage planes have the same orientation in every z section (due to the duplication process) and they are strictly orthogonal to each z section. Let us note that the cleavage planes are almost parallel in each section with a given global orientation. We have verified that the correct orientation was correctly recovered using the PCA method from our algorithm. In Figure 3.19 we automatically represent the lines obtained using our algorithm. The lines are orthogonal to the cleavage planes direction.

The orientation was computed on the entire volume, but for manual and for automatic measurements of the distance and thickness, we extract a subvolume presented in Figure 3.18. On this subvolume we verify the agreement between the automatic and manual measurements.

The manual measurements were made using the Seg3D [CIBC] software and they are presented in Figure 3.20 and Figure 3.21. 100 lines have been traced for distance measurements and 184 lines for thickness measurements. As can be seen in the two figures, the measurements were made only in the z plane, because cleavage planes are guaranteed to be orthogonal to each slice.

Figure 3.22 shows the results of the manual and the automatic measurements (with line spacing=1). The two measurements, automatic (with line spacing = 1) and manual, of the distance between cleavage planes present the same peaks (the first 4 peaks are identical in values) and also similar shapes. The histograms corresponding to the cleavage plane thicknesses also have similar shapes. The maximum peaks are shifted by just one unit (one pixel). The main cause is due to sampling: the boundaries of cleavage planes cannot be known with subpixel precision, and the lines crossing the image are also sampled in pixel coordinates, therefore measurement errors of ± 1 pixel are to be expected. Since for the thicknesses we are measuring something very small, such an error is immediately noticeable.

For the manual measurement, a line spacing of 1 pixel is out of the question. We made measurements only in places where there were features of interest (cleavage planes) and we tried to keep the line spacing more or less regular. On average, manual distance measurements have a line spacing of 44 pixels, with a minimum spacing of 20 pixels and a maximum spacing of 44 pixels. For manual thickness measurements, the average line spacing is 23 pixels, with a minimum of 3 pixels and a maximum of 64 pixels.

In order to see how the line spacing influences the results we do two more rounds of automatic measurements with line spacings of 44 and then 23 pixels. The results are shown in Figure 3.23a and Figure 3.23b. It can be seen that for the case of automatic

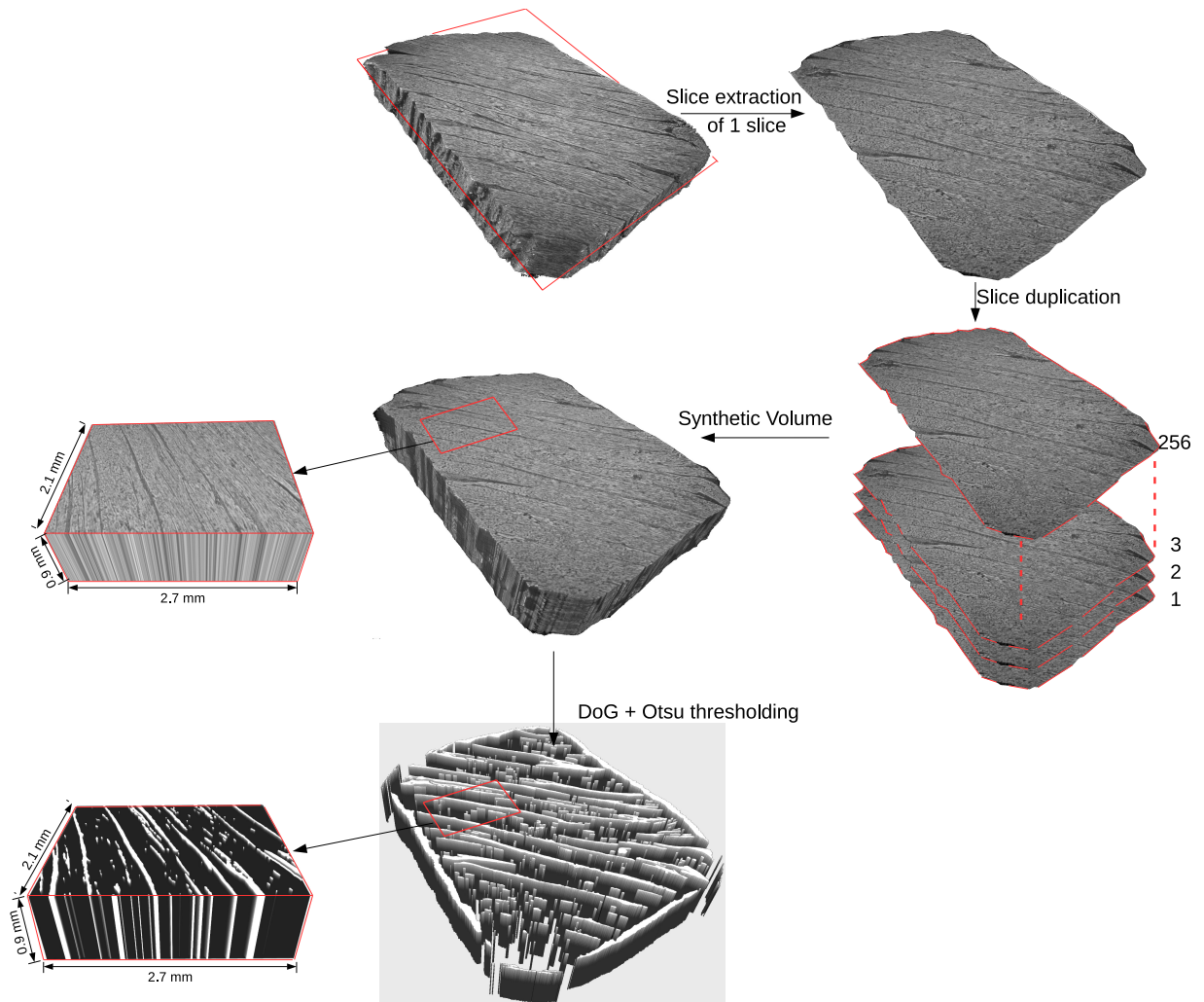


Figure 3.18: *Synthetic volume construction for testing the methodology: a slice is selected from the original volume and duplicated to re-achieve the original 3D image size. On this synthetic volume we apply the same methodology as shown in Figure 3.3.*

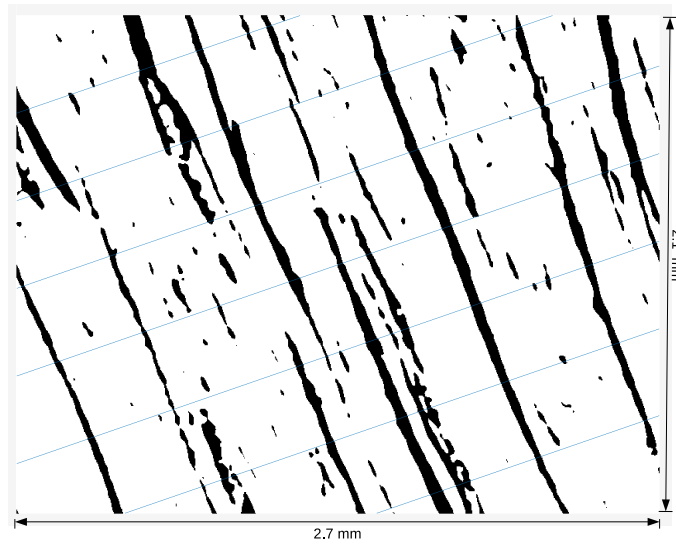


Figure 3.19: Automatic lines (blue) displayed in the main orientation perpendicularly to the CP: $[0.9452 \ 0.3265 \ 0]$ with a spacing of 100 pixels.

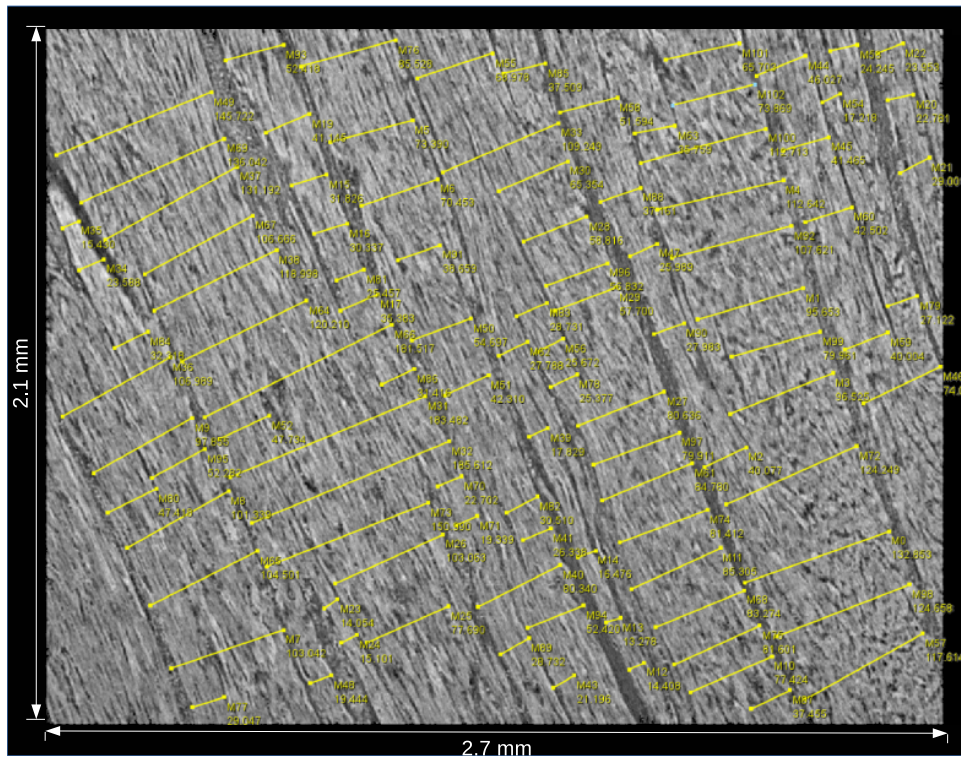


Figure 3.20: Manual measurement of distances between cleavage planes. The measurements are made using the Seg3D tool.

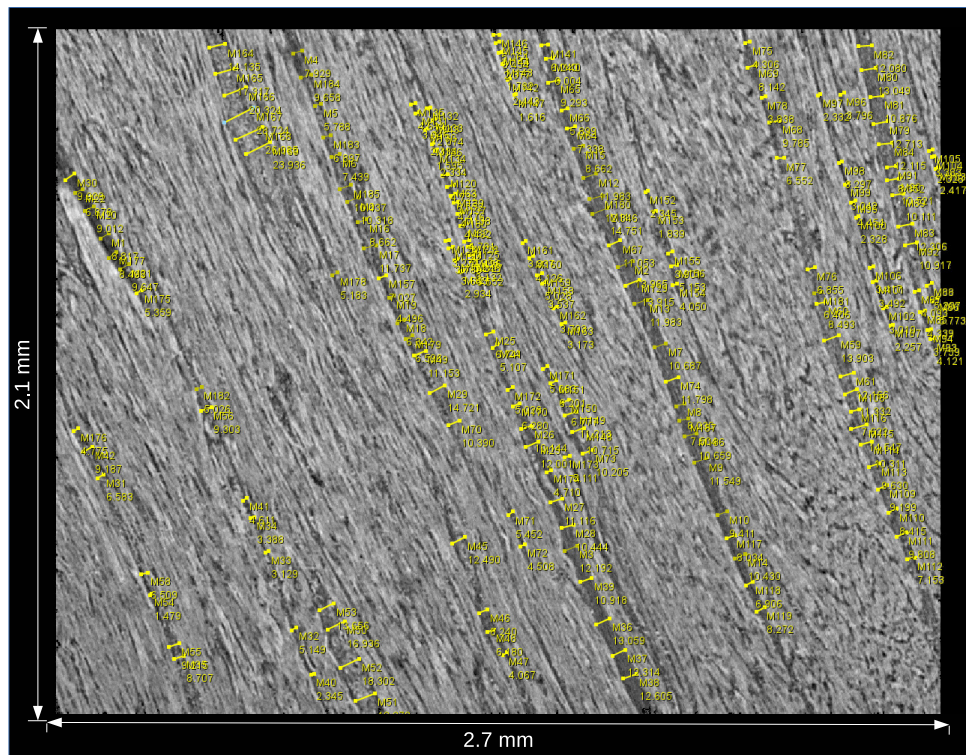


Figure 3.21: *Manual measurement of the thicknesses of the cleavage plane. The measurements are made using the Seg3D tool.*

measurements using a line spacing equal to 23 pixels, a line spacing of 1 pixel and manual measurement the general shape and the peaks of the histograms remain the same. In the case of the automatic measurement with line spacing of 44 pixels, the histogram shape changes due to the small number of measurement lines and their location (not necessarily passing through interesting features in this small sample). However the peaks remain in almost the same position, except the first value. For the automatic thickness measurement, the histogram changes more because the sample is small and there are few lines crossing features of interest to build a meaningful statistic.

3.6 Conclusion

We analysed the perimysium extracellular matrix of the human cardiac tissue obtained with 3D X-ray Phase Contrast μ -CT. We developed a method in order to extract the perimysium extracellular matrix and to analyse the inter-cleavage plane distances and their thicknesses. To the best of our knowledge, this is the first time that the 3D perimysium extracellular matrix is analysed and we do not have any other study from the literature with which to compare our results. This is why much attention was given to the evaluation of our method and we study the error induced by each step of our method.

First, we study the impact on the inter CP distances and their thicknesses introduced by the binarisation method. The results show that the statistical results of the CP thick-

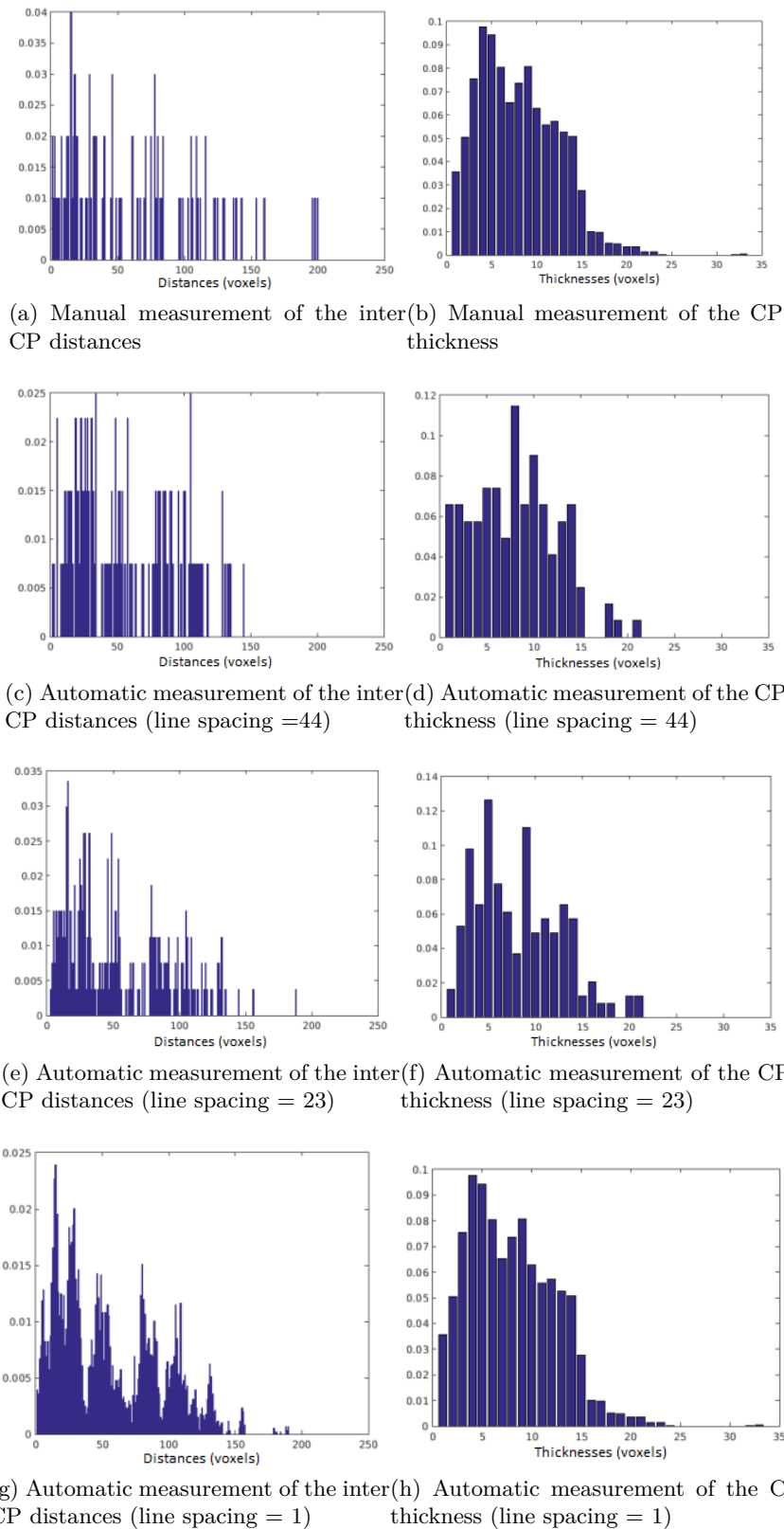
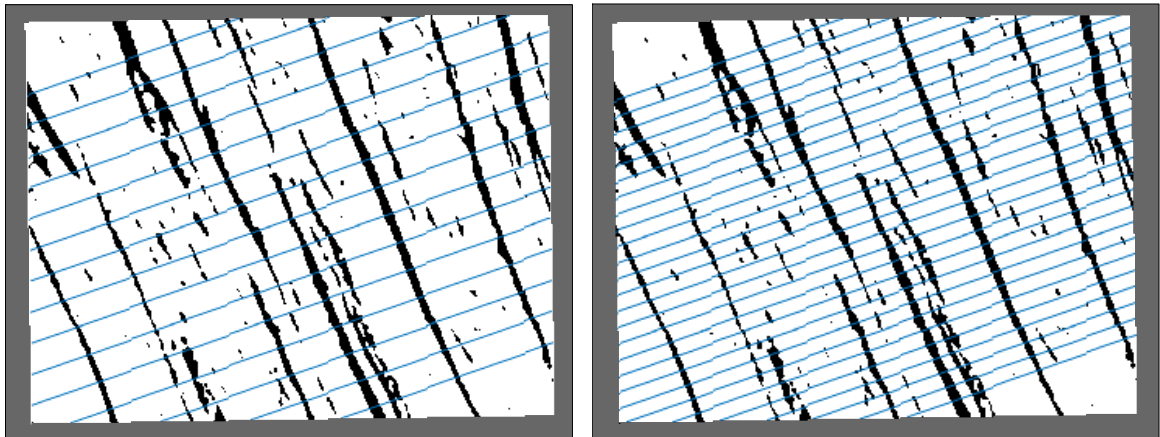


Figure 3.22: *Statistical study of distances between cleavage planes and thicknesses of cleavage planes using the automatic method with different line sampling and a manual measurement.*



(a) Automatic measurement (line spacing = 44 voxels) (b) Automatic measurement (line spacing = 23 voxels)

Figure 3.23: *Lines (solid blue) crossing the image (a) line spacing=44 voxels, line spacing=23 voxels (b).*

nesses are similar if we vary the binarisation threshold. The inter CP distances exhibit more differences when the threshold varies: that can be easily be interpreted if we consider that a larger number of detected cleavage planes increases the number of short distances between them.

Afterwards, we analyzed the distance and thickness measurement errors introduced by an error in the PCA main vector orthogonality. The inter CP distances and the CP thicknesses are very similar, the mean values having only a small variation between each angle deviation case. In conclusion, as long as the orientation error is small, the distance and thickness measurements are not affected significantly.

Finally, the entire methodology is evaluated. The statistical results of the inter CP distances and the CP thicknesses are computed on a synthetic volume, the results being compared to a manual measurement. The evaluation method reports good agreement between the automatic and the manual method.

Cleavage Planes: statistical analysis

Plans de clivage: analyse statistique

4.1 Introduction

The purpose of this chapter is to quantitatively analyse the perimysium extracellular matrix for all ESRF samples presented in Chapter 2. The method used was presented in Chapter 3. This chapter is focused on the method application on the entire transmural samples. All the steps presented in Chapter 3 are applied on small parts of the sample, keeping into account that the direction of the CPs is changing smoothly. We present for one transmural sample all the intermediate results after each step for quantifying the inter-CP distances and the CP's thicknesses. We also analyse the error that may appear based on the main direction extraction on a region of interest (ROI).

We compare the statistical results obtained using a main orientation extracted from a sub-ROI from the centre of the sample with the results obtained from splitting the entire ROI in 64 sub-ROI's of equal size. The statistical inter-cleavage plane distances and the CP's thicknesses results for all the samples are presented and analysed. The results show that the thickness of CP roughly varies between $24 \mu m$ and $59 \mu m$ and that the distance inter-CP varies approximately between $70 \mu m$ and $280 \mu m$, with significant local variations of the standard deviation.

We compare the samples from the posterior, anterior and lateral left ventricle from slice 1 of heart number 2 among themselves. A second sample group that we compare consists of 3 anterior left ventricle samples: from slice 1 of heart 2, from slice 2 of heart

2, and from slice 5 of heart 1. A third sample group that we analyse consists of the anterior and posterior septum samples from slice 1 of heart 1. The fourth group consists of two antero-posterior septum samples from slice 2 of heart 2. The conclusion is that all the samples have their own particularities, and their inter-CP distances and the CP thicknesses are not similar, although there are regions of similarity. The CP thicknesses and the inter-CP distances of the anterior, posterior and lateral left ventricle from slice 1, from the same heart, are in general different, with some regions with similar values. The anterior and posterior septum inter-CP distances are similar from the midwall until 100% wall depth. The CP's thicknesses are very similar for the anterior and posterior septum, as well as for the antero-posterior septum samples.

4.1.1 Statistical analysis of the transmural laminar microarchitecture of the human left ventricle (sample 1, LV_ant_S5_1)

As can be seen in the study presented in Chapter 2, the perimysium extracellular matrix forms the cleavage planes. The cleavage planes are locally parallel one to the other and smoothly change their spatial orientation. For this reason, all the steps presented in Chapter 3.3, in order to extract statistics about cleavage planes thicknesses and distances, will be applied on small slices or ROIs of the reconstructed volume, of dimensions 2048 x 2048 x 256 voxels ($7 \times 7 \times 0.9 \text{ mm}^3$).

4.1.2 Segmentation step

Figure 4.1a shows the reconstruction of the anterior left ventricle sample (*t5_ech18*). We divide it into 32 Regions Of Interest (ROI) that are separately analysed. In Figure 4.1b we present a sub-region of the ROI 19 obtained after the application of the DoG method. Its corresponding histogram is given in Figure 4.1c). The two classes: background and perimysium can be separated by using the Otsu thresholding method. The Otsu threshold assumes Gaussian distributions for the foreground and background gray levels and is chosen such that it minimizes the intra-class variance.

We can obtain the perimysium extracellular matrix for the entire sample presented in Figure 4.1e by applying the Otsu thresholding method separately on the Difference of Gaussians of each of the 32 ROI, then reassembling the thresholding results back into a large volume (Figure 4.1e). Working on small parts rather than on the entire volume at once is easier because the entire volume is very large (30 GB) and requires a lot of memory to process. Additionally, due to variations throughout the sample (partly due to acquiring the entire volume in several stages), the Otsu threshold might not be exactly the same from one part to the next. We plot the Otsu threshold for each of the 32 ROI in Figure 4.1d, where we see that there are indeed some small variations of the threshold (on the scale of 10^{-3}).

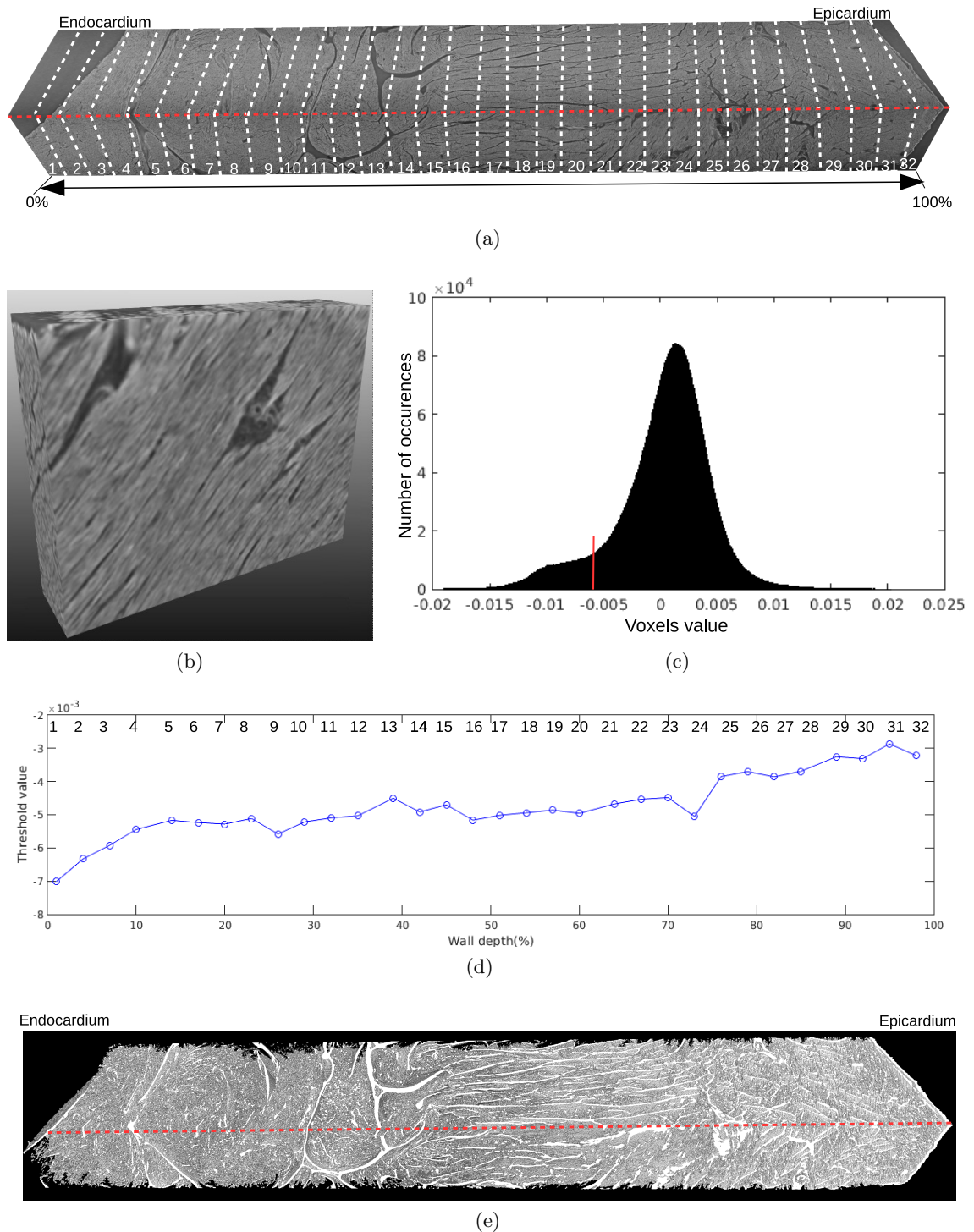


Figure 4.1: *a) Sample extracted from the anterior left ventricle sample, slice 5 (LV_ant_S5_1). b) Difference of Gaussians (DoG) of ROI 19. c) Histogram of the DoG image (b). d) Otsu threshold of each ROI. e) Reconstructed thresholded sample showing the 3D extracellular matrix.*

4.1.3 Orientation detection

ROI The main orientation orthogonal to the cleavage planes is extracted on each of the 32 ROIs separately, on a central sub-region of $256 \times 256 \times 256$ voxels, ($0.9 \times 0.9 \times 0.9 \text{ mm}^3$) as can be seen in Figure 4.2a. After extracting the main orientation from this central region, we then compute statistics about the cleavage planes' thicknesses and distances between successive planes along this orientation, on the whole ROI using the line grid procedure discussed in Section 3.4.

As can be seen in Figure 4.2b, the main orientation sometimes varies abruptly (the angles between the orientations of the successive ROIs are plotted in Figure 4.2c). One of the reasons for these abrupt variations is the existence of two or more principal directions in the ROI, that cannot be described well using only second-order statistics (eigenvectors and eigenvalues from the PCA of the thresholded FFT, see Section 3.3.2). In this case the eigenvalues can offer some information related to the significance of the "main" orientation extracted. The "main" orientation is properly defined by second-order statistics when the first eigenvalue is sufficiently larger than the other two eigenvalues. Figure 4.2d plots the eigenvalues for the 32 ROI. As can be seen, in ROI 21 the first two eigenvalues are very close, which may indicate the presence of two "main" orientations. Another reason can be the existence of a large cleavage plane or boundary that does not continue in the next subvolume, as can be seen in the first three ROI (in this case, we are affected by the very edge of the sample).

Sub-ROI In order to analyse the error introduced by the fact that the main orientation is chosen taking into account only a central cube of $256 \times 256 \times 256$ voxels, a ROI of $2048 \times 2048 \times 256$ has been split into 64 cubes of $256 \times 256 \times 256$ voxels (Figure 4.4a). For each cube, the main orientation is extracted, and then the distances and thicknesses statistics were computed. The results are shown in Figure 4.4c and Figure 4.4e. The ROI chosen for testing is ROI 21 from Figure 4.1a.

In ROI 21, the mean distance between successive CP obtained using the main orientation of the FFT (method presented in Chapter 3.3.2) extracted from the central cube of $256 \times 256 \times 256$, is 50 voxels, with a standard deviation of 37 voxels (Figure 4.2e). The average distance between successive CP, computed with orientations extracted individually for each cube of $256 \times 256 \times 256$ voxels, is 40 voxels with a standard deviation of 26 voxels Figure 4.4c. Such large standard deviations, comparable in size to the average value, are normal when we consider the type of distribution that the inter-CP distances have, as the possible distances experience a wide range of values. Considering this, the two average distances of 40 respectively 50 voxels are relatively similar.

As for the cleavage plane thicknesses, computing them using the orientation extracted from the central cube yields a mean thickness of 9 voxels with a standard deviation of 6 voxels. Computing with orientation extracted for each cube separately yields a mean thickness of 8 voxels with a standard deviation of 5 voxels. (Figure 4.4c). The difference

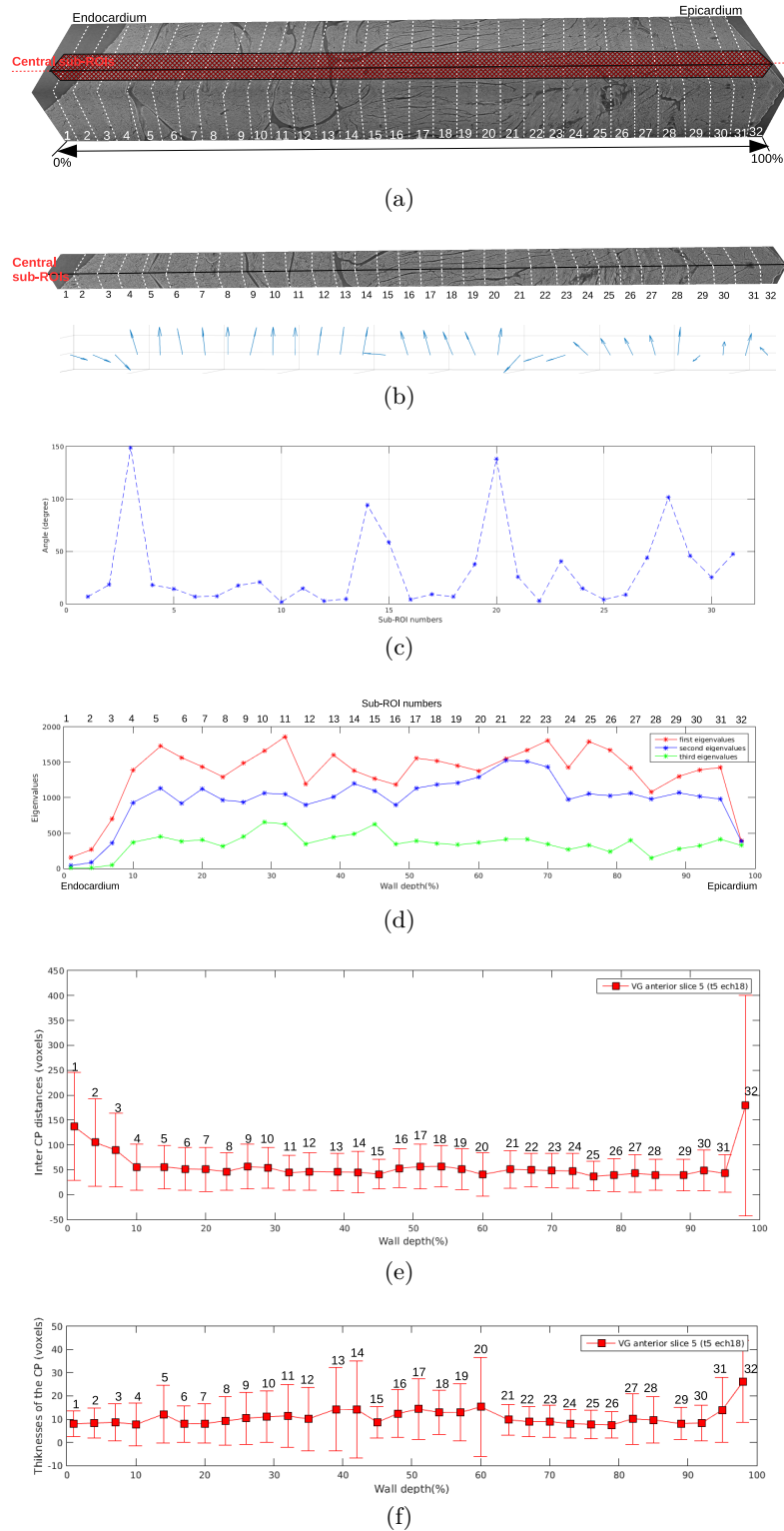


Figure 4.2: *a) Sample extracted from the anterior left ventricle, slice 5 (LV_ant_S5_1), with the central sub-ROIs (in red). b) Series of the 32 central sub-ROIs with their main individual CP orientation . c) Angle between two consecutive individual main orientations. d) Eigenvalues corresponding to each of the 32 ROIs. e) Inter CP distances computed for each of the 32 ROIs (average values and standard deviations). f) Thicknesses of the CP computed for each of the 32 ROIs (average values and standard deviations).*

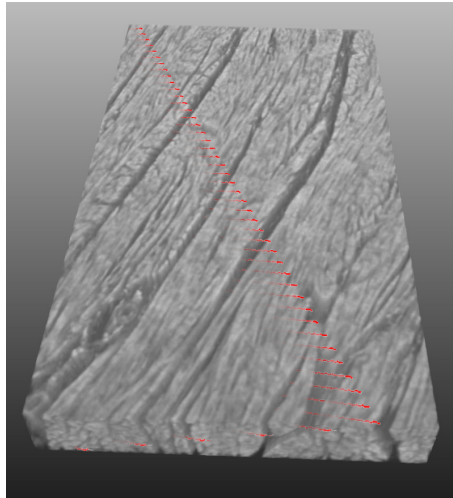


Figure 4.3: A part cropped from ROI 29 with the red lines showing the orientation extracted from the FFT.

between the mean and the SD of each sub-ROI cube compared to the whole ROI 21 comes from the fact that the main orientation is not always perpendicular to all the cleavage planes, as can be noticed in Figure 4.3.

4.1.4 Cleavage planes statistics of the anterior left ventricle (sample 4, LV_ant_S1_2)

The cleavage planes can be clearly seen throughout the sample (Figure 4.5a). Close to the epicardium, the structure appears more fragmented, with shorter cleavage planes with many ramifications; an artery is also visible. In the midwall, the structure is more regular, with many long, parallel cleavage planes. Towards the endocardium, the myocytes are more tightly packed in larger groups, separated by large, curved cleavage planes.

Excluding ROIs 1, 2, 18 and 19, for which distance and thickness statistics are affected by the large number of voxels that fall outside the sample, the mean distances between cleavage planes from ROI to ROI vary between 41 voxels and 60 voxels ($143\text{-}213\mu\text{m}$), with standard deviations of around 40-50 voxels ($140\text{-}175\mu\text{m}$). There is a tendency for distances to be greater in the middle ROIs, but considering the standard deviations, the tendency is not significant.

As for the mean cleavage plane thicknesses, again excluding the two extreme ROIs on each side, the means are between 7-16 voxels ($24.5\text{-}56\mu\text{m}$), slightly greater in ROIs 3, 4 and 5 because of the large cleavage planes present. The variances are also greater in these ROIs, because we still have small cleavage planes, as well as large ones.

The distances and thicknesses histograms for each of the 19 ROIs are plotted in Figure 4.6. For distances, histograms for ROIs 2-12 are relatively similar, with ROIs 2-5 having somewhat larger distances. There is a break in ROI 13, caused by volume merging artifacts. Afterwards, the histogram shape shows higher weights for low distances, in accordance with the strong fragmentation of the ROIs. The thickness histograms appear

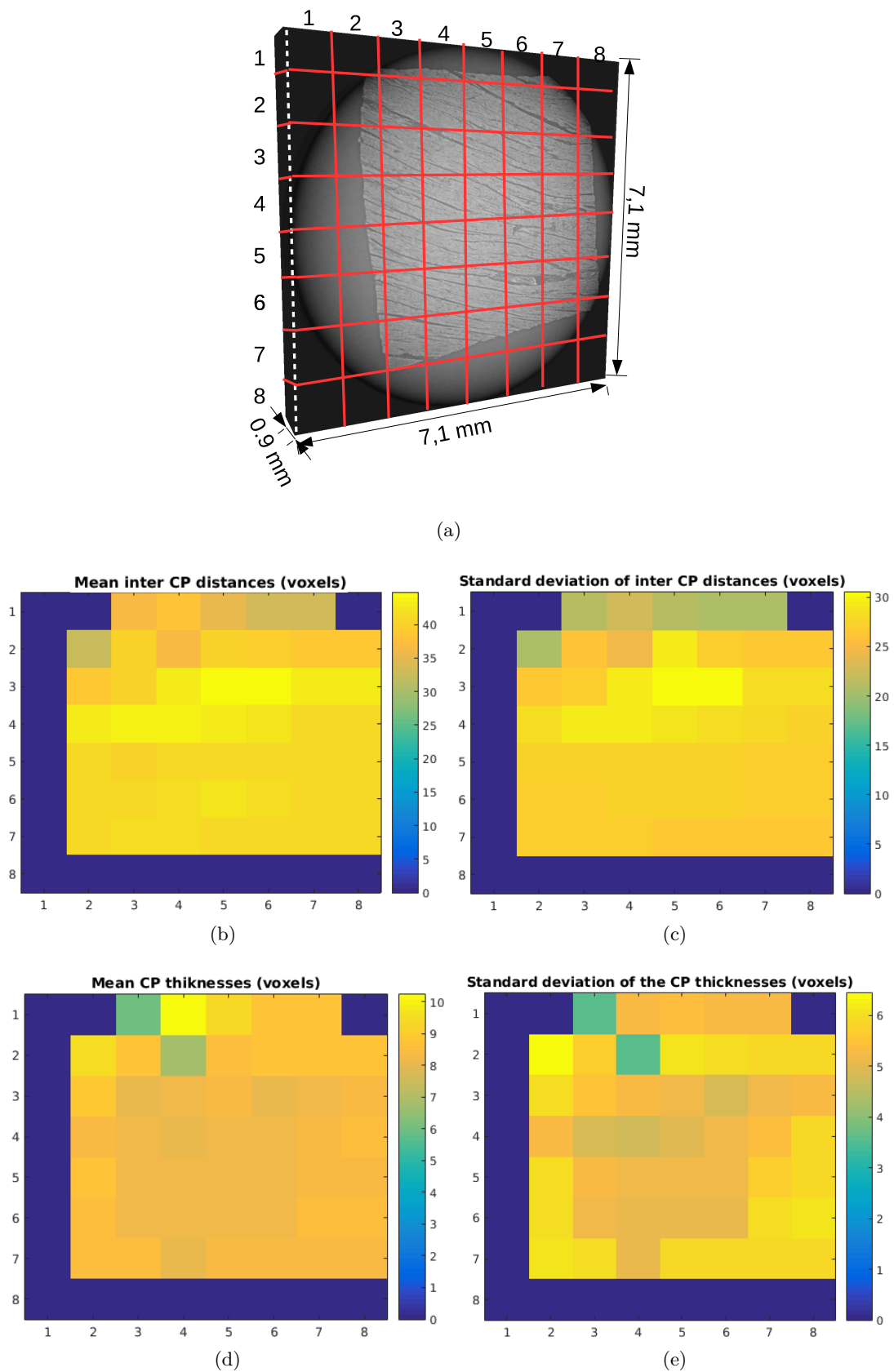


Figure 4.4: a) ROI 21, split into 64 parts of $256 \times 256 \times 256$ voxels, for which the main orientation of the FFT is extracted separately. b) Inter-CP distances extracted for each part. c) Thicknesses of the CP extracted for each part.

more or less similar, with the exception of the outermost ROIs which have too many voxels outside the sample.

4.1.5 Cleavage planes statistics of the posterior left ventricle (sample 6, LV_post_S1_2)

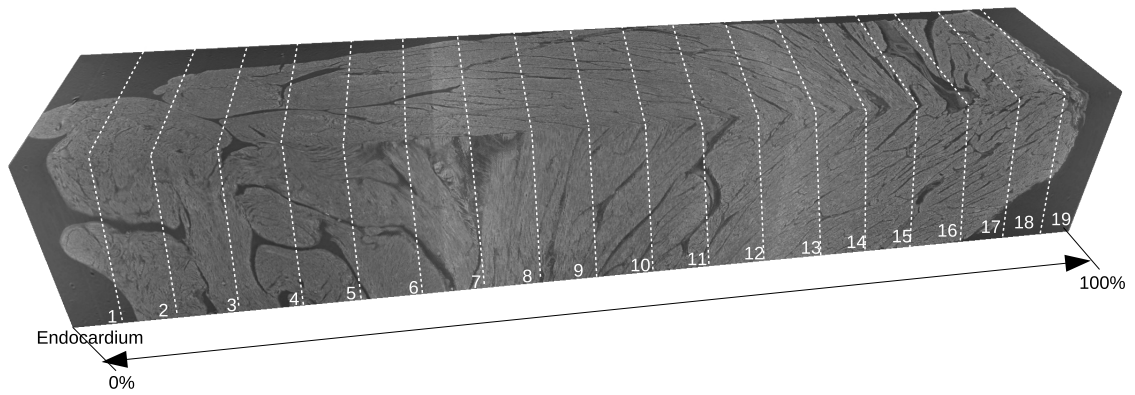
The cleavage planes can be clearly seen throughout the sample (Figure 4.7a). From the endocardium until the middle of the sample, the structure appears to be regular, with parallel cleavage planes. In the middle of the sample the structure becomes more fragmented, with changes in the direction of cleavage planes and with many ramifications visible especially in ROIs 10 and 11 (Figure 4.7d). Close to the epicardium the cleavage planes are shorter and thinner, less evident at this display size. A large cleavage plane containing several arterioles and venules can be seen in ROIs 15-17 (Figure 4.7d).

The average distances inter cleavage planes in the posterior left ventricle are between 22 and 63 voxels ($77 \mu m - 220 \mu m$). Close to the endocardium (ROIs 2-8) there are more fluctuations because of long, curved cleavage planes (Figure 4.7b). Starting from ROI 10 until the epicardium, the change in structure, with many CP ramifications at first and then the CP becoming less evident and less numerous (also see Figure 2.18b) means that the distance statistics become less relevant. The CP mean thicknesses are between 7 and 17 voxels ($24 - 59 \mu m$). Close to the epicardium (where the CP are not in sufficient number) or in zones with many ramifications (there the CP are no longer parallel to each other) the extracted values are not reliable. The distributions of the inter CP distances and of the CP thicknesses are shown in Figure 4.8.

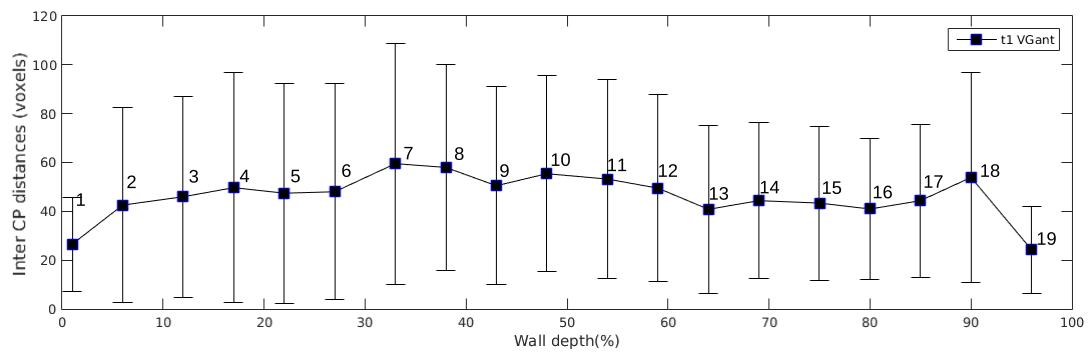
4.1.6 Cleavage planes statistics of the lateral left ventricle (sample 5, LV_lat_S1_2)

Close to the epicardium, the mean inter CP distance is approximately 50 voxels ($175 \mu m$) and the mean CP thickness is approximately 10 voxels ($35 \mu m$) (Figure 4.9). A large cleavage plane with a visible artery (in an almost longitudinal section) can be seen in ROIs 11-17 (in ROI 17, on the top face, we can see the artery in a crosswise section). In ROIs 15-18, the structure is relatively compact because most of the CP are thin, and regular because the CP are parallel to each other. In the midwall (ROIs 8-14), the structure remains regular, with long, parallel cleavage planes, but there is a large change in the CP direction compared to the epicardium. The CP are also thicker than in the epicardium, visible in the graph and confirmed visually.

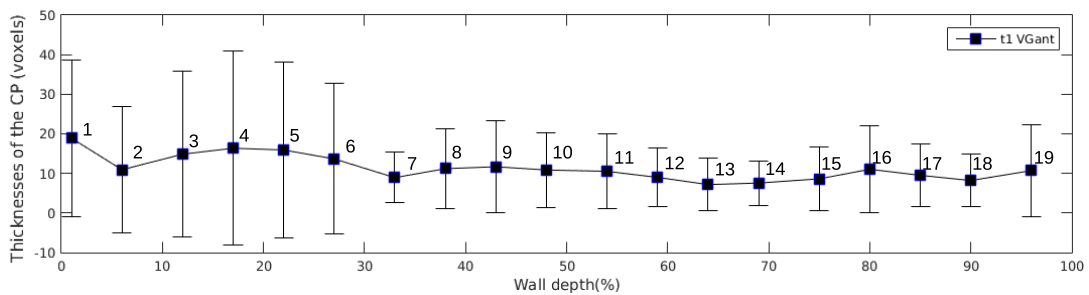
Advancing towards the endocardium, there is a change in the type of structure from ROI 7 to ROI 1. The tissue is organised into "folds" with wide, long but highly curved separations in between. This is reflected in an increase of the mean inter CP distance. The irregularly curved structure also causes large fluctuations in the average inter CP distances, between 44-85 voxels ($154 - 297 \mu m$) and large variances.



(a)



(b)



(c)

Figure 4.5: a) Sample extracted from the left anterior ventricle, slice 1 (LV_ant_S1_2). b) Distances between successive cleavage planes (CP) in each of the 19 ROIs (average values and standard deviations). c) Thicknesses of CP in each of the 19 ROIs (average values and standard deviations).

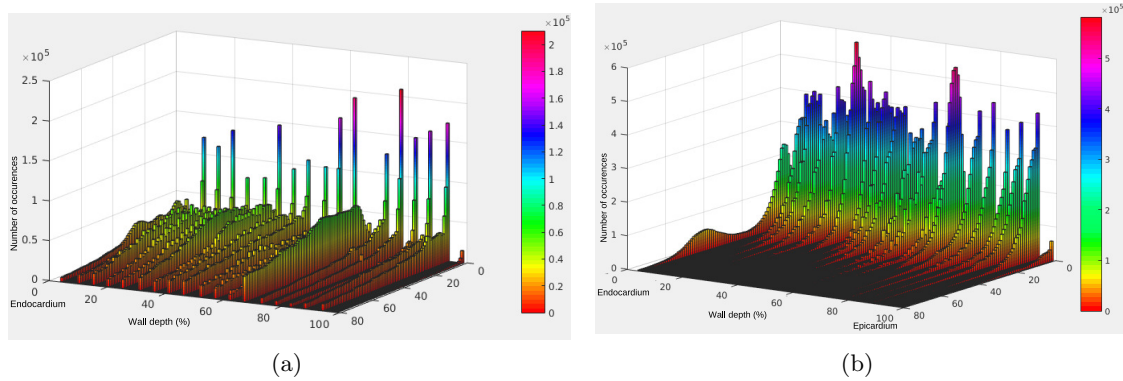


Figure 4.6: *Distribution of the Inter-CP distances (a) and CP thicknesses (b) of the anterior left ventricle from slice 1 (LV_ant_S1_2) computed for each ROI from the endocardium (wall depth 0%) to the epicardium (wall depth 100%).*

4.1.7 Cleavage planes statistics of the samples from slice 1 of the left ventricle (sample 4, 5, 6, LV_ant_S1_2, LV_lat_S1_2, LV_post_S1_2)

In Figure 4.10a is presented the comparison between the distances inter CP of all three samples extracted from the slice 1. The lateral left ventricle inter CP distances present a high variation from endocardium to epicardium, the structure being more irregular than the other two samples from sample 1. The highest distances inter CP are in the lateral left ventricle. The anterior left ventricle seems to have the smoothest transition for the inter CP distances, and the lowest values, from ROI 1 till ROI 6. Also the anterior left ventricle tissue is more regular than the other two samples. The inter CP variation of the posterior left ventricle close to endocardium present also a variation, but less pronounced than the lateral left ventricle. In the middle of the posterior left ventricle sample (between ROI 9 and ROI 12), the main tendency of the inter CP distances is to decrease, in contrast with the increasing tendency of the inter CP distances of the anterior left ventricle sample.

The thickest CP are found in the lateral left ventricle (till ROI 13), and the lower values are found for the posterior left ventricle. The difference in values between the anterior ventricle and the posterior left ventricle is around 10 voxels ($35 \mu m$). From ROI 13 till ROI 19, the thicknesses are similar for all 3 samples, all the samples present a significant cleavage planes that cross the tissue. The anterior left ventricles CP thicknesses are close to the lateral left ventricle from ROI 1 till ROI 7, then the values are smaller than the CP thicknesses of the lateral left ventricle and higher than the CP thicknesses of the posterior left ventricle.

4.1.8 Cleavage planes statistics of the sample from slice 2 of the left ventricle - Anterior left ventricle (sample 3, LV_ant_S2_2)

The cleavage planes can be clearly seen throughout the sample (Figure 5.8a). Close to the epicardium, the structure appears more regular, with long parallel CP with ramifications; several artery are visible in ROI 24, 23, 22, 21 and 20 in Figure 4.9c. In the midwall,

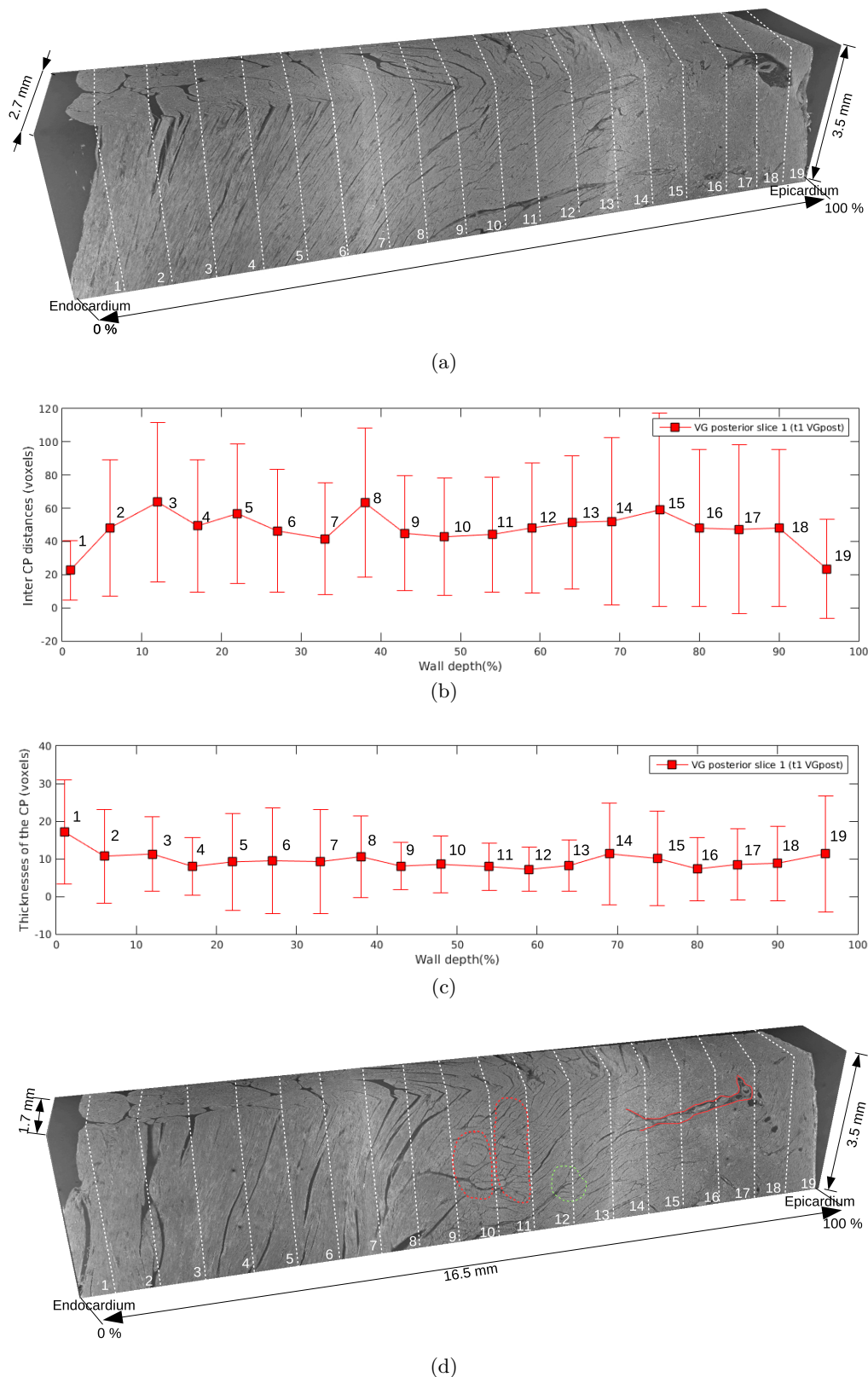


Figure 4.7: a) Posterior left ventricle sample from slice 1 (LV_post_S1_2). b) Inter CP distances and the thicknesses (c) in each of the 19 ROIs. d) The same sample as (a), digitally "cut" narrower to show the inside. Many CP ramifications are highlighted in ROIs 10-13. Several blood vessels are highlighted (red) in ROIs 15-17. We can observe two orthogonal intricate populations of CP in the midwall (ROIs 10 and 11) of the sample.

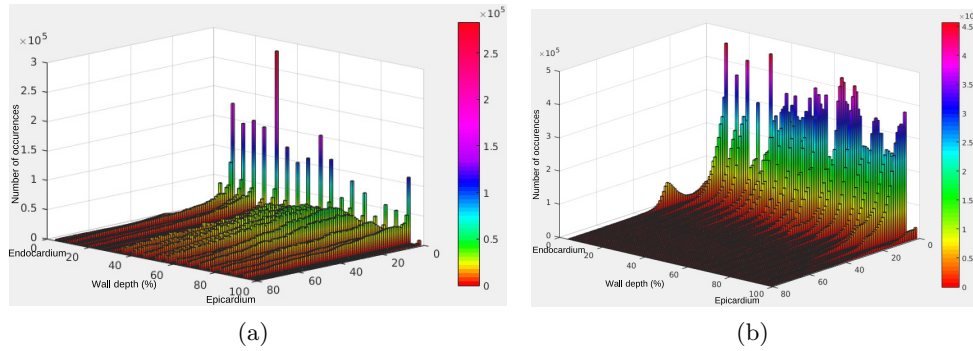


Figure 4.8: *Distribution of inter CP distances (a) and CP thicknesses (b) in the ROIs of the posterior left ventricle sample (LV_post_S1_2) computed for each ROI from the endocardium (wall depth 0%) to the epicardium (wall depth 100%).*

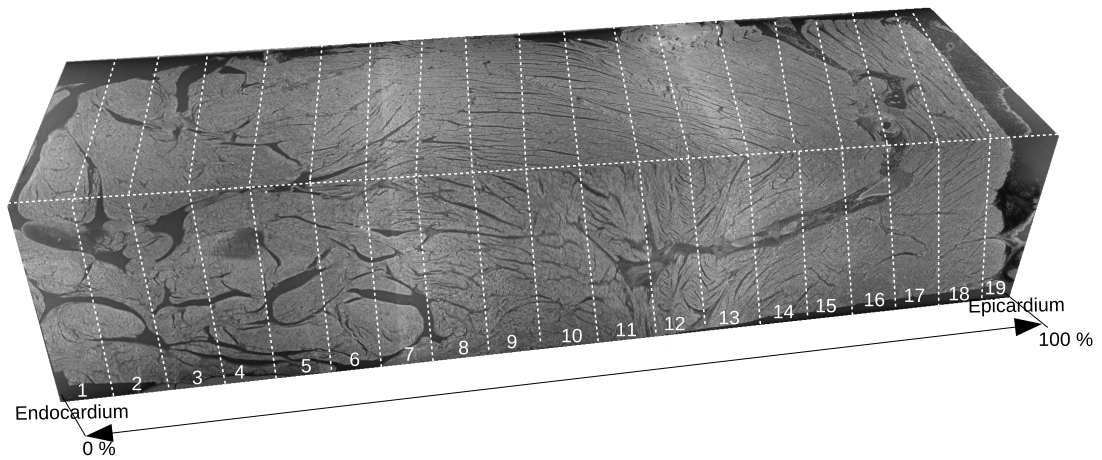
the structure is more fragmented, with shorter cleavage planes with many ramifications. In the ROI 15, 17 and 18, the cleavage planes orientation is changing from a ROI to another. Towards the endocardium, from ROI 1 till ROI 13, in the papillary muscle region, the structure is more irregular.

Excluding ROIs 1, 2 and 25, for which distance and thickness statistics are affected by the large number of voxels that fall outside the sample, the mean distances between cleavage planes from ROI to ROI vary between 32 voxels and 73 voxels ($112-255\mu m$), with standard deviations of around 40-68 voxels ($140-233\mu m$). There is a tendency for distances to be greater from ROI 3 till ROI 13. From ROI 14 till ROI 16, the distances inter CP are decreasing, then the distances are increasing till ROI 18. ROI 15 and ROI 19 have a principal direction diametrically opposed. The distances variation change from ROI 19, till the end of the structure. A large distance is obtained for ROI 20. The CP for ROI 20 are not very evident, also a significant cleavage plane is present.

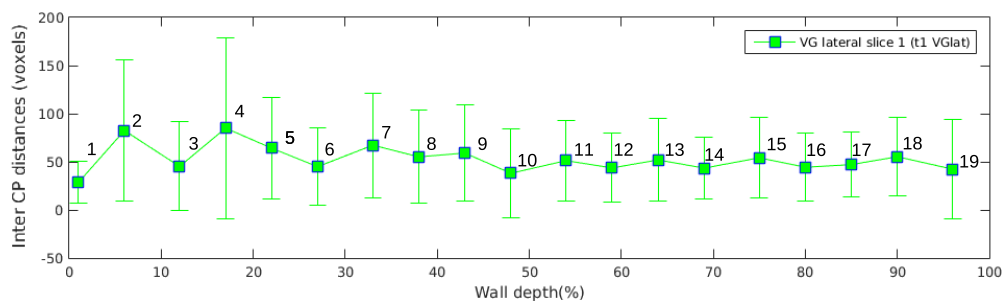
As for the mean cleavage plane thicknesses, again excluding the two extreme ROIs on each side, the means are between 7-18 voxels ($24.5-63\mu m$), slightly greater in ROIs 5, 8 and 9 because of the large distance between groups of myocytes. The variances are also greater in these ROIs, because we still have small cleavage planes, as well as large ones. The distances and thicknesses histograms for each of the 25 ROIs are plotted in Figure 4.12. For distances, histograms for ROIs 1-24 are relatively similar. The thickness histograms appear more or less similar, with the exception of the outermost ROIs which have too many voxels outside the sample.

4.1.9 Comparison between different anterior left ventricle samples from 2 hearts (samples 1, 3 and 4)

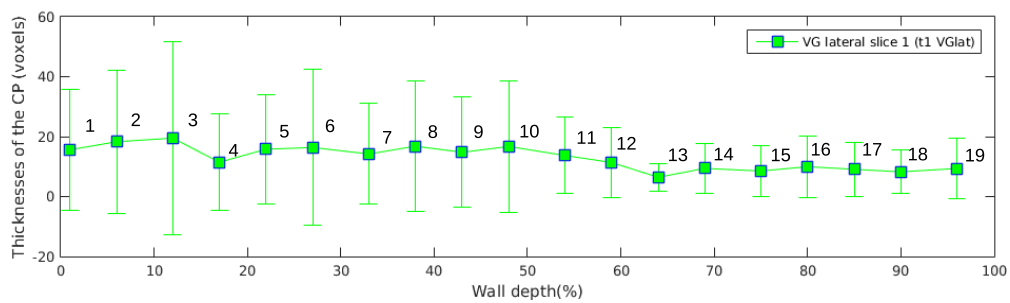
In Figure 4.13 the inter-CP mean distances for the anterior left ventricle from 3 different samples and 2 hearts are presented. The inter cleavage planes distances for the ROI corresponding to the wall depth ranging from 18% to 32% starting from endocardium are very similar for all 3 samples: it is around 50 voxels. From 32% depth from endocardium,



(a)



(b)



(c)

Figure 4.9: a) Lateral left ventricle sample from slice 1 (*LV_lat_S1_2*), b) Inter-CP distances in each of the 19 ROIs. c) Thicknesses of the CP in each of the 19 ROIs.

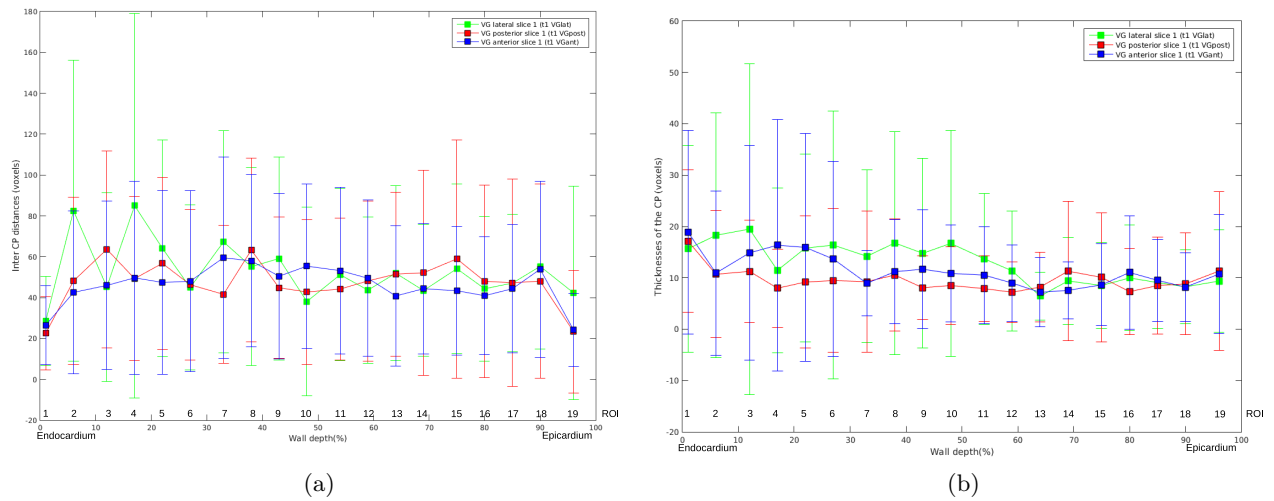
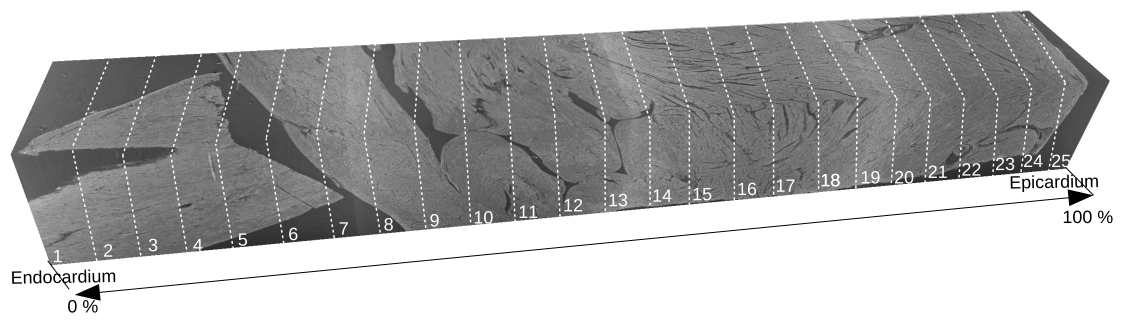


Figure 4.10: *Inter-CP distances and (b) CP thicknesses of the lateral, posterior and anterior samples of the left ventricle from slice 1.*

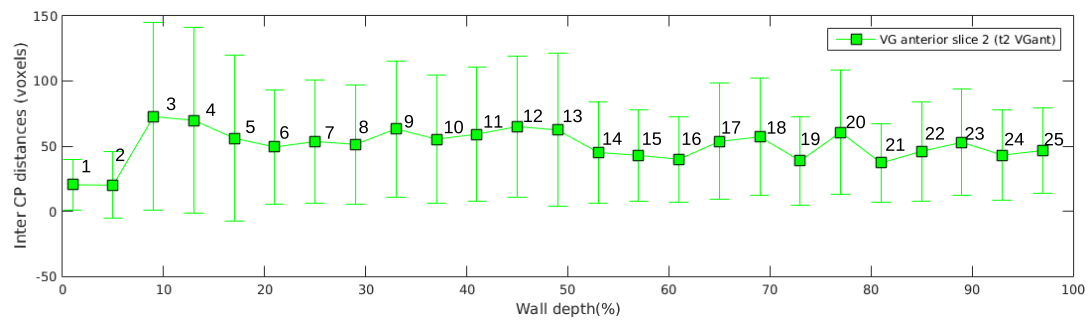
till epicardium, the distances of the cleavage planes in the 3 samples differ by around 10 voxels. The anterior left ventricle from slice 1 and slice 5 seems to be similar in CP distances between a wall depth of 48% and 82% from endocardium.

In Figure 4.13 are presented the thicknesses of all 3 samples of anterior left ventricle from different slices, and 2 different hearts. The CP thicknesses are very different from all 3 samples from endocardium till 38% from endocardium. The variation are also different for all 3 samples. The anterior left ventricle from slice 2 has the most irregular variation of the CP thicknesses, contrary to the other 2 samples that have a progressive increasing/decreasing of the CP thicknesses values. The anterior left ventricle CP thicknesses of the slice 1, has an increasing value till 18 voxels and then a decreasing till 8 voxels. Contrary, the anterior left ventricle from slice 5, heart 2, the thicknesses have a smooth increasing values from endocardium till 35% depth from endocardium. The CP thicknesses values are very similar for anterior left ventricle from slice 1 and slice 2, for the same heart, from 38% depth from endocardium, till epicardium. Also, from 62% from endocardium, the 3 samples seem to have similar values of the CP thicknesses. All the 3 samples have an increasing thicknesses mean value close to the epicardium. As it is presented below, all the 3 samples, present important cleavage planes close to the epicardium.

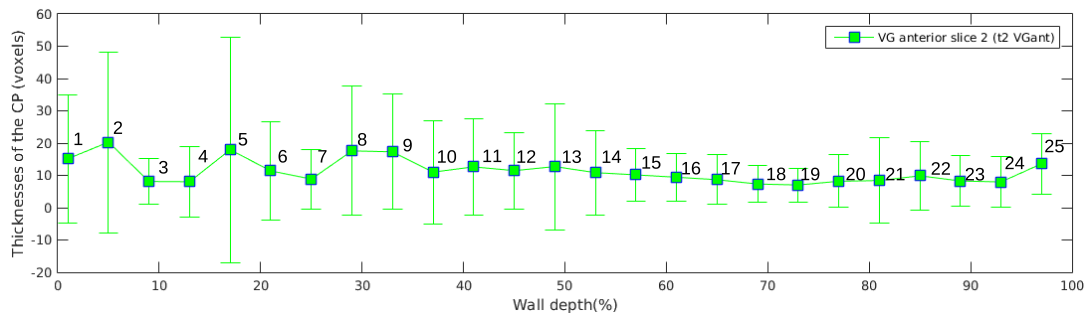
In conclusion, the CP thicknesses of all the 3 samples are similar from midwall till epicardium. The high difference is close to endocardium, were the structure is very differently organised. The inter CP distances for all 3 samples are slightly different in some regions, the variation of the CP distances is also different, still are regions were the distances are equal for all 3 samples. The anterior left ventricle from slice 5 and slice 1 from 2 different hearts seems to have more similar distances values. The structure of the 3 samples from left ventricle are very different in texture organisation, as can be seen in the Figure 4.12, Figure 4.6a, and Figure 4.2a. Even for the 2 samples from the same heart presented in



(a)

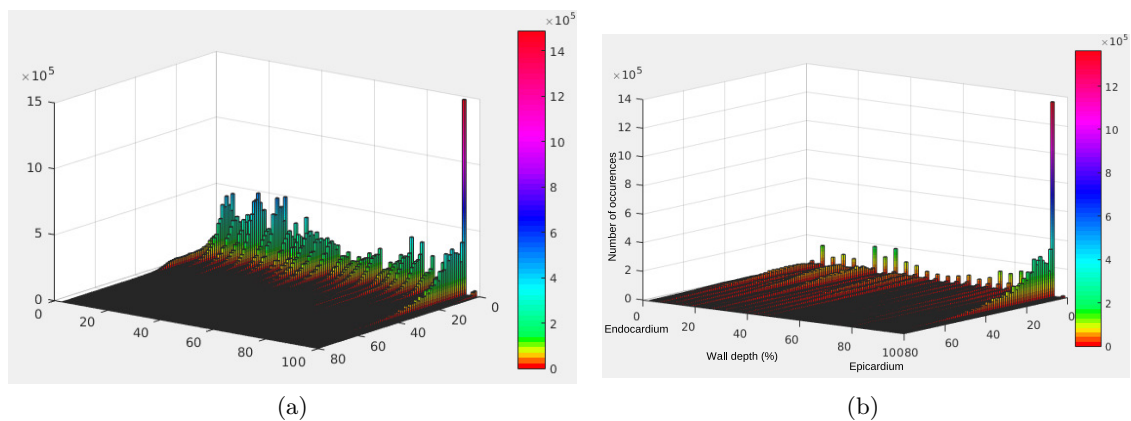


(b)



(c)

Figure 4.11: a) Anterior left ventricle sample from slice 2 (*LV_ant_S2_2*), b) inter-CP distances and (c) thicknesses of the CP in each of the 25 ROIs.



(a)

(b)

Figure 4.12: Distribution of the inter-CP distances (a) and CP thicknesses (b) distribution in the ROIs of the anterior left ventricle sample (*LV_ant_S2_2*) computed for each ROI from the endocardium (wall depth 0%) to the epicardium (wall depth 100%).

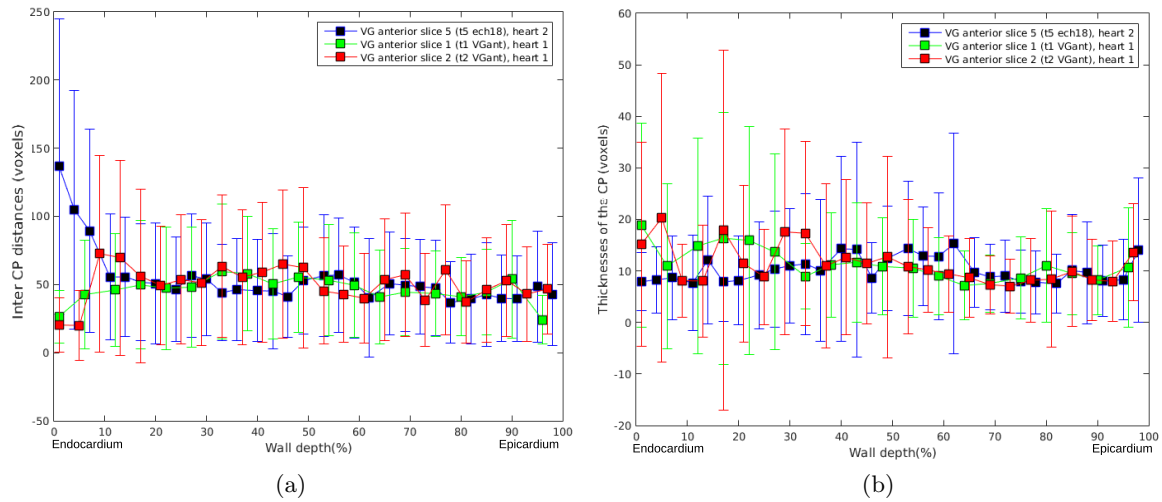


Figure 4.13: *a) Inter-CP distances and b) CP thicknesses of the anterior left ventricle from sample 1, 2 and 5 from 2 different hearts.*

Figure 4.12 and Figure 4.6a , situated one above the other, the structure is very different.

4.1.10 Cleavage planes statistics of the posterior septum (sample 8, S_post_S1_2)

The cleavage planes can be clearly seen throughout the sample (Figure 4.14). From ROI 1 till ROI 14, the structure appears more fragmented but regular, with long cleavage planes with many ramifications; several arteries and veins are visible. The myocytes are more tightly packed in small groups, separated by large, curved or straight cleavage planes. From ROI 15, the texture is changing, the long cleavage planes are less, the cleavage planes are shorter, the structure is irregular. Several arteries and veins are visible. Towards the endocardium, Excluding ROIs 1, and 23, for which distance and thickness statistics are affected by the large number of voxels that fall outside the sample, the mean distances between cleavage planes from ROI to ROI varies between 38 voxels and 90 voxels ($133-315 \mu m$), with standard deviations of around 30-80 voxels ($105-280 \mu m$). There is a tendency for distances to increase from ROI 6 till ROI 10, then to decrease till ROI 17. An explication for the inter CP the jump of cleavage plane distance for ROI 14, is the existence of the 2 main orientations from a significant CP.

As for the mean cleavage plane thicknesses, again excluding the two extreme ROIs on each side, the means are between 7-20 voxels ($24.5-70 \mu m$), the main tendency is for the thicknesses to increase as we move to the middle of the sample then to decrease. The variances are also greater in these ROIs, because we still have small cleavage planes, as well as large ones.

The distances and thicknesses histograms for each of the 23 ROIs are plotted in (Figure 4.14d and Figure 4.14e). For distances, histograms are different, with ROIs 1-4 and

ROI 18-22 having somewhat larger distances. The thickness histograms appear more or less similar, with the exception of the outermost ROIs which have too many voxels outside the sample.

4.1.11 Cleavage planes statistics of the anterior septum (sample 7, S_ant_S1_2)

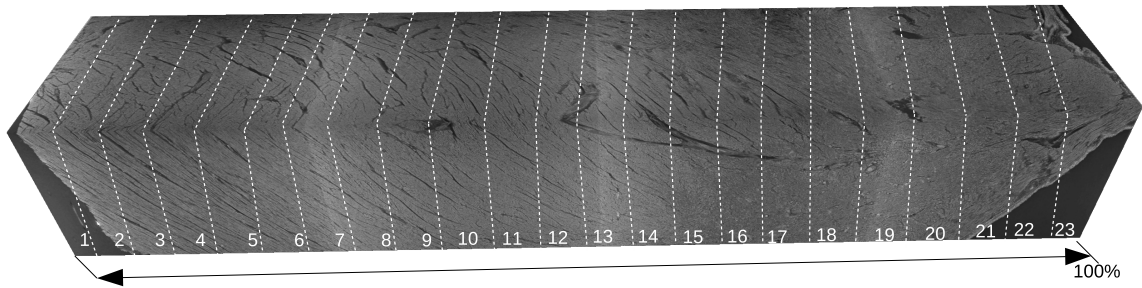
As can be seen in Figure 4.15, the structure is irregular. It cannot be distinguished a special pater, like in the case of posterior septum. The cleavage planes are in general very fine/tiny, but also important cleavage planes that change their orientation are present. The sample was split in 22 ROI. Taking into account that the last 2-3 ROIs contain only one large cleavage plane, only the first 20 ROIs are automatically analysed. The results are presented in Figure 4.15b and Figure 4.15c.

The main tendency of the distances inter cleavage planes from ROI 2 till ROI 8 is to decrease from 105 voxels at 58 voxels ($367 - 203 \mu m$). For ROI 10, the smallest inter CP distance value is registered, of 33 voxels ($115 \mu m$), then the distances inter CP are increasing again till 72 voxels ($252 \mu m$). One main reason of the increasing of the inter CP distances, is the bifurcation and the banding of the cleavage planes. Then the inter CP distances decrease till 25 voxels ($87 \mu m$) for ROI 20. The SD is also high from ROI 2 till ROI 4, around 90 voxels, then the SD for the rest of ROIs is around 40-70 voxels. The thicknesses of the CP are around 7-10 voxels for ROI 2 till ROI 15. The SD is around 6-8 voxels, for most of the ROIs with some exceptions: ROI 5, 6 and 10. That means that there are also thick CPs. The CP thicknesses increase from 9 voxels till 16 voxels from ROI 15 till ROI 20. A network of thick cleavage planes cross those ROIs, as can be seen also in Figure A.8.

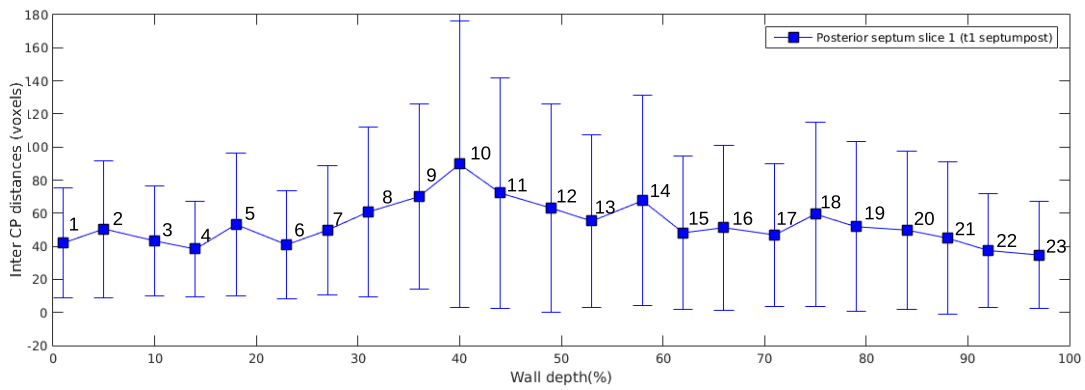
4.1.12 Cleavage planes statistics of the antero-posterior septum (sample 9, S_antposta_S2_2)

The cleavage planes in the sample presented in Figure 4.16a can be observed easily. The cleavage planes orientation of the ROI 1 till ROI 11 seems to have a direction perpendicular on the direction of the cleavage planes from ROI 16 till ROI 26. Between ROI 11 and ROI 16, the cleavage planes seems to be slightly curved. The structure is fragmented, the inter CP distances vary a lot in all the sample. As can be seen in Figure 4.16a and the statistics results from Figure 4.16c, the cleavage planes distances for the first 13 ROIs present a high variation, from 37 to 75 voxels ($130-262 \mu m$), with standard deviations of around 33-72 voxels. From ROI 13, the inter CP distances have a slow variation, between 27 - 49 voxels ($95-172 \mu m$), with standard deviations of around 21-47 voxels. The variances are also greater in these ROIs, because we still have small cleavage planes, as well as large ones.

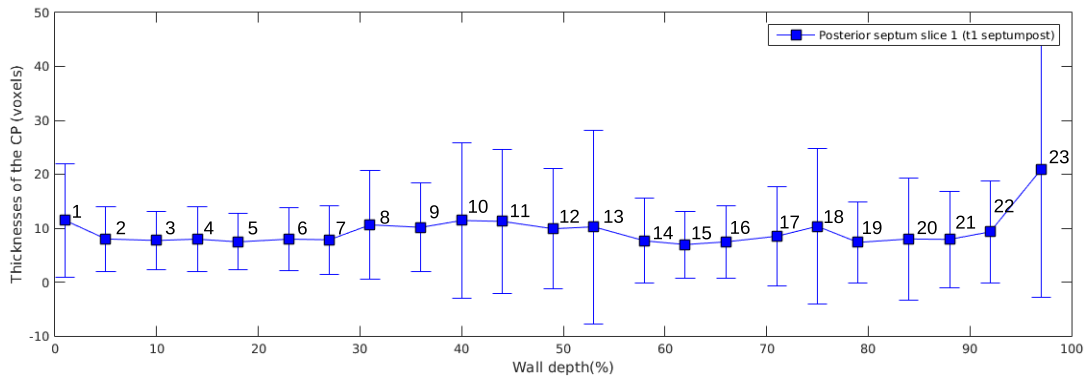
As for the mean cleavage plane thicknesses, for the first 10 ROIs the means are almost constant around 9-10 voxels ($32-35 \mu m$), with a variance of 9-10 voxels. The mean thick-



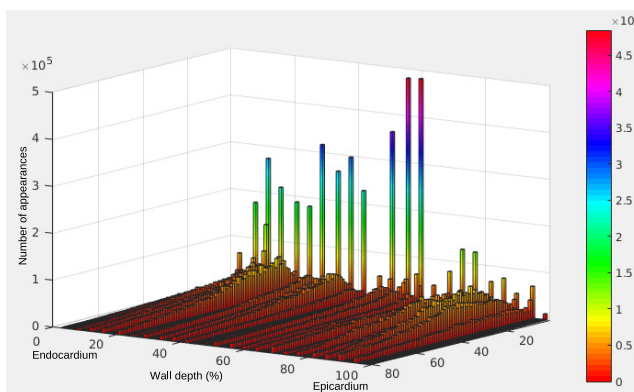
(a)



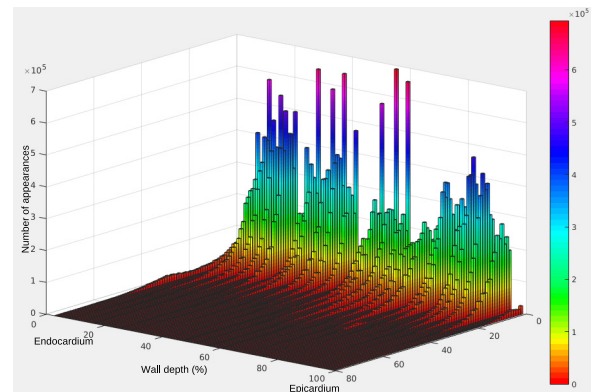
(b)



(c)

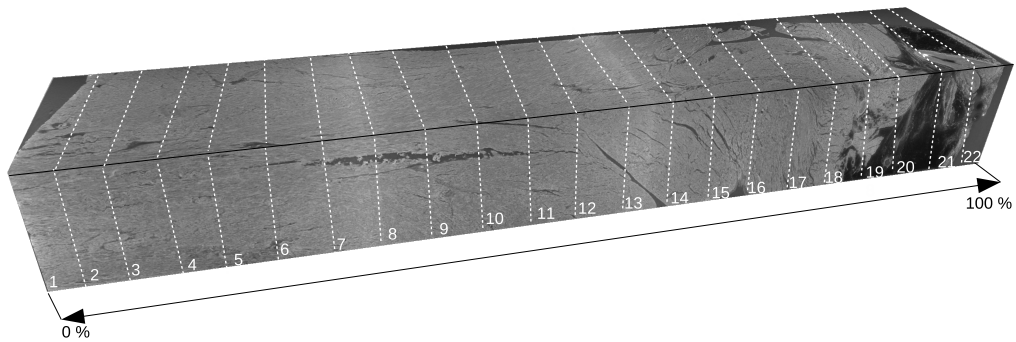


(d)

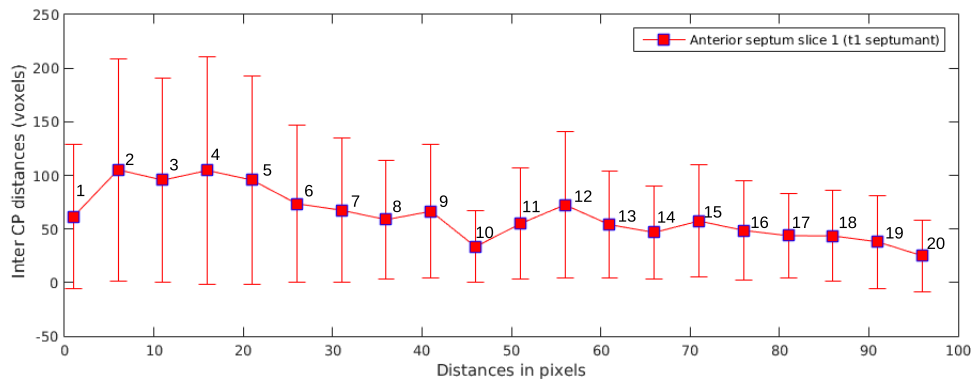


(e)

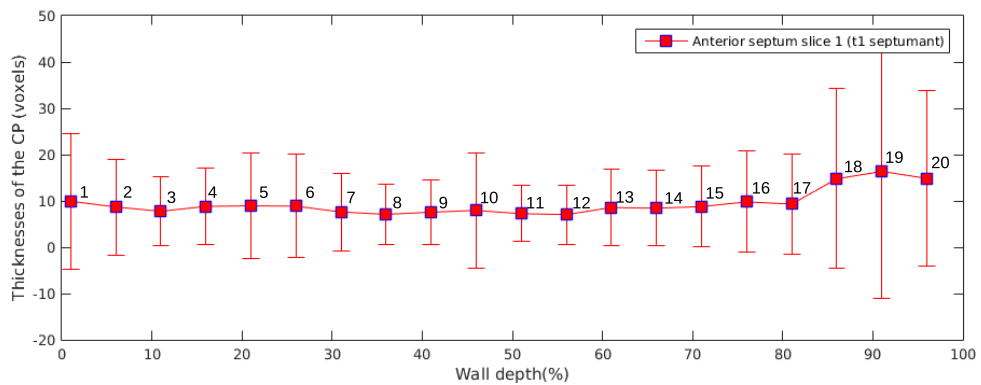
Figure 4.14: a) Sample extracted from the posterior septum from slice 1 ($S_{post_S1_2}$), b) Inter-CP distances and c) thicknesses of CP in each of the 23 ROI. d) Inter-CP distances, and CP thicknesses (e) distribution



(a)



(b)



(c)

Figure 4.15: a) Sample extracted from the anterior septum, slice 1 ($S_{ant_S1_2}$), b) Inter-CP distances computed for each of the 20 ROIs (average values and standard deviations) and c) Thicknesses of the CP computed for each of the 20 ROIs (average values and standard deviations).

nesses are higher for ROI 11 and 12, around 11 voxels with a variance of 15 voxels. In the middle of the sample, from ROI 13 till ROI 21 the thicknesses are between 7-9 voxels (24-31 μm), with standard deviation between 7-10 voxels. Between ROI 19 and ROI 26 a significant cleavage plane is present, that makes the thickness mean values to increase till 12 voxels. The presence of the pericardium in the last 3 ROIs, helps to increase the mean thickness values.

The distances and thicknesses histograms for each of the 19 ROIs are plotted in Figure 4.17. For distances, histograms for are relatively similar, with ROI 4 and 8 having more smaller distances between CP . The thickness histograms appear more or less similar.

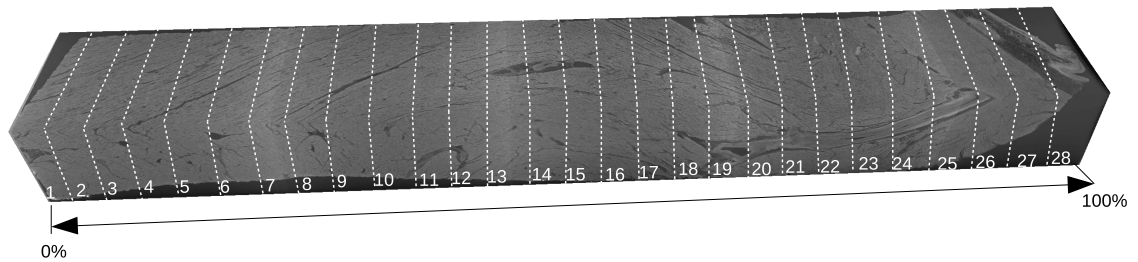
4.1.13 Cleavage planes statistics of the antero-posterior septum (sample 10, S_antpostb_S2_2)

The cleavage planes are parallel and have a main tendency to curve. The distances inter CP are between 33 and 68 voxels (115 - 238 μm). Excluding ROIs 1, 2, and 27, for which distance and thickness statistics are affected by the large number of voxels that fall outside the sample. The texture is not the same in all the sample. From ROI 6 till ROI 16, the inter cleavage planes distance is almost constant around 40-45 voxels (140 - 157 μm), with a standard deviation between 34 - 50 voxels (119 - 175 μm). From ROI 16, the cleavage planes become less evident, the sample texture is changing. The inter CP distance is increasing from ROI 16 till ROI 19 at 68 voxels (66 - 238 μm), also the standard deviation is increasing from 50 for ROI 17 till 68 voxels (238 μm) for ROI 19. Then the distance inter CP is decreasing till 20 voxels (70 μm) for ROI 21. The cleavage planes are less evident. Close to the pericardium, from ROI 22 till ROI 27 the CP distance are high, around 42 - 58 voxels (147 - 203 μm).

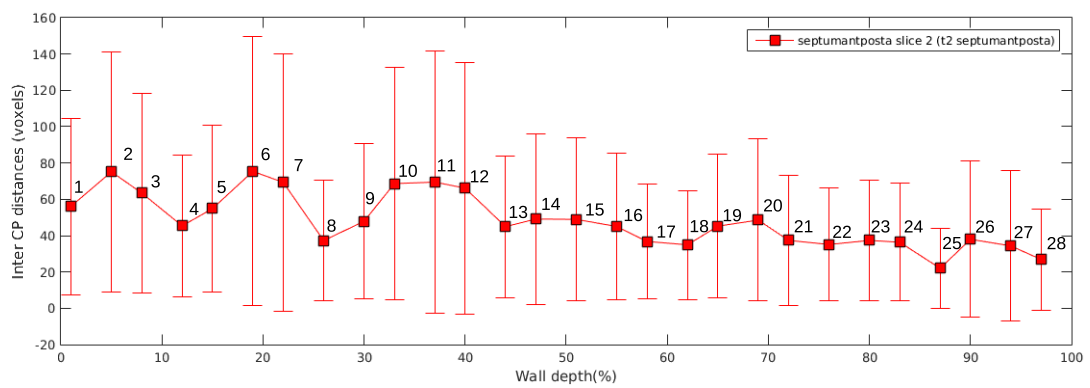
The CP thicknesses are between 8 and 10 voxels (28-35 μm) for ROI from 4 to 19 with a standard deviation of 6 - 11 voxels. For ROI 11 and 12 the CP thicknesses is increasing. Also from ROI 19 till ROI 37, the cleavage planes thicknesses is higher, around 8 and 12 voxels.

4.1.14 Comparation between the septum samples (samples 7, 8 and samples 9, 10)

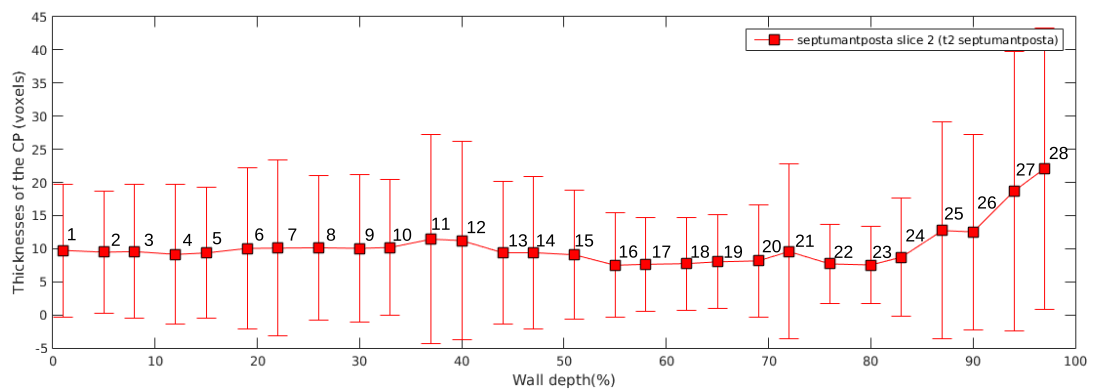
Anterior and posterior samples The inter cleavage planes distances of the anterior and posterior samples for the ROI corresponding to the wall depth ranging from 50% to 100% are very similar (Figure 4.19). The posterior septum inter cleavage planes distances are higher than the inter cleavage planes distances of the anterior septum for the wall depth ranging from 0% to 30%. The CP thicknesses values are similar from wall depth of 0% till 75% with slightly thicknesses values increasing for posterior septum between the wall depth of 30% to 50%.



(a)



(b)



(c)

Figure 4.16: a) Sample extracted from the anterior-posterior septum, slice 2 ($S_{antposta_S2_2}$), b) Inter-CP distances computed for each of the 28 ROIs (average values and standard deviations) and c) Thicknesses of the CP computed for each of the 28 ROIs (average values and standard deviations).

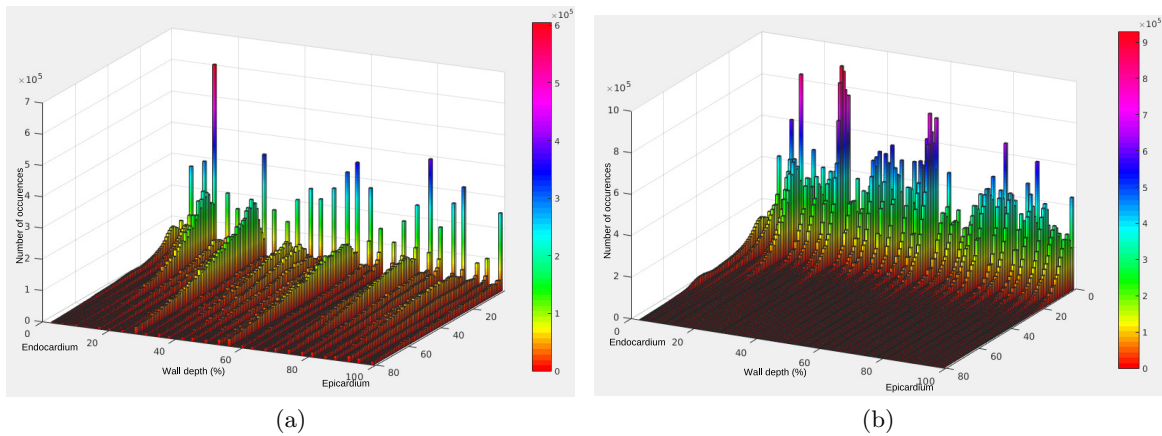
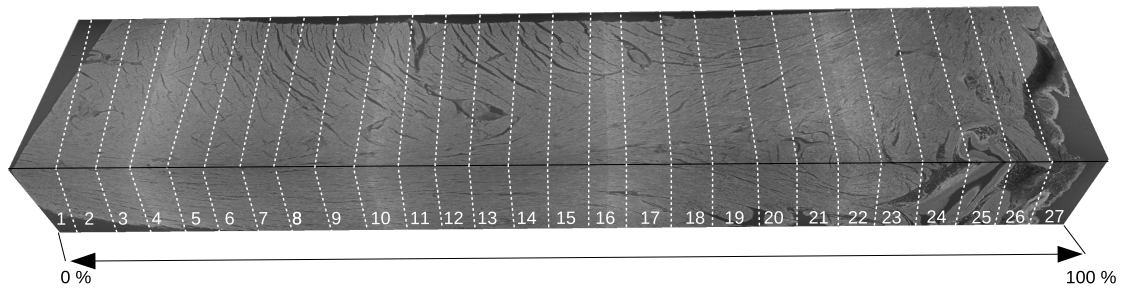


Figure 4.17: *a) Distribution of the Inter-CP distances and CP thicknesses (b) distribution of the anterior-posterior septum from slice 2 ($S_{antposta_S2_2}$) computed for each ROI from the endocardium (wall depth 0% at the endocardium to 100% at the epicardium).*

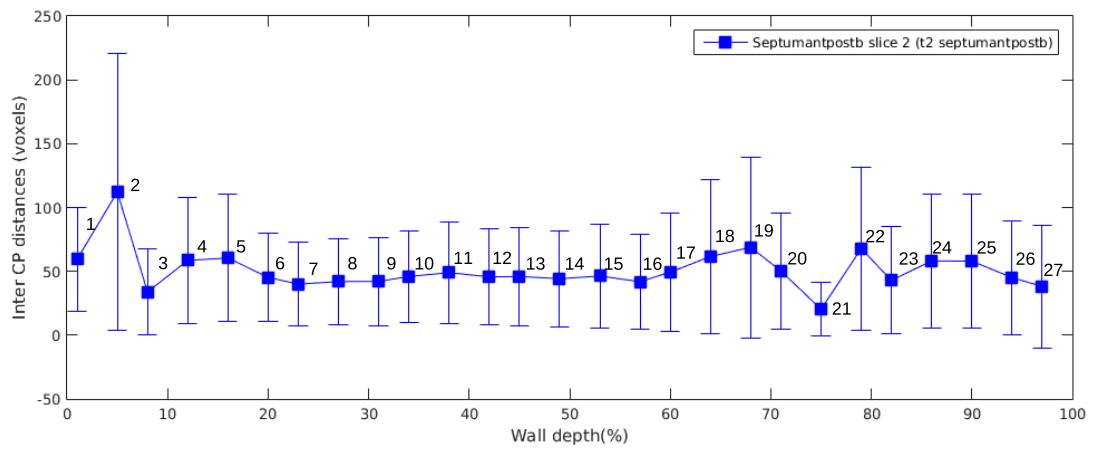
Antero-posterior samples If we compare the septumantposta sample with septumantpostb sample Figure 4.20, we notice that the thicknesses of the two samples are almost the same till 75% from the pericardium. The SD is higher for the septumantposta than the septumantpostb sample. The inter CP distances are higher for septumantposta sample, one reason is the irregularity of the texture. In the middle of the samples, the inter CP distances are almost equal. Close to the pericardium the inter CP distances vary a lot.

4.2 Conclusion

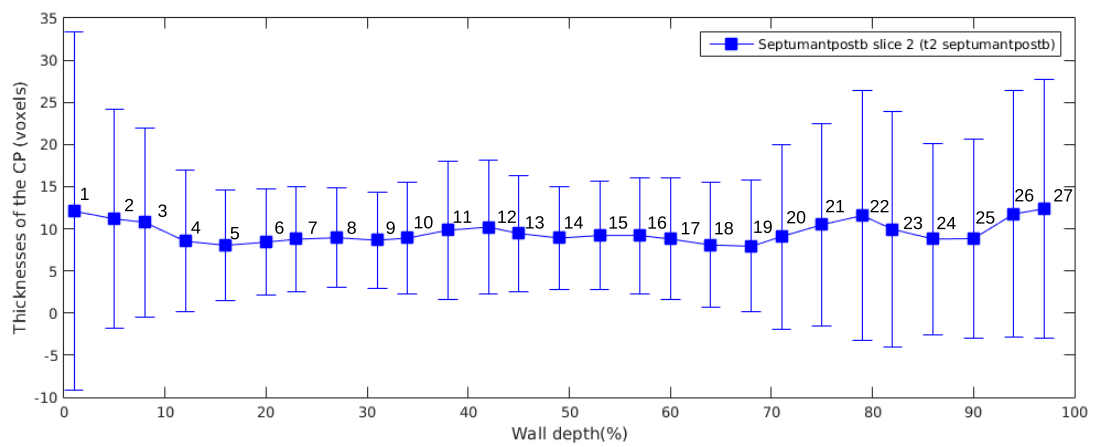
The quantitative data that we extracted show that the thickness of cleavage planes varies roughly between $24 \mu m$ and $59 \mu m$ and that the distance between successive cleavage planes varies approximately between $120 \mu m$ and $280 \mu m$, with significant local variations of the standard deviation. The anterior left ventricle samples from 2 different hearts, from three different regions was compared. The CP thicknesses of all the 3 samples of the anterior left ventricle from 2 human hearts are similar from midwall till epicardium, with high difference close to the endocardium. The inter CP distances for all 3 samples are slightly different in some regions, the variation of the CP distances is also different, still are regions where the distances are equal for all 3 samples. The CP thicknesses and the inter-CP distances of the anterior, posterior and lateral left ventricle from sample 1, from the same heart, are in general different, with some regions with similar values. The anterior and posterior septum inter-CP distance are similar from midwall till 100% wall depth. The CP's thicknesses are very similar for anterior and posterior septum, also for the septumantposta and septumantpostb.



(a)



(b)



(c)

Figure 4.18: a) Sample extracted from the septumantpostb, slice 2 ($S_{\text{antpostb}}S2_2$), b) Inter-CP distances computed for each of the 27 ROIs.

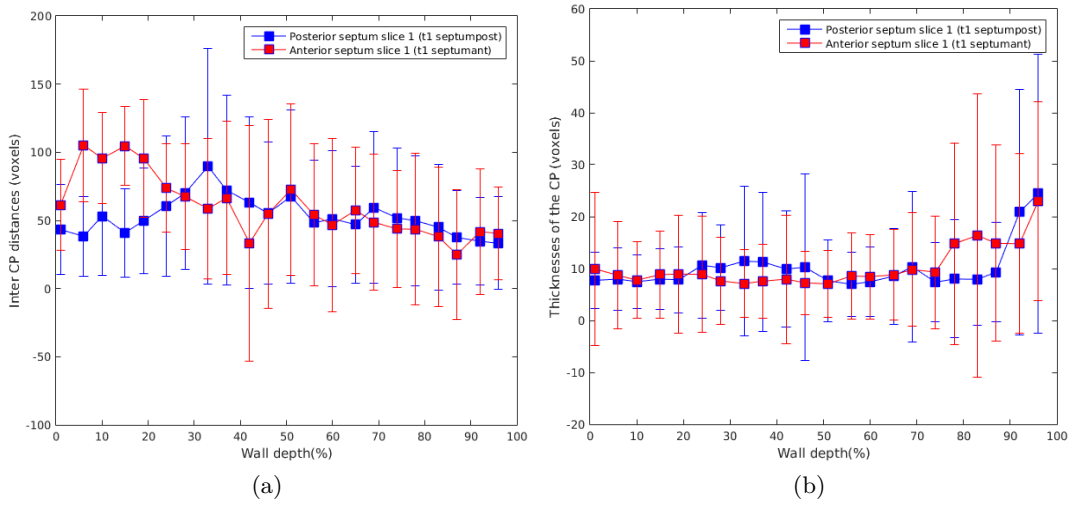


Figure 4.19: *a) Inter-CP distances and b) CP thicknesses of the posterior and anterior samples.*

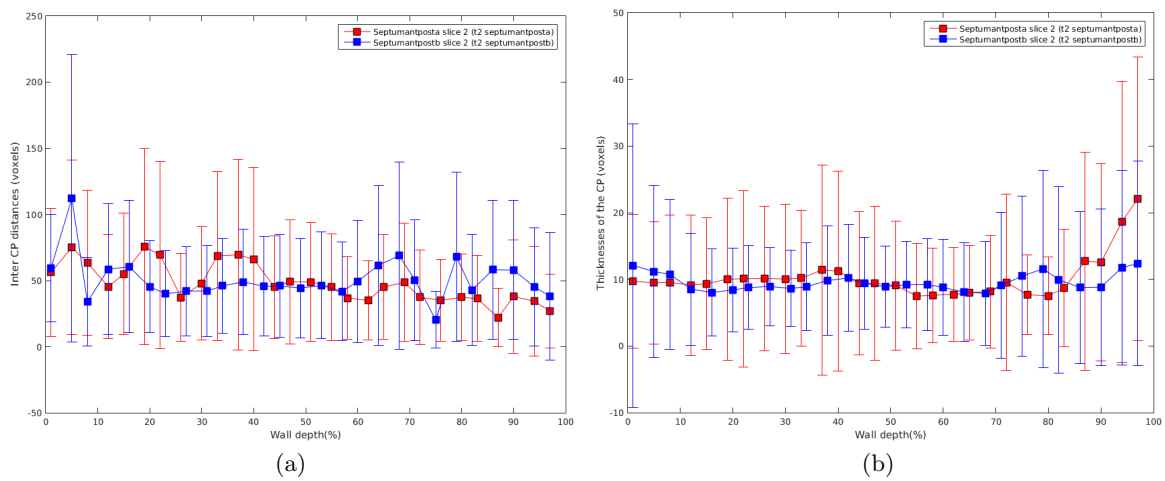


Figure 4.20: *a) Inter-CP distances and b) CP thicknesses of the antero-posterior samples.*

General conclusion and perspectives

The aim of this thesis is to investigate the 3D microscopic structure of *ex-vivo* human cardiac muscle. To overcome the limitations of the 3D imaging techniques such as DMRI or CT, we employed X-ray phase contrast μ -CT, developed at the European Synchrotron Radiation Facility (ESRF). Then tissue samples from the left ventricle and septum of normal fresh hearts were prepared, imaged and reconstructed in 3D at an isotropic resolution of $3.5 \mu\text{m}$. The obtained volumes were compared with 2D histological examinations, which served as a basis for interpreting their content and identifying the tissue components.

Our experiments showed that 3D X-ray phase-contrast μ -CT is a viable technique for *ex-vivo* investigation of the 3D arrangement of myocytes at a microscopic level, allowing a better understanding of the 3D cardiac tissue micro-architecture. For the first time, it was possible to observe the 3D arrangement of the various components such as the myocytes, capillaries and the extra-cellular matrix, from the epicardium to the endocardium, at a scale ranging between a few μm to 1 cm. We made a descriptive analysis of three samples from the posterior left ventricle and from the anterior and posterior septum. Visualizing data volumes of several tens of GB in size was not possible with conventional software, therefore we resorted to either displaying small parts of the samples at full resolution, or the entire samples at a lower resolution.

Then, we focused on the analysis of the extracellular matrix, specifically on the cleavage planes (CP). We developed an image processing protocol to automatically extract the cleavage planes and compute statistics on their thickness and on the distance separating them in 3D. The computation method was based on the fact that the cleavage planes are locally parallel and have a privileged 3D orientation. We demonstrated that the proposed method was efficient to clearly reveal the cleavage planes present within the myocardium and to quantify new biomarkers such as the thickness and the inter-CP distances.

We showed that these two structural descriptors did not vary much when crossing the LV wall from the epicardium to the endocardium within the same transmural sample, but that they could vary significantly between samples of the septum and of the anterior and posterior left ventricle. We have also confirmed the existence of two quasi-orthogonal populations of cleavage planes in certain regions of the left ventricle (previously reported in the literature), whose role in the cardiac biomechanics is certainly primary. Lastly,

the quantitative statistical data that we extracted show that the thickness of CP roughly varies between $24 \mu m$ and $59 \mu m$ and that the distance inter-CP approximately varies between $70 \mu m$ and $280 \mu m$, with significant local variations of the standard deviation.

In the future, we plan to extract more detailed biomarkers corresponding to the perimysium in order to better understand diseases caused by anomalies in the cleavage planes. This will imply extracting more detailed cleavage plane orientation measurements, not just of the average orientation within a subvolume, but going to the orientations of individual cleavage planes or even to local orientations in *regions* of the cleavage plane. In addition to the orientation, cleavage plane interconnections and ramification can also be an interesting information, as well as biomarkers for other tissue elements, such as the dimensions, density and orientations of myocytes. A particularly interesting aspect, if suitable samples can be acquired, would be to compare similar regions from a normal heart and from pathological cases. Both a visual comparison as well as a comparison of biomarkers could help to better understand the 3D structural modifications that appear in the case of cardiac diseases such as hypertrophic cardiomyopathy or other conditions that can lead to cardiac arrest.

Another interesting research topic would be a comparison of biomarkers extracted at different scales from X-ray PCI with those extracted from MRI, ideally on the same heart sample. This would potentially allow us to get a better understanding of what is seen in lower-resolution MRIs and in the future make better hypotheses about the microscopic structure of the heart and potential cardiac illnesses based on *in-vivo* MRI images.

Appendix

Appendix A

3D X-ray Phase Contrast μ -CT images

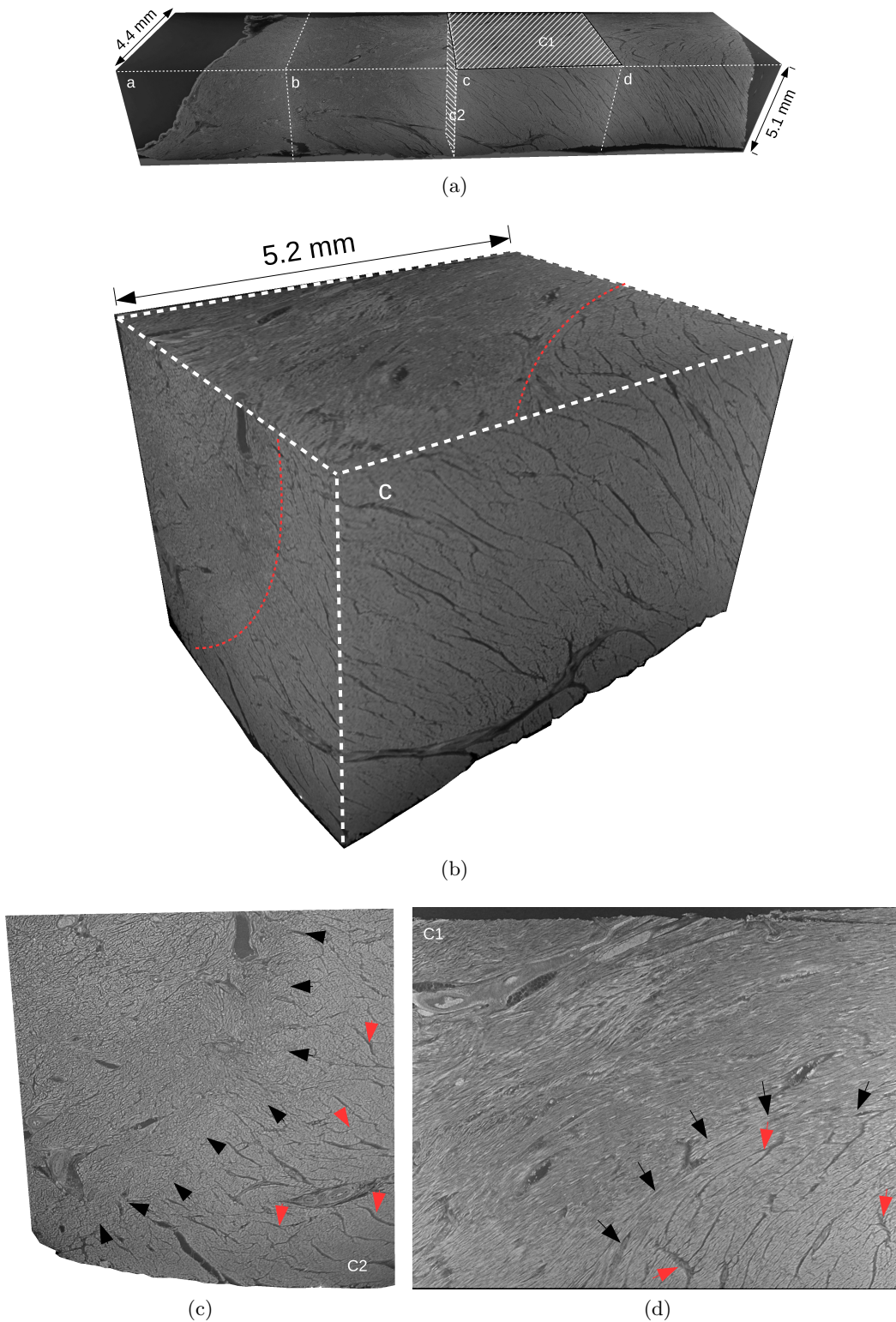


Figure A.1: Zoom-in on subvolume (c) of the posterior septum sample from Figure 2.8. The red dashed lines mark the transition from the left ventricle (more fragmented by cleavage planes) to the right ventricle. Zoom-in on two orthogonal sections through the posterior septum sample from Figure 2.8, the top and left faces of the parallelepiped from Figure A.1. Each of these sections shows two organisation patterns, one corresponding to the left ventricle and the other to the right ventricle. The approximate separation between patterns is indicated by the black arrows. Some cleavage planes are marked by red arrows.

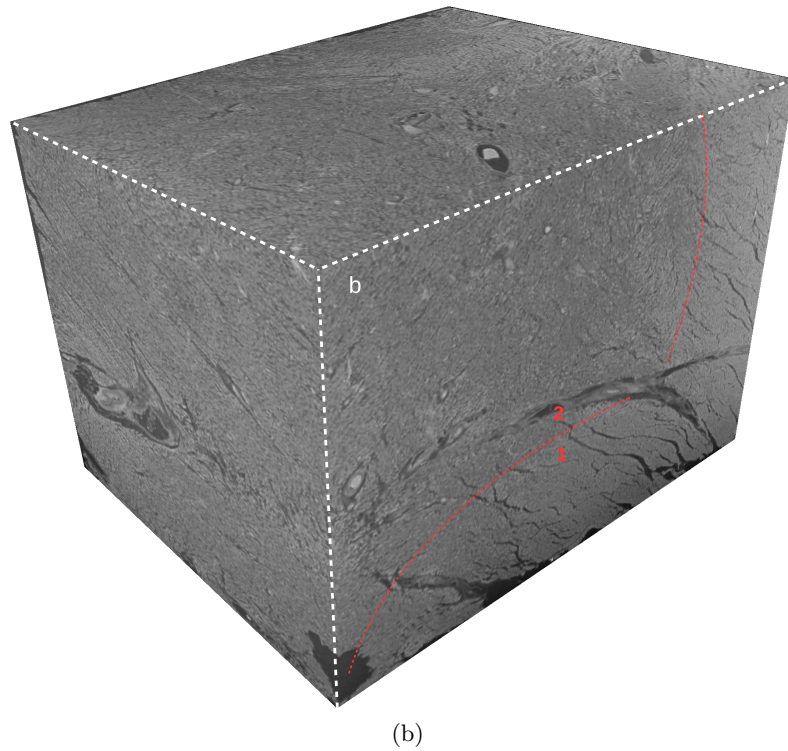
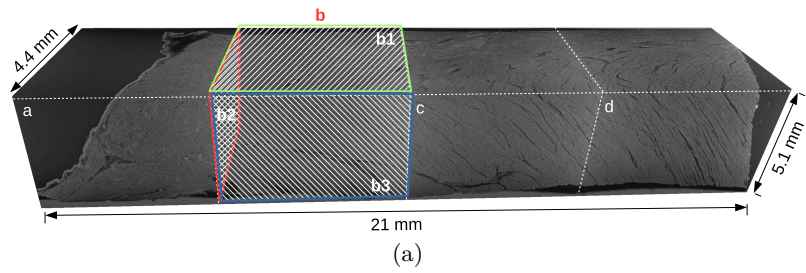


Figure A.2: *Zoom-in on the subsample marked (b) of the posterior septum sample from Figure 2.8. The red dashed line marks the approximate separation between the left and right ventricles.*

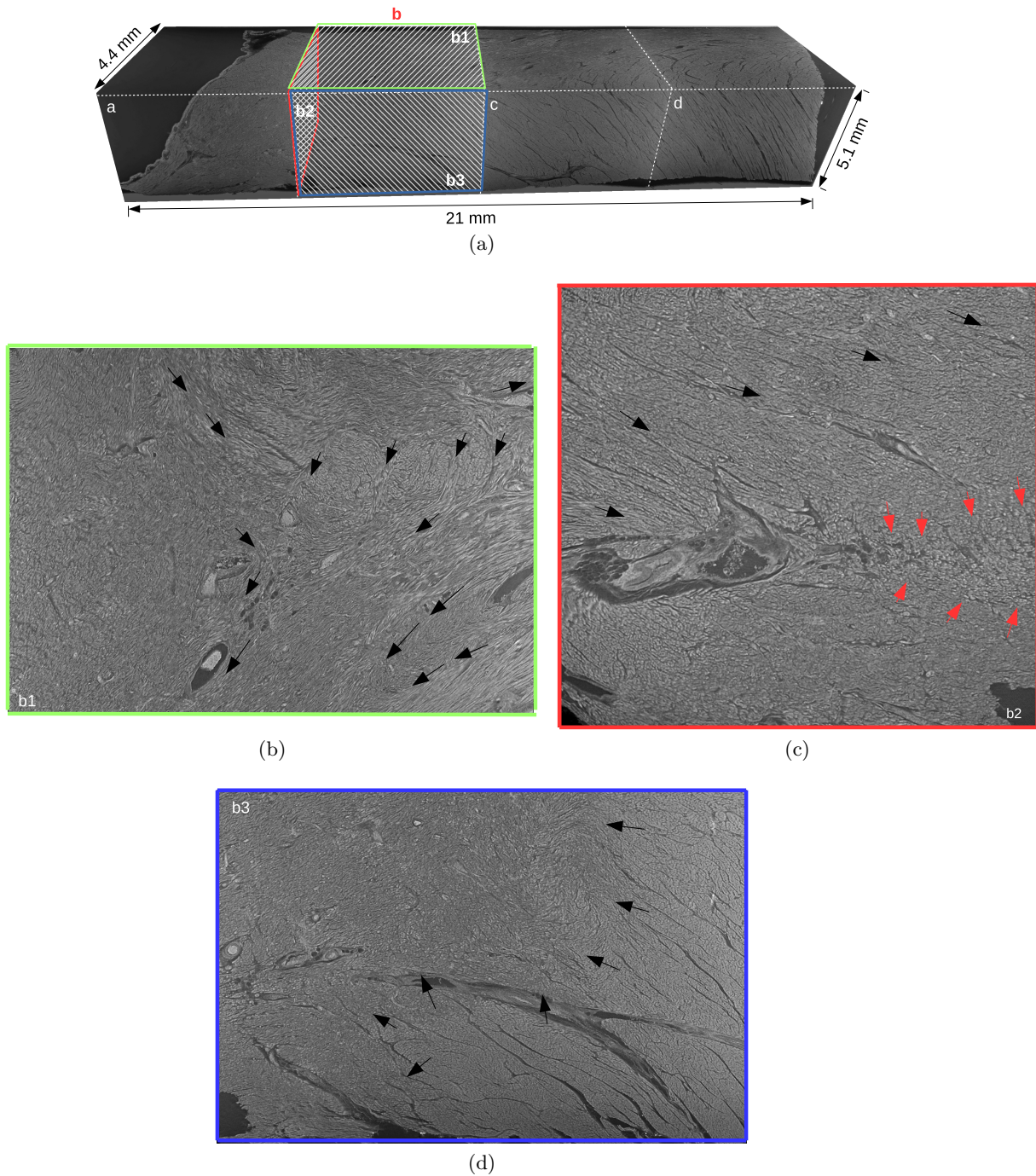


Figure A.3: a) Zoom-in on the top face of subsample (b) of the posterior septum sample from Figure 2.8. As opposed to subsamples (c) and (d), we can now see abrupt changes in the orientation of myocytes (black arrows mark the changes). b) Zoom-in on the left face of subsample (b) of the posterior septum sample from Figure 2.8. Myocytes keep their orientations (black arrows). The cleavages planes are thin. The myocytes (red arrows) change their orientation in the neighborhood of the transversally-cut cleavage plane, in which several blood vessels and adipose cells can be seen. Zoom-in on the front face of subsample (b) of the posterior septum sample from Figure 2.8. This section shows two organisation patterns, one corresponding to the left ventricle and the other to the right ventricle. The approximate separation between patterns is indicated by the black arrows.

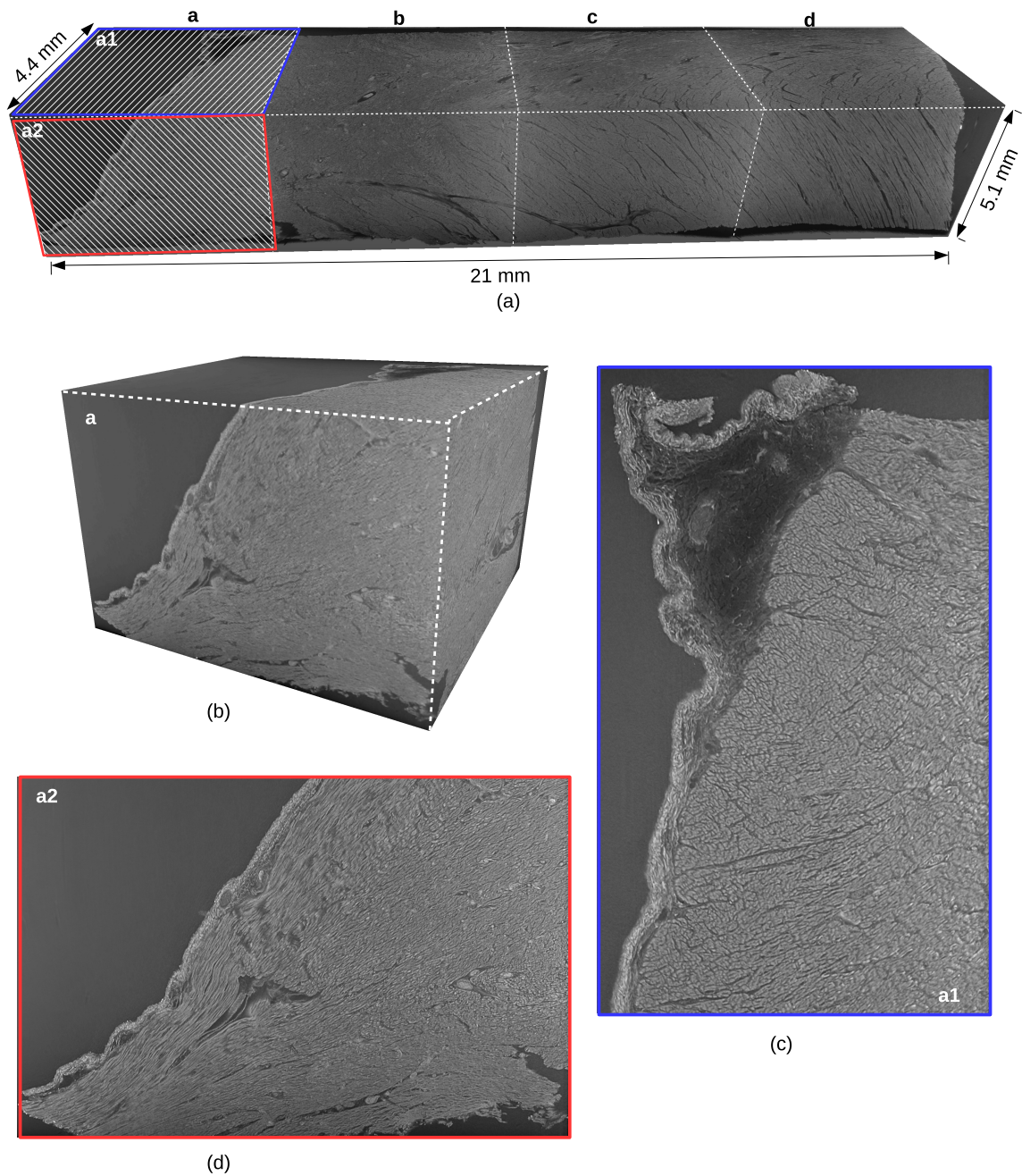


Figure A.4: *Zoom-in on the cube marked (a) of the posterior septum sample shown in Figure 2.8. Zoom-in on the top and front faces of subsample (a) of the posterior septum sample from Figure 2.8. The myocytes are very dense and thin cleavage planes can be seen. The pericardium can also be seen at the edge of the tissue.*

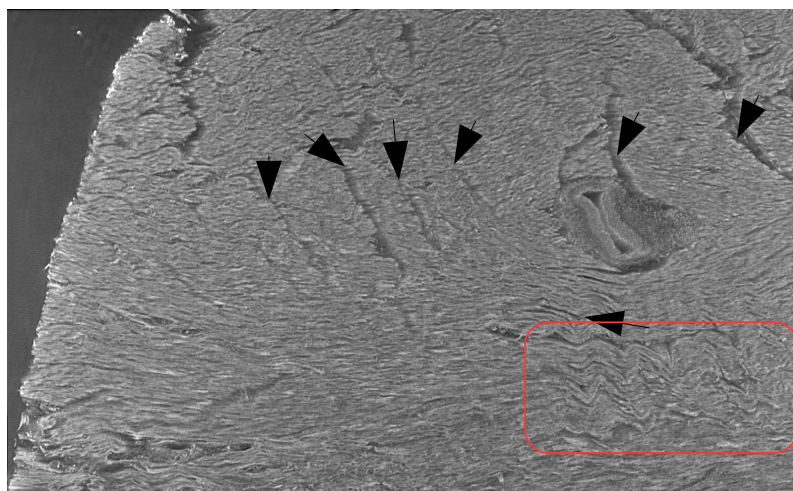
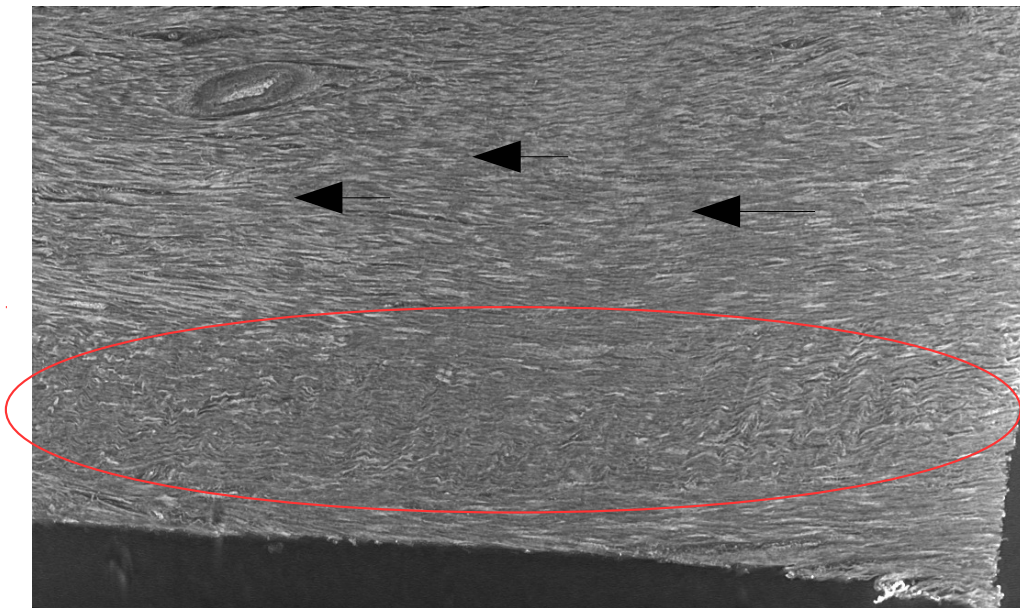
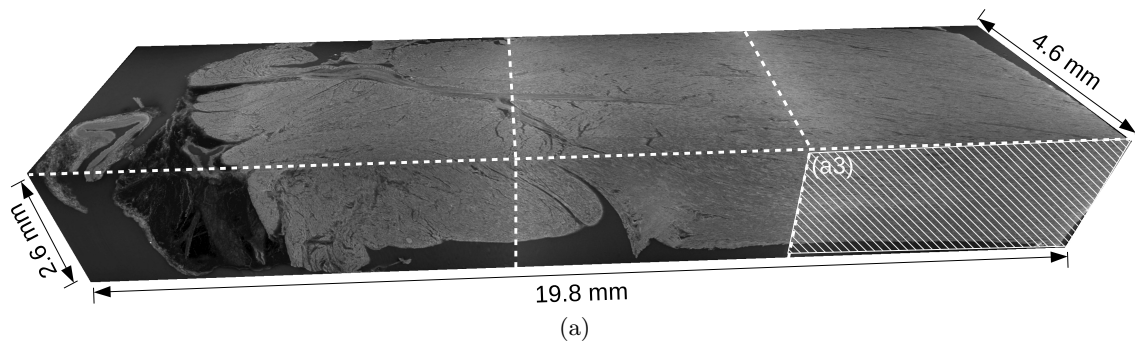


Figure A.5: Zoom-in on the front face (a3, hatched, shown in A.5b) and its opposite face (2.14) from the anterior septum sample from Figure 2.15. Both faces present areas of wavy extracellular matrix and myocytes (inside the red contours). In A.5c) the cleavage planes (black arrows) are thicker than in A.5b, and in the upper half of A.5c, the myocytes are transversally oriented. In the lower half of A.5c, a longitudinal crimped collagen structure can be seen (red square).

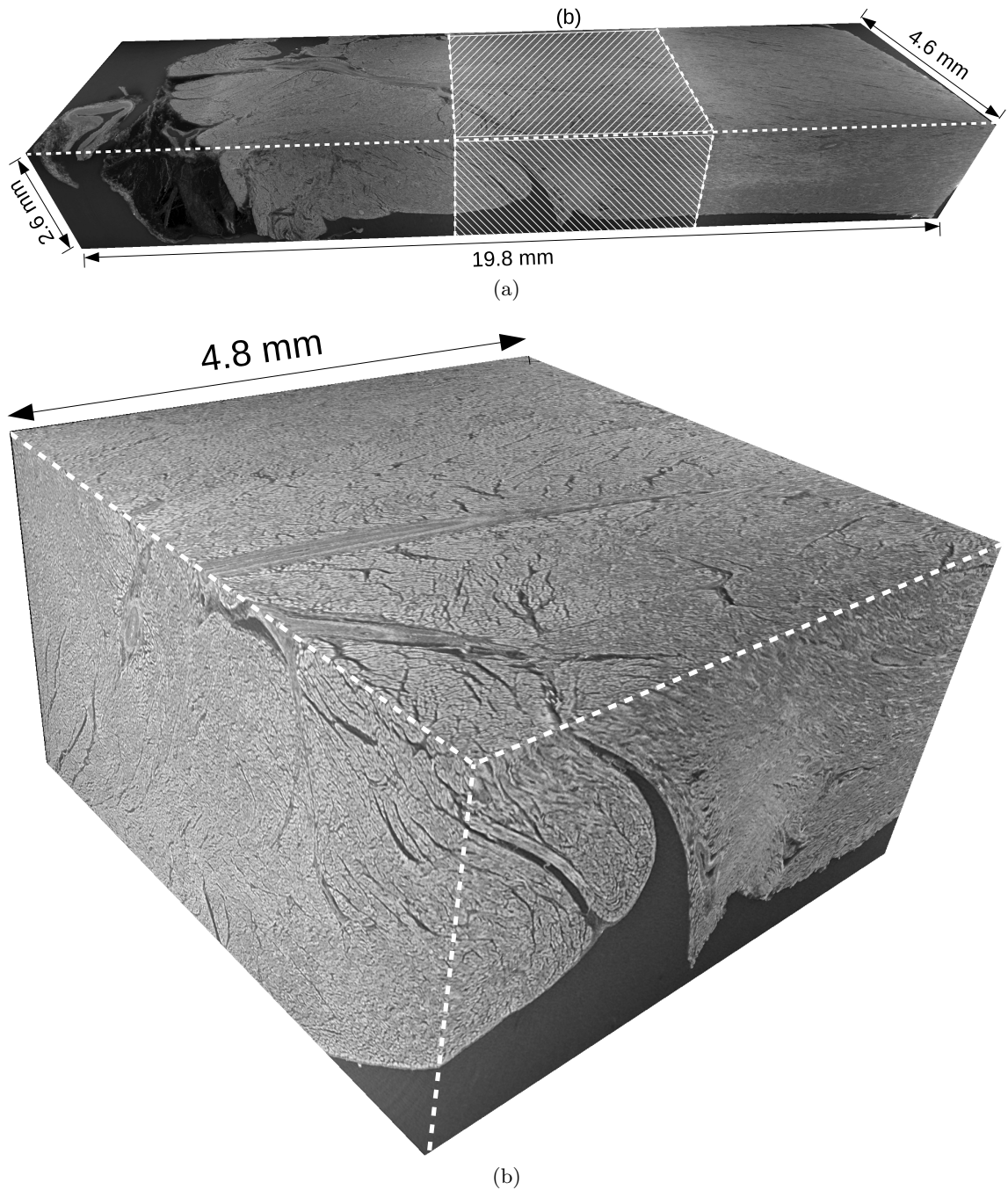


Figure A.6: *Zoom-in on the cube marked (b) of the anterior septum sample shown in Figure 2.14. A ramification of an artery is visible on the top face. The structure is generally compact, but there are cleavage planes visible in the vicinity of the arteries.*

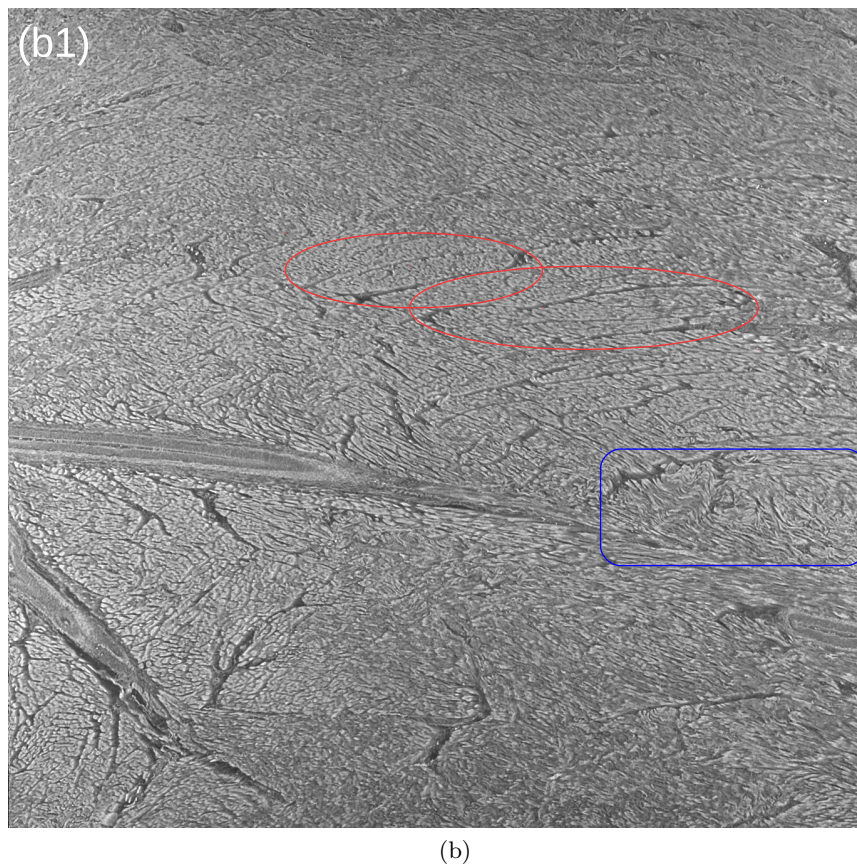
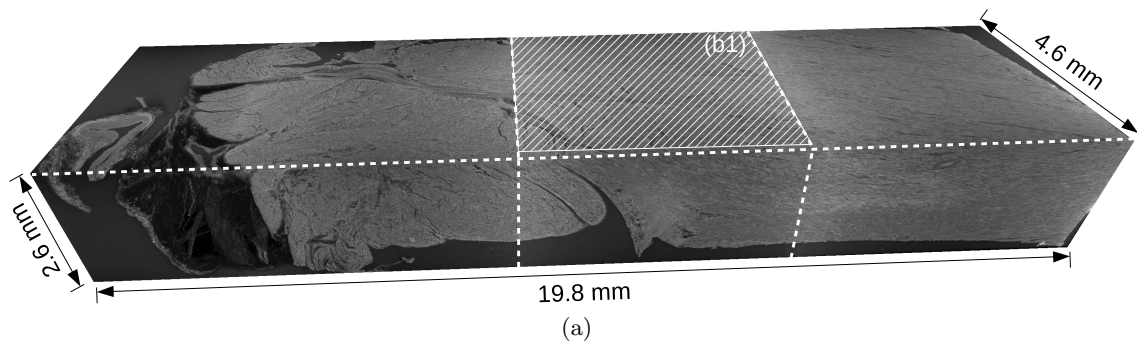


Figure A.7: *Zoom-in on the top face of the anterior septum sample from Figure A.6. Note the wavy extracellular matrix and myocytes (inside the blue square) and groups of myocytes, in transversal view, surrounded by perimysium (red ellipses).*

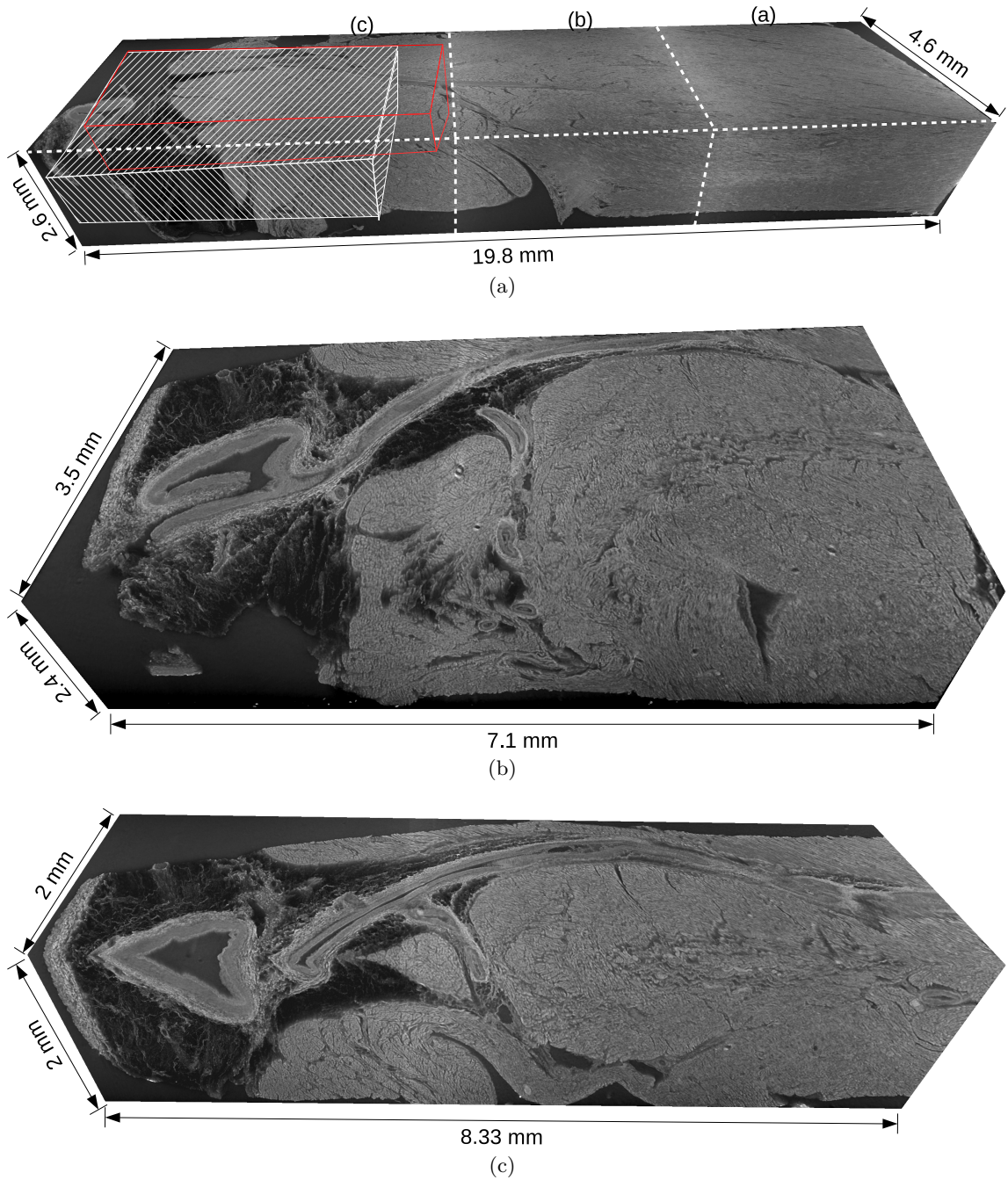


Figure A.8: Zoom-in on part (c) from the anterior septum sample from Figure 2.14. Two different 3D cuts are shown, the white hatched cut in A.8b and the red cut in A.8c. A.8a: a big CP can be seen, containing a large artery in transversal section (left) from which a smaller ramification departs towards the right (in longitudinal section). Collagen fibers can be seen as thin white filaments on the black background around the large artery.

Bibliography

- [Anderson *et al.* (2005)] Anderson, R. H., Ho, S. Y., Redmann, K., Sanchez-Quintana, D., and Lunkenheimer, P. P. (2005). The anatomical arrangement of the myocardial cells making up the ventricular mass. *European journal of cardio-thoracic surgery*, 28(4):517–525.
- [Anderson *et al.* (2006)] Anderson, R. H., Ho, S. Y., Sanchez-Quintana, D., Redmann, K., and Lunkenheimer, P. P. (2006). Heuristic problems in defining the three-dimensional arrangement of the ventricular myocytes. *The Anatomical Record*, 288(6):579–586.
- [Axel *et al.* (2014)] Axel, L., Wedeen, V. J., and Ennis, D. B. (2014). Probing dynamic myocardial microstructure with cardiac magnetic resonance diffusion tensor imaging. *Journal of Cardiovascular Magnetic Resonance*, 16(1):89.
- [Baltes *et al.* (2009)] Baltes, C., Radzwill, N., Bosshard, S., Marek, D., and Rudin, M. (2009). Micro mri of the mouse brain using a novel 400 mhz cryogenic quadrature rf probe. *NMR in biomedicine*, 22(8):834–842.
- [Bernus *et al.* (2015)] Bernus, O., Radjenovic, A., Trew, M. L., LeGrice, I. J., Sands, G. B., Magee, D. R., Smaill, B. H., and Gilbert, S. H. (2015). Comparison of diffusion tensor imaging by cardiovascular magnetic resonance and gadolinium enhanced 3d image intensity approaches to investigation of structural anisotropy in explanted rat hearts. *Journal of Cardiovascular Magnetic Resonance*, 17(1):31.
- [Bishop and Lindahl (1999)] Bishop, J. E. and Lindahl, G. (1999). Regulation of cardiovascular collagen synthesis by mechanical load. *Cardiovascular research*, 42(1):27–44.
- [Bracewell and Riddle (1967)] Bracewell, R. N. and Riddle, A. C. (1967). Inversion of fan-beam scans in radio astronomy. *Astrophysical Journal*, 150(1):427–434.
- [CIBC] CIBC. Seg3D: Volumetric Image Segmentation and Visualization. Scientific Computing and Imaging Institute (SCI), Download from: <http://www.seg3d.org>.
- [Caulfield and Borg (1979)] Caulfield, J. and Borg, T. (1979). The collagen network of the heart. *Lab Invest*, 40(1):364–72.
- [Chen *et al.* (2005)] Chen, J., Liu, W., Zhang, H., Lacy, L., Yang, X., Song, S.-K., Wickline, S. A., and Yu, X. (2005). Regional ventricular wall thickening reflects changes in cardiac fiber and sheet structure during contraction: quantification with diffusion tensor mri. *American journal of physiology. Heart and circulatory physiology*, 289(5):H1898–907.
- [Cheng *et al.* (2005)] Cheng, A., Langer, F., Rodriguez, F., Criscione, J. C., Daughters, G. T., Miller, D. C., and Ingels, N. B. (2005). Transmural sheet strains in the lateral

- wall of the ovine left ventricle. *American Journal of Physiology-Heart and Circulatory Physiology*, 289(3):H1234–H1241.
- [Cloetens *et al.* (1999)] Cloetens, P., Ludwig, W., Baruchel, J., Van Dyck, D., Van Landuyt, J., Guigay, J., and Schlenker, M. (1999). Holotomography: Quantitative phase tomography with micrometer resolution using hard synchrotron radiation x rays. *Applied physics letters*, 75(19):2912–2914.
- [Costa *et al.* (1999)] Costa, K. D., Takayama, Y., McCulloch, A. D., and Covell, J. W. (1999). Laminar fiber architecture and three-dimensional systolic mechanics in canine ventricular myocardium. *American Journal of Physiology-Heart and Circulatory Physiology*, 276(2):H595–H607.
- [Desrosiers *et al.* (2012)] Desrosiers, P. A., Michalowicz, G., Jouk, P.-S., Usson, Y., and Zhu, Y. (2012). Modeling of the optical behavior of myocardial fibers in polarized light imaging. In *International Workshop on Statistical Atlases and Computational Models of the Heart*, pages 235–244. Springer.
- [Dettmeyer *et al.* (2013)] Dettmeyer, R., Verhoff, M. A., and Schütz, H. F. (2013). Forensic medicine: fundamentals and perspectives. *Springer Science & Business Media*.
- [Dokos *et al.* (2002)] Dokos, S., Smaill, B. H., Young, A. A., and LeGrice, I. J. (2002). Shear properties of passive ventricular myocardium. *American Journal of Physiology-Heart and Circulatory Physiology*, 283(6):H2650–H2659.
- [Dolber and Spach (1987)] Dolber, P. C. and Spach, M. S. (1987). Thin collagenous septa in cardiac muscle. *The Anatomical Record*, 218(1):45–55.
- [Doste *et al.* (2017)] Doste, R., Soto-Iglesias, D., Bernardino, G., Sebastian, R., Giffard-Roisin, S., Cabrera-Lozoya, R., Sermesant, M., Berruezo, A., Sánchez-Quintana, D., and Camara, O. (2017). A rule-based method to model myocardial fiber orientation for simulating ventricular outflow tract arrhythmias. In *International Conference on Functional Imaging and Modeling of the Heart*, pages 344–353. Springer.
- [Egerton (2005)] Egerton, R. F. (2005). *Physical principles of electron microscopy*. Springer.
- [Eroschenko (2008)] Eroschenko, V. P. (2008). Atlas of histology with functional correlations. *Williams and Wilkins Lippincott*, pages 171–184.
- [Fernandez-Teran and Hurle (1982)] Fernandez-Teran, M. and Hurle, J. (1982). Myocardial fiber architecture of the human heart ventricles. *The Anatomical Record*, 204(2):137–147.
- [Ferreira *et al.* (2014)] Ferreira, P. F., Kilner, P. J., McGill, L.-A., Nilles-Vallespin, S., Scott, A. D., Ho, S. Y., McCarthy, K. P., Haba, M. M., Ismail, T. F., Gatehouse, P. D., *et al.* (2014). In vivo cardiovascular magnetic resonance diffusion tensor imaging shows evidence of abnormal myocardial laminar orientations and mobility in hypertrophic cardiomyopathy. *Journal of Cardiovascular Magnetic Resonance*, 16(1):87.
- [Fox and Hutchins (1972)] Fox, C. C. and Hutchins, G. (1972). The architecture of the human ventricular myocardium. *The Johns Hopkins medical journal*, 130(5):289–299.

- [Gerdes *et al.* (1986)] Gerdes, A. M., Moore, J. A., Hines, J. M., Kirkland, P., and Bishop, S. P. (1986). Regional differences in myocyte size in normal rat heart. *The Anatomical Record*, 215(4):420–426.
- [Gilbert *et al.* (2007)] Gilbert, S. H., Benson, A. P., Li, P., and Holden, A. V. (2007). Regional localisation of left ventricular sheet structure: integration with current models of cardiac fibre, sheet and band structure. *European journal of cardio-thoracic surgery*, 32(2):231–249.
- [Goblot *et al.* (2016)] Goblot, D., Pop, M., and Siddiqi, K. (2016). Cartan frame analysis of hearts with infarcts. In *International Workshop on Statistical Atlases and Computational Models of the Heart*, pages 87–95. Springer.
- [Grant (1965)] Grant, R. P. (1965). Notes on the muscular architecture of the left ventricle. *Circulation*, 32(2):301–308.
- [Greenbaum *et al.* (1981)] Greenbaum, R., Ho, S. Y., Gibson, D., Becker, A., and Anderson, R. (1981). Left ventricular fibre architecture in man. *British heart journal*, 45(3):248–263.
- [Groso *et al.* (2006)] Groso, A., Abela, R., and Stampanoni, M. (2006). Implementation of a fast method for high resolution phase contrast tomography. *Opt. Express*, 14(18):8103–8110.
- [Gureyev *et al.* (2004)] Gureyev, T. E., Davis, T. J., Pogany, A., Mayo, S. C., and Wilkins, S. W. (2004). Optical phase retrieval by use of first born- and rytov-type approximations. *Appl. Opt.*, 43(12):2418–2430.
- [Hanley *et al.* (1999)] Hanley, P. J., Young, A. A., LeGrice, I. J., Edgar, S. G., and Loiselle, D. S. (1999). 3-dimensional configuration of perimysial collagen fibres in rat cardiac muscle at resting and extended sarcomere lengths. *The Journal of Physiology*, 517(3):831–837.
- [Harrington *et al.* (2005)] Harrington, K. B., Rodriguez, F., Cheng, A., Langer, F., Ashikaga, H., Daughters, G. T., Criscione, J. C., Ingels, N. B., and Miller, D. C. (2005). Direct measurement of transmural laminar architecture in the anterolateral wall of the ovine left ventricle: new implications for wall thickening mechanics. *American journal of physiology. Heart and circulatory physiology*, 288(3):H1324.
- [Helm *et al.* (2005)a] Helm, P., Beg, M. F., Miller, M. I., and Winslow, R. L. (2005a). Measuring and mapping cardiac fiber and laminar architecture using diffusion tensor mr imaging. *Annals of the New York Academy of Sciences*, 1047(1):296–307.
- [Helm *et al.* (2005)b] Helm, P. A., Tseng, H.-J., Younes, L., McVeigh, E. R., and Winslow, R. L. (2005b). Ex vivo 3d diffusion tensor imaging and quantification of cardiac laminar structure. *Magnetic resonance in medicine*, 54(4):850–859.
- [Helm *et al.* (2006)] Helm, P. A., Younes, L., Beg, M. F., Ennis, D. B., Leclercq, C., Faris, O. P., McVeigh, E., Kass, D., Miller, M. I., and Winslow, R. L. (2006). Evidence of structural remodeling in the dyssynchronous failing heart. *Circulation Research*, 98(1):125–132.
- [Hitchcock (1941)] Hitchcock, F. L. (1941). The distribution of a product from several sources to numerous localities. *Journal of Mathematics and Physics*, 20(1-4):224–230.

- [Hort (1957)a] Hort, W. (1957a). Mikrometrische untersuchungen an verschieden weiten meerschweinchenherzen. In *Klinische Wochenschrift*, volume 35, pages 698–698. Springer Verlag 175.
- [Hort (1957)b] Hort, W. (1957b). Untersuchungen über die muskelfaserdehnung und das gefüge des myokards in der rechten herzkammerwand des meerschweinchens. *Virchows Archiv*, 329(6):694–731.
- [Hort (1960)] Hort, W. (1960). Makroskopische und mikrometrische untersuchungen am myokard verschieden stark gefüllter linker kammern. *Virchows Archiv*, 333(6):523–564.
- [Icardo and Colvee (1998)] Icardo, J. M. and Colvee, E. (1998). Collagenous skeleton of the human mitral papillary muscle. *The Anatomical Record*, 252(4):509–518.
- [Jiang *et al.* (2004)] Jiang, Y., Pandya, K., Smithies, O., and Hsu, E. W. (2004). Three-dimensional diffusion tensor microscopy of fixed mouse hearts. *Magnetic resonance in medicine*, 52(3):453–460.
- [Jouk *et al.* (2000)] Jouk, P.-S., Usson, Y., Michalowicz, G., and Grossi, L. (2000). Three-dimensional cartography of the pattern of the myofibres in the second trimester fetal human heart. *Anatomy and embryology*, 202(2):103–118.
- [Jouk *et al.* (2007)] Jouk, P.-S., Mourad, A., Milisic, V., Michalowicz, G., Raoult, A., Caillerie, D., and Usson, Y. (2007). Analysis of the fiber architecture of the heart by quantitative polarized light microscopy. accuracy, limitations and contribution to the study of the fiber architecture of the ventricles during fetal and neonatal life. *European journal of cardio-thoracic surgery*, 31(5):915–921.
- [Kanzaki *et al.* (2010)] Kanzaki, Y., Terasaki, F., Okabe, M., Fujita, S., Katashima, T., Otsuka, K., and Ishizaka, N. (2010). Three-dimensional architecture of cardiomyocytes and connective tissue in human heart revealed by scanning electron microscopy.
- [Kanzaki *et al.* (2012)a] Kanzaki, Y., Yamauchi, Y., Okabe, M., Terasaki, F., and Ishizaka, N. (2012a). Three-dimensional architecture of cardiomyocytes and connective tissues in hypertrophic cardiomyopathy. *Circulation*, 125(5):738–739.
- [Kanzaki *et al.* (2012)b] Kanzaki, Y., Yamauchi, Y., Okabe, M., Terasaki, F., and Ishizaka, N. (2012b). Three-dimensional architecture of cardiomyocytes and connective tissues in hypertrophic cardiomyopathy. *Circulation*, 125(5):738–739.
- [Kocica *et al.* (2006)] Kocica, M. J., Corno, A. F., Carreras-Costa, F., Ballester-Rodes, M., Moghbel, M. C., Cueva, C. N., Lackovic, V., Kanjuh, V. I., and Torrent-Guasp, F. (2006). The helical ventricular myocardial band: global, three-dimensional, functional architecture of the ventricular myocardium. *European Journal of Cardio-thoracic Surgery*, 29(Supplement 1):S21–S40.
- [Krehl (1891)] Krehl, L. I. (1891). *Beiträge zur kenntnis der füllung und entleerung des herzens*. Hirzel.
- [Kung *et al.* (2011)] Kung, G. L., Nguyen, T. C., Itoh, A., Skare, S., Ingels, N. B., Miller, D. C., and Ennis, D. B. (2011). The presence of two local myocardial sheet populations confirmed by diffusion tensor mri and histological validation. *Journal of Magnetic Resonance Imaging*, 34(5):1080–1091.

- [Labiche *et al.* (2007)] Labiche, J.-C., Mathon, O., Pascarelli, S., Newton, M. A., Ferre, G. G., Curfs, C., Vaughan, G., Homs, A., and Carreiras, D. F. (2007). Invited article: The fast readout low noise camera as a versatile x-ray detector for time resolved dispersive extended x-ray absorption fine structure and diffraction studies of dynamic problems in materials science, chemistry, and catalysis. *Review of scientific instruments*, 78(9):091301.
- [LeGrice *et al.* (1995)] LeGrice, I. J., Smaill, B., Chai, L., Edgar, S., Gavin, J., and Hunter, P. J. (1995). Laminar structure of the heart: ventricular myocyte arrangement and connective tissue architecture in the dog. *American Journal of Physiology-Heart and Circulatory Physiology*, 269(2):H571–H582.
- [LeGrice *et al.* (1997)] LeGrice, I. J., Hunter, P. J., and Smaill, B. (1997). Laminar structure of the heart: a mathematical model. *American Journal of Physiology-Heart and Circulatory Physiology*, 272(5):H2466–H2476.
- [LeGrice *et al.* (2001)] LeGrice, I., Hunter, P., Young, A., and Smaill, B. (2001). The architecture of the heart: a data-based model. *Philosophical Transactions of the Royal Society of London A: Mathematical, Physical and Engineering Sciences*, 359(1783):1217–1232.
- [LeGrice *et al.* (2004)] LeGrice, I., Sands, G., Hooks, D., Gerneke, D., and Smaill, B. (2004). Microscopic imaging of extended tissue volumes. *Clinical and experimental pharmacology and physiology*, 31(12):902–905.
- [LeGrice *et al.* (2005)] LeGrice, I. J., Pope, A., and Smaill, B. (2005). Chapter 1. the architecture of the heart: Myocyte organization and the cardiac extracellular matrix. *Interstitial Fibrosis in Heart Failure*, 253(1):3–20.
- [Lev and Simkins (1956)] Lev, M. and Simkins, C. (1956). Architecture of the human ventricular myocardium; technic for study using a modification of the mall-maccallum method. *Laboratory investigation; a journal of technical methods and pathology*, 5(5):396.
- [Mall (1911)] Mall, F. P. (1911). On the muscular architecture of the ventricles of the human heart. *Developmental Dynamics*, 11(3):211–266.
- [McLean and Prothero (1991)] McLean, M. and Prothero, J. (1991). Myofiber orientation in the weanling mouse heart. *Developmental Dynamics*, 192(4):425–441.
- [Mirea *et al.* (2015)] Mirea, I., Varray, F., Zhu, Y. M., Fanton, L., Langer, M., Jouk, P.-S., Michalowicz, G., Usson, Y., and Magnin, I. E. (2015). Very high-resolution imaging of post-mortem human cardiac tissue using x-ray phase contrast tomography. *International Conference on Functional Imaging and Modeling of the Heart. LNCS*, 9126:172–179.
- [Mirea *et al.* (2016)] Mirea, I., Wang, L., Varray, F., Zhu, Y.-M., Serrano, E. D., and Magnin, I. E. (2016). Statistical analysis of transmural laminar microarchitecture of the human left ventricle. *2016 IEEE 13th International Conference on Signal Processing (ICSP)*, pages 53–56.
- [Morita *et al.* (1991)] Morita, T., Shimada, T., Kitamura, H., and Nakamura, M. (1991). Demonstration of connective tissue sheaths surrounding working myocardial cells and purkinje cells of the sheep moderator band. *Archives of histology and cytology*, 54(5):539–550.

- [Otsu (1979)] Otsu, N. (1979). A Threshold Selection Method from Gray-level Histograms. *IEEE Transactions on Systems, Man and Cybernetics*, 9(1):62–66.
- [Paganin *et al.* (2002)] Paganin, D., Mayo, S., Gureyev, T. E., Miller, P. R., and Wilkins, S. W. (2002). Simultaneous phase and amplitude extraction from a single defocused image of a homogeneous object. *Journal of microscopy*, 206(1):33–40.
- [Pope *et al.* (2008)] Pope, A. J., Sands, G. B., Smaill, B. H., and LeGrice, I. J. (2008). Three-dimensional transmural organization of perimysial collagen in the heart. *American Journal of Physiology-Heart and Circulatory Physiology*, 295(3):H1243–H1252.
- [Prado *et al.* (2002)] Prado, I., Motta, P., Stallone, T., Camboni, A., Nottola, S., Macchiarelli, G., and Ohtani, O. (2002). A micro-anatomical model of the distribution of myocardial endomysial collagen. *Histology and histopathology*.
- [Rachev (1985)] Rachev, S. T. (1985). The monge–kantorovich mass transference problem and its stochastic applications. *Theory of Probability & Its Applications*, 29(4):647–676.
- [Robb and Robb (1942)] Robb, J. S. and Robb, R. C. (1942). The normal heart: anatomy and physiology of the structural units. *American Heart Journal*, 23(4):455–467.
- [Robert and Freitas (2004)] Robert, A. and Freitas, J. (2004). Nanomedicine. vol. 1: Basic capabilities. *Landes Bioscience; 1999*.
- [Robinson *et al.* (1983)] Robinson, T., Cohen-Gould, L., Factor, S., and Borg, T. (1983). Skeletal framework of mammalian heart muscle. arrangement of inter- and pericellular connective tissue structures. *Lab Invest*, 49(4):482–98.
- [Ross *et al.* (1967)] Ross, J., Sonnenblick, E. H., Covell, J. W., Kaiser, G. A., and Spiro, D. (1967). The architecture of the heart in systole and diastole. *Circulation research*, 21(4):409–421.
- [Rubner *et al.* (1998)] Rubner, Y., Tomasi, C., and Guibas, L. J. (1998). A metric for distributions with applications to image databases. In *Proceedings of the Sixth International Conference on Computer Vision, ICCV '98*, pages 59–, Washington, DC, USA. IEEE Computer Society.
- [Rubner *et al.* (2000)] Rubner, Y., Tomasi, C., and Guibas, L. J. (2000). The earth mover’s distance as a metric for image retrieval. *International journal of computer vision*, 40(2):99–121.
- [Rushmer *et al.* (1953)] Rushmer, R. F., Crystal, D. K., and Wagner, C. (1953). The functional anatomy of ventricular contraction. *Circulation Research*, 1(2):162–170.
- [Sachse *et al.* (2009)] Sachse, F. B., Savio-Galimberti, E., Goldhaber, J. I., and Bridge, J. H. (2009). Towards computational modeling of excitation-contraction coupling in cardiac myocytes: reconstruction of structures and proteins from confocal imaging. In *Pacific Symposium on Biocomputing. Pacific Symposium on Biocomputing*, page 328. NIH Public Access.
- [Salomé *et al.* (1999)] Salomé, M., Peyrin, F., Cloetens, P., Odet, C., Laval-Jeantet, A.-M., Baruchel, J., and Spanne, P. (1999). A synchrotron radiation microtomography system for the analysis of trabecular bone samples. *Medical Physics*, 26(10):2194–2204.

- [Sanchez-Quintana *et al.* (1990)] Sanchez-Quintana, D., Garcia-Martinez, V., and Hurle, J. (1990). Myocardial fiber architecture in the human heart. *Cells Tissues Organs*, 138(4):352–358.
- [Sanchez-Quintana *et al.* (1995)] Sanchez-Quintana, D., Garcia-Martinez, V., Climent, V., and Hurle, J. M. (1995). Morphological changes in the normal pattern of ventricular myoarchitecture in the developing human heart. *The Anatomical Record*, 243(4):483–495.
- [Sanchez-Quintana *et al.* (1996)] Sanchez-Quintana, D., Anderson, R. H., and Ho, S. Y. (1996). Ventricular myoarchitecture in tetralogy of fallot. *Heart*, 76(3):280–286.
- [Sands *et al.* (2005)] Sands, G. B., Gerneke, D. A., Hooks, D. A., Green, C. R., Smaill, B. H., and Legrice, I. J. (2005). Automated imaging of extended tissue volumes using confocal microscopy. *Microscopy research and technique*, 67(5):227–239.
- [Satoh *et al.* (1996)] Satoh, H., Delbridge, L., Blatter, L. A., and Bers, D. M. (1996). Surface: volume relationship in cardiac myocytes studied with confocal microscopy and membrane capacitance measurements: species-dependence and developmental effects. *Biophysical journal*, 70(3):1494–1504.
- [Schmid *et al.* (2005)] Schmid, P., Jaermann, T., Boesiger, P., Niederer, P. F., Lunkenheimer, P. P., Cryer, C. W., and Anderson, R. H. (2005). Ventricular myocardial architecture as visualised in postmortem swine hearts using magnetic resonance diffusion tensor imaging. *European journal of cardio-thoracic surgery*, 27(3):468–472.
- [Serrano *et al.* (2012)] Serrano, E. E. D., Guigues, L., Roux, J.-P., Cervenansky, F., Camarasu-Pop, S., Reyes, J. G. R., Flórez-Valencia, L., Hoyos, M. H., and Orkisz, M. (2012). Creatools: A framework to develop medical image processing software: Application to simulate pipeline stent deployment in intracranial vessels with aneurysms. In *International Conference on Computer Vision and Graphics*, pages 55–62. Springer.
- [Severs (2000)] Severs, N. J. (2000). The cardiac muscle cell. *Bioessays*, 22(2):188–199.
- [Snigirev *et al.* (1995)] Snigirev, A., Snigireva, I., Kohn, V., Kuznetsov, S., and Schelokov, I. (1995). On the possibilities of x-ray phase contrast microimaging by coherent high-energy synchrotron radiation. *Review of scientific instruments*, 66(12):5486–5492.
- [Spach *et al.* (2004)] Spach, M. S., Heidlage, J. F., Barr, R. C., and Dolber, P. C. (2004). Cell size and communication: role in structural and electrical development and remodeling of the heart. *Heart Rhythm*, 1(4):500–515.
- [Spotnitz *et al.* (1974)] Spotnitz, H. M., Spotnitz, W. D., Cottrell, T. S., Spiro, D., and Sonnenblick, E. H. (1974). Cellular basis for volume related wall thickness changes in the rat left ventricle. *Journal of molecular and cellular cardiology*, 6(4):317–331.
- [Streeter (1979)] Streeter, J. D. (1979). Gross morphology and fiber geometry of the heart. *Handbook of Physiology*, Baltimore: Williams and Wilkins;(1):61–112.
- [Streeter *et al.* (1969)] Streeter, D. D., Spotnitz, H. M., Patel, D. P., Ross, J., and Sonnenblick, E. H. (1969). Fiber orientation in the canine left ventricle during diastole and systole. *Circulation research*, 24(3):339–347.

- [Torrent-Guasp (1975)] Torrent-Guasp, F. (1975). Organizacion de la musculatura cardiaca ventricular. *Zarco P., Perez J.(eds) El Fallo Mecanico del Corazon*, pages 3–36.
- [Torrent-Guasp *et al.* (2001)] Torrent-Guasp, F., Ballester, M., Buckberg, G. D., Carreras, F., Flotats, A., Carrió, I., Ferreira, A., Samuels, L. E., and Narula, J. (2001). Spatial orientation of the ventricular muscle band: physiologic contribution and surgical implications. *The Journal of Thoracic and Cardiovascular Surgery*, 122(2):389–392.
- [Torrent-Guasp *et al.* (2004)] Torrent-Guasp, F., Kocica, M. J., Corno, A., Komeda, M., Cox, J., Flotats, A., Ballester-Rodes, M., and Carreras-Costa, F. (2004). Systolic ventricular filling. *European journal of cardio-thoracic surgery*, 25(3):376–386.
- [Torrent-Guasp *et al.* (2005)] Torrent-Guasp, F., Kocica, M. J., Corno, A. F., Komeda, M., Carreras-Costa, F., Flotats, A., Cosin-Aguillar, J., and Wen, H. (2005). Towards new understanding of the heart structure and function. *European Journal of Cardio-Thoracic Surgery*, 27(2):191–201.
- [Trew *et al.* (2006)] Trew, M. L., Caldwell, B. J., Sands, G. B., Hooks, D. A., Tai, D. C.-S., Austin, T. M., LeGrice, I. J., Pullan, A. J., and Smaill, B. H. (2006). Cardiac electrophysiology and tissue structure: bridging the scale gap with a joint measurement and modelling paradigm. *Experimental physiology*, 91(2):355–370.
- [Varray *et al.* (2013)] Varray, F., Wang, L., Fanton, L., Zhu, Y., and Magnin, I. (2013). High resolution extraction of local human cardiac fibre orientations. *International Conference on Functional Imaging and Modeling of the Heart*, LNCS 7945:150–157.
- [Varray *et al.* (2017)] Varray, F., Mirea, I., Langer, M., Peyrin, F., Fanton, L., and Magnin, I. E. (2017). Extraction of the 3d local orientation of myocytes in human cardiac tissue using x-ray phase-contrast micro-tomography and multi-scale analysis. *Medical image analysis*, 38:117–132.
- [Veinot *et al.* (2001)] Veinot, J., Ghadially, F., and Walley, V. (2001). Light microscopy and ultrastructure of the blood vessel and heart. *Cardiovascular Pathology. 3rd ed. New York, NY: Churchill Livingstone*, pages 30–53.
- [Villarreal (2004)] Villarreal, F. (2004). *Interstitial fibrosis in heart failure*, volume 253. Springer Science & Business Media.
- [Wang *et al.* (2012)] Wang, L., Zhu, Y., Li, H., Liu, W., and Magnin, I. E. (2012). Multi-scale modeling and simulation of the cardiac fiber architecture for dmri. *IEEE Transactions on Biomedical Engineering*, 59(1):16–19.
- [Weber (1989)] Weber, K. T. (1989). Cardiac interstitium in health and disease: the fibrillar collagen network. *Journal of the American College of Cardiology*, 13(7):1637–1652.
- [Weber *et al.* (1994)] Weber, K. T., Sun, Y., Tyagi, S. C., and Cleutjens, J. P. (1994). Collagen network of the myocardium: function, structural remodeling and regulatory mechanisms. *Journal of molecular and cellular cardiology*, 26(3):279–292.
- [Weitkamp *et al.* (2011)] Weitkamp, T., Haas, D., Wegrzynek, D., and Rack, A. (2011). Ankaphase: software for single-distance phase retrieval from inline x-ray phase-contrast radiographs. *Journal of synchrotron radiation*, 18(4):617–629.

- [Wu and Liu (2005)] Wu, X. and Liu, H. (2005). X-ray cone-beam phase tomography formulas based on phase-attenuation duality. *Opt. Express*, 13(16):6000–6014.
- [Yacoub (1995)] Yacoub, M. H. (1995). Two hearts that beat as one. *Circulation*, 92(2):156–157.
- [Young *et al.* (1998)] Young, A., LeGrice, I., Young, M., and Smaill, B. (1998). Extended confocal microscopy of myocardial laminae and collagen network. *Journal of Microscopy*, 192(2):139–150.
- [Zhao *et al.* (2012)] Zhao, J., Butters, T. D., Zhang, H., Pullan, A. J., LeGrice, I. J., Sands, G. B., and Smaill, B. H. (2012). An image-based model of atrial muscular architecture: effects of structural anisotropy on electrical activation. *Circulation: Arrhythmia and Electrophysiology*, pages CIRCEP–111.

TITRE EN FRANCAIS

Analyse de la microstructure 3D du tissu cardiaque humain à l'aide de la micro-tomographie à rayons X par contraste de phase

RESUME EN FRANCAIS

Les pathologies cardiovasculaires restent un des problèmes majeurs de santé publique qui justifie les recherches menées pour améliorer notre compréhension de la fonction cardiaque. Celles-ci nécessitent une bonne connaissance de la microarchitecture myocardique afin de mieux comprendre les relations entre les fonctions mécanique, hémodynamique et les changements structuraux induits par les maladies cardiaques. Pour ce faire il est nécessaire d'accéder à une connaissance précise de l'arrangement spatial des composants du tissu. Cependant, notre compréhension de l'architecture du coeur est limitée par le manque de description 3D de l'organisation des structures à l'échelle microscopique. Nous proposons d'explorer la structure 3D du tissu cardiaque en utilisant l'imagerie X synchrotron par contraste de phase disponible à l'ESRF. Pour la première fois, 9 échantillons de tissu de la paroi du ventricule gauche (VG) humain sont imagés à la résolution isotrope de $3,5 \mu m$ et analysés. Cette thèse est centrée sur la description 3D d'un des constituants principal du tissu: la matrice extracellulaire (MEC). La MEC inclue: l'endomysium qui entoure et sépare les myocytes et les capillaires de façon individuelle, le perimysium qui entoure et sépare des groupes de myocytes et l'épimysium qui enveloppe le muscle cardiaque dans son ensemble. Chaque échantillon reconstruit fait environ 30 Gb, ce qui représente une quantité importante de données à traiter et à visualiser. Pour ce faire, nous avons développé un algorithme automatique de traitement d'image pour binariser chaque échantillon et isoler la MEC. Ensuite, nous avons extrait des paramètres statistiques relatifs à la microarchitecture de l'ECM, principalement l'épaisseur des plans de clivage (PC) et les distances inter-PC. Les résultats montrent que l'arrangement local des PC diffère selon l'emplacement au sein du VG (postérieur, antérieur, septal) et de leur distance à l'apex (plus complexe). L'épaisseur des PC extraite de tous les échantillons va approximativement de $24 \mu m$ à $59 \mu m$ et la distance inter-PC de $70 \mu m$ à $280 \mu m$ avec une variation locale significative de la déviation standard. Ce sont de nouveaux marqueurs quantitatifs de la MEC du tissu cardiaque humain qui sont d'un intérêt majeur pour une meilleure compréhension de la fonction cardiaque.

TITRE EN ANGLAIS

Analysis of the 3D microstructure of the human cardiac tissue using X-ray phase contrast micro-tomography

RESUME EN ANGLAIS

Cardiovascular diseases remain one of the most serious health problems, motivating research to deepen our understanding of the myocardial function. To succeed, there is a need to get detailed information about the spatial arrangement of the cardiac tissue components. Currently, our understanding of the cardiac microarchitecture is limited by the lack of 3D descriptions of the cardiac tissue at the microscopic scale. This thesis investigates the 3D cardiac tissue microstructure using X-Ray μ -CT phase contrast imaging available at the ESRF. For the first time, 9 human cardiac left ventricle (LV) wall samples are imaged at an isotropic resolution ($3.5 \mu m$) and analysed. We focus on the description of the cardiac extracellular matrix (CEM) that is one of the main components of the tissue. The CEM includes: the endomysium that surrounds and separates individual myocytes and capillaries, the perimysium that surrounds groups of myocytes and the epimysium that surrounds the entire heart muscle. Each reconstructed sample is about 30 GB which represents a large amount of data to process and display. To succeed, we developed an automatic image processing algorithm to binarise each sample by selecting the CEM. We extract statistical features of the ECM, mainly the thickness of the cleavage planes (CP) and the inter-CP distances. The results show that the local 3D arrangement of the CP differs according to their location in the LV (posterior, anterior, septal) and their distance from the apex (more complex). The thickness of the CP extracted from all the samples roughly ranges from $24 \mu m$ to $59 \mu m$ and the inter-CP distances from $70 \mu m$ to $280 \mu m$ with significant local variations of the standard deviation. Those new quantitative markers of the ECM of the human cardiac are of main interest for a better understanding of the heart function.

MOTS-CLES

INTRODUCTION ET ADRESSE DE L'INSA LYON / URL DU LABORATOIRE

© J. Mireal, [2017], INSA Lyon, tous droits réservés
Université de Lyon, CREATIS ; CNRS UMR5220 ; Inserm U1044 ; INSA-Lyon ; Université Lyon 1,
7 Av. Jean Capelle, 69621 VILLEURBANNE, France.